TAMPEREEN TEKNILLINEN YLIOPISTO
TAMPERE UNIVERSITY OF TECHNOLOGY

Simran Singh

Time-Interleaved Analog-to-Digital-Converters: Modeling, Blind Identification and Digital Correction of Frequency Response Mismatches

Julkaisu 1398 • Publication 1398

Tampere 2016

Tampereen teknillinen yliopisto. Julkaisu 1398
Tampere University of Technology. Publication 1398

Simran Singh

Time-Interleaved Analog-to-Digital-Converters:
Modeling, Blind Identification and Digital Correction of Frequency Response Mismatches

Thesis for the degree of Doctor of Science in Technology to be presented with due permission for public examination and criticism in Sähkötalo Building, lecture room SJ204, at Tampere University of Technology, on the 12th of August 2016, at 12 noon.

Tampereen teknillinen yliopisto - Tampere University of Technology
Tampere 2016

Supervisor
Mikko Valkama, Dr. Tech., Professor
Department of Electronics and Communications Engineering
Tampere University of Technology
Tampere, Finland

Pre-examiners
Christian Vogel, Dr. techn., Adjunct Professor
Signal Processing and Speech Communication Laboratory
University of Technology Graz
Graz, Austria

Håkan Johansson, Dr. Tech., Professor
Department of Electrical Engineering
Linköping University
Linköping, Sweden

Opponent
Timo Rahkonen, Dr. Tech., Professor
Department of Electrical Engineering
University of Oulu
Oulu, Finland

ISBN 978-952-15-3773-8 (printed)
ISBN 978-952-15-3788-2 (PDF)
ISSN 1459-2045

Abstract

Analog-to-digital-conversion enables utilization of digital signal processing (DSP) in many applications today such as wireless communication, radar and electronic warfare. DSP is the favored choice for processing information over analog signal processing (ASP) because it can typically offer more flexibility, computational power, reproducibility, speed and accuracy when processing and extracting information. Software defined radio (SDR) receiver is one clear example of this, where radio frequency waveforms are converted into digital form as close to the antenna as possible and all the processing of the information contained in the received signal is extracted in a configurable manner using DSP. In order to achieve such goals, the information collected from the real world signals, which are commonly analog in their nature, must be converted into digital form before it can be processed using DSP in the respective systems. The common trend in these systems is to not only process ever larger bandwidths of data but also to process data in digital format at ever higher processing speeds with sufficient conversion accuracy. So the analog-to-digital-converter (ADC), which converts real world analog waveforms into digital form, is one of the most important cornerstones in these systems.

The ADC must perform data conversion at higher and higher rates and digitize ever-increasing bandwidths of data. In accordance with the Nyquist-Shannon theorem, the conversion rate of the ADC must be sufficient to accomodate the BW of the signal to be digitized, in order to avoid aliasing. The conversion rate of the ADC can in general be increased by using parallel ADCs with each ADC performing the sampling at mutually different points in time. Interleaving the outputs of each of the individual ADCs provides then a higher digitization output rate. Such ADCs are referred to as TI-ADC. However, the mismatches between the ADCs cause unwanted spurious artifacts in the TI-ADC's spectrum, ultimately leading to a loss in accuracy in the TI-ADC compared to the

individual ADCs. Therefore, the removal or correction of these unwanted spurious artifacts is essential in having a high performance TI-ADC system.

In order to remove the unwanted interleaving artifacts, a model that describes the behavior of the spurious distortion products is of the utmost importance as it can then facilitate the development of efficient digital post-processing schemes. One major contribution of this thesis consists of the novel and comprehensive modeling of the spurious interleaving mismatches in different TI-ADC scenarios. This novel and comprehensive modeling is then utilized in developing digital estimation and correction methods to remove the mismatch induced spurious artifacts in the TI-ADC's spectrum and recovering its lost accuracy. Novel and first of its kind digital estimation and correction methods are developed and tested to suppress the frequency dependent mismatch spurs found in the TI-ADCs. The developed methods, in terms of the estimation of the unknown mismatches, build on statistical I/Q signal processing principles, applicable without specifically tailored calibration signals or waveforms. Techniques to increase the analog BW of the ADC are also analyzed and novel solutions are presented. The interesting combination of utilizing I/Q downconversion in conjunction with TI-ADC is examined, which not only extends the TI-ADC's analog BW but also provides flexibility in accessing the radio spectrum. Unwanted spurious components created during the ADC's bandwidth extension process are also analyzed and digital correction methods are developed to remove these spurs from the spectrum. The developed correction techniques for the removal of the undesired interleaving mismatch artifacts are validated and tested using various HW platforms, with up to 1 GHz instantaneous bandwidth. Comprehensive test scenarios are created using measurement data obtained from HW platforms, which are used to test and evaluate the performance of the developed interleaving mismatch estimation and correction schemes, evidencing excellent performance in all studied scenarios.

The findings and results presented in this thesis contribute towards increasing the analog BW and conversion rate of ADC systems without losing conversion accuracy. Overall, these developments pave the way towards fulfilling the ever growing demands on the ADCs in terms of higher conversion BW, accuracy and speed.

Preface

This thesis is based on the research work carried out from Autumn 2012 until Autumn 2015 at the Department of Electronics and Communications Engineering, Tampere University of Technology, Tampere, Finland in close collaboration with Airbus Defence and Space, Ulm, Germany.

I would like to begin with expressing my deepest gratitude to my supervisor, Prof. Dr. Mikko Valkama for providing me the opportunity to work towards this dissertation under his invaluable guidance during all these years. His extensive knowledge and experience in the field and in research together with his hard-working nature have in general been an incredible support in this part of this dissertation. His very relevant expertise in the field led to interesting discussions, strategic and constructive scrutiny of the thesis results and contributions. In this sense, it is difficult to imagine having a better suited supervisor and mentor other than Mikko.

I would also like to extended my most heartfelt thanks to Michael Epp and Dr. Wolfgang Schlecker from Airbus Defence and Space for their time, support and vigorous discussion throughout this dissertation period. Michael initiated this research work within Airbus and closely supervised this thesis with high enthusiasm as well as never losing focus on developing practical solutions. Michael's preferrence on detailed to-do lists always gave a clear picture of task sequence and time schedule. Wolfgang also assisted Michael in the supervision of this thesis work. He always tried to find time, despite his busy schedule and numerous responsibilities, to join in our discussions. He is always quick to think his way into our current discussion topics and contribute to them. A warm thanks also to Dr. Lauri Antilla for his support and guidance during the research and also during the publication phase of this thesis work, for always trying to allocate time and meeting up for a discussion.

I would like to express my gratitude to Dr. Jochen Dederer, Elmar Ingber, Cletus-Afrifa Donkor, Colin Savage, Dr. Sébastian Chartier, Dr. Georg Vallant, Dennis Honold, Frank Kehrer and all other colleagues of Airbus Defence and Space for their help and support along the way. I would also like to say thank you to Monika Korzer for her help in all office related matters and travel arrangements. Thank you to Dr. H. Brugger, U. Schneider and M. Schlumpp from Airbus Defense and Space for supporting and enabling this research work.

I would like to specially thank Dr. Markus Allén, Mahmoud Abdelaziz, Aki Hakkarainen, Dr. Janis Werner, Dr. Jaakko Marttila, Dr. Jukka Talvitie, Pedro Figueiredo e Silva, Dr. Sener Dikmese, Alaa Loulou, Dani Korpi, Dr. Adnan Kiayani, Vesa Lehtinen, Dr. Toni Levanen, Mike Koivisto, Dr. Paschalis Sofotasios, Dr. Mulugeta Fikadu, Joonas Säe and all other colleagues from the Department of Electronics and Communications Engineering (ELT) at Tampere University of Technology (TUT) for the productive, fruitful and enjoyable discussions on various topics, for sharing their experiences, expertise and providing the help when needed. A special thanks to Prof. Dr. Markku Renfors for his interesting courses and contributions towards creating a nice working environment at the department. Thank you also to Soile Lönnqvist, Elina Orava and all other organizational members of the ELT department for their help, advice, time and efforts. For their financial support, I would like to also thank the Academy of Finland (under the project 251138 Digitally-Enhanced RF for Cognitive Radio Devices), the Linz Center of Mechatronics (LCM) in the Austrian COMET-K2 programme, the Tuula and Yrjö Neuvo Fund and the Nokia Foundation, which enabled and supported participation of the TUT research members.

I am grateful to Prof. Dr. Håkan Johansson and Prof. Dr. Christian Vogel, for agreeing to act as pre-examiners for this thesis, for investing their precious time and providing valuable suggestions to improve the quality of the thesis. I would also like to thank Prof. Dr. Timo Rahkonen for his willingness to travel from Oulu to Tampere and to act as the opponent in the defense process of this dissertation.

I would also like to thank all the people who may have indirectly contributed to the successful completion of this thesis. Last but not least, I would like to express my most dearest thanks to all my family members and loved ones in life, for their continuous love and support; without whom I would not be here and this work would not have been possible.

Thank you all.

Tampere, July 2016

Simran Singh

Table of Contents

Abstract **i**

Preface **iii**

List of Publications **ix**

Abbreviations **xi**

Symbols and Notations **xiii**

1 Introduction **1**
1.1 Background and Research Motivation 1
1.2 Thesis Scope and Objectives 4
1.3 Outline and Main Results of the Thesis 5
1.4 Author's Contributions to the Publications 6
1.5 Used Mathematical Notations and Basic Modeling of the Sampling Process 7

2 Basic Concepts and State-of-the-Art of High Speed ADCs **11**
2.1 An Overview of High Speed ADC Architectures 11
2.2 Time Interleaving of ADCs 15
2.3 Downconversion Circuitry and TI-ADCs 15
2.3.1 Real Sampling TI-ADCs 15
2.3.2 I/Q Sampling TI-ADCs 17
2.4 An Overview of existing TI-ADC Mismatch Correction Methods 18
2.4.1 Mixed-signal Correction Methods 18

2.4.2 All-Digital Correction Methods 19

3 Modeling of Frequency Response Mismatches in TI-ADCs 25
3.1 FRM Modeling of 2 TI-ADC 26
3.1.1 Quantifying Replica Rejection Ratio in 2 TI-ADC 28
3.2 FRM Modeling of 4 TI-ADC 29
3.2.1 Quantifying Replica Rejection Ratio in 4 TI-ADC 33
3.3 FRM Modeling in I/Q Downconversion TI-ADCs 33
3.3.1 I/Q Downconversion Stage Mismatch Modeling 33
3.3.2 Time Interleaved ADC Stage Mismatch Modeling 35
3.3.3 Combined Effect of All Frequency Response Mismatches 37
3.3.4 The Relationship of I/Q downconversion and 2 TI-ADC FRM Spurs 39
3.4 The relationship of 2 I/Q TI-ADC and 4 TI-ADCs FRM Spurs 41

4 Identification and Compensation of TI-ADCs mismatches 43
4.1 Identification and Compensation of FRM in 2 TI-ADC 43
4.1.1 2 TI-ADC Identification and Compensation Structure - Type I . 45
4.1.2 2 TI-ADC Identification and Compensation Structure - Type II . 47
4.2 Identification and Compensation of FRMs in 4 TI-ADC 48
4.2.1 4 TI-ADC Identification Structure Type I 48
4.2.2 4 TI-ADC Identification Structure Type II 53
4.2.3 Computational Complexity Analysis 55
4.3 Identification and Compensation of FRMs in I/Q Downconversion 2 TI-ADC 57
4.3.1 I/Q Mismatch Image Spur Identification and Correction 58
4.3.2 TI Image Spur Identification and Correction 58
4.3.3 TI Spur Identification and Correction 59
4.4 MFI-based Blind Learning Algorithms 61

5 Hardware Measurements and Mismatch Correction Performance Evaluation 65
5.1 Description of Various Measurement HW Platforms 65
5.2 FRM Spur Characteristics of Measured HW 66
5.2.1 LTC2208 HW FRM Measurement 66
5.2.2 ADC12D1800RF HW FRM Measurement 68
5.2.3 I/Q Downconversion Circuitry & ADC12D1800RF HW FRM Measurement 68
5.3 Measured Performance of Proposed Blind Identification and Correction of TI-ADC FRM Spurs 71

5.3.1 Validation of Proposed Blind Identification and Correction of 2-channel TI-ADC FRM Spurs using Measured Data 71
5.3.2 Validation of Proposed Blind Identification and Correction of 4-channel TI-ADC FRM Spurs using Measured Data 72
5.3.3 Validation of Proposed Blind Identification and Correction of TI-ADC FRM Spurs using Modulated Communication Waveforms 76
5.4 Validation of Proposed Blind Identification and Correction of FRM Spurs in I/Q Downconversion 2 TI-ADC using Measured Data 79

6 Conclusions **81**
6.1 Summary of Thesis Contributions & Results 81
6.2 Possible Future Work Topics 82

References **85**

Publications **95**

List of Publications

This thesis is a compound thesis based on the following publications.

[P1] S. Singh, L. Anttila, M. Epp, W. Schlecker, and M. Valkama, "Frequency Response Mismatches in 4-channel Time-Interleaved ADCs: Analysis, Blind Identification, and Correction," *IEEE Transactions on Circuits and Systems I: Regular Papers*, vol. 62, no. 9, pp. 2268 – 2279, September 2015. DOI: 10.1109/TCSI.2015.2459554

[P2] S. Singh, L. Anttila, M. Epp, W. Schlecker, and M. Valkama, "Analysis, Blind Identification, and Correction of Frequency Response Mismatch in Two-Channel Time-Interleaved ADCs," *IEEE Transactions on Microwave Theory and Techniques*, vol. 63, no. 5, pp. 1721–1734, May 2015. DOI: 10.1109/TMTT.2015.2409852

[P3] S. Singh, M. Valkama, M. Epp, and W. Schlecker, "Digitally Enhanced Wideband I/Q Downconversion Receiver with 2-channel Time-Interleaved ADCs," *IEEE Transactions on Circuits and Systems II: Express Briefs*, vol. 63, no. 1, pp. 29–33, January 2016. DOI: 10.1109/TCSII.2015.2468923

[P4] S. Singh, M. Valkama, M. Epp, and W. Schlecker, "Frequency Response Mismatch Analysis in Time-Interleaved Analog I/Q Processing and ADCs," *IEEE Transactions on Circuits and Systems II: Express Briefs*, vol. 62, no. 6, pp. 608–612, June 2015. DOI: 10.1109/TCSII.2015.2406781

[P5] S. Singh, M. Valkama, M. Epp, L. Anttila, W. Schlecker and E. Ingber, "Digital correction of frequency response mismatches in 2-channel time-interleaved ADCs

using adaptive I/Q signal processing," *Journal of Analog Integrated Circuits and Signal Processing*, vol. 82, no. 3, pp. 543–555, March 2015. DOI: 10.1007/s10470-014-0476-9

[P6] S. Singh, M. Valkama, M. Epp, and W. Schlecker, "Low-Complexity Digital Correction of 4-Channel Time-Interleaved ADC Frequency Response Mismatch using Adaptive I/Q Signal Processing," in *Proceedings of the IEEE Global Conference on Signal and Information Processing (GlobalSIP 2015)*, Orlando, Florida, USA, December 2015, pp. 250–254. DOI: 10.1109/GlobalSIP.2015.7418195

[P7] S. Singh, M. Epp, G. Vallant, M. Valkama, and L. Anttila, "A Blind Frequency Response Mismatch Correction Algorithm for 4-Channel Time-Interleaved ADC," in *Proceedings of the IEEE International Symposium on Circuits and Systems (ISCAS 2014)*, Melbourne, Australia, June 2014, pp. 1304–1307. DOI: 10.1109/ISCAS.2014.6865382

[P8] S. Singh, M. Epp, G. Vallant, M. Valkama and L. Anttila, "2-channel Time-Interleaved ADC frequency response mismatch correction using adaptive I/Q signal processing," in *Proceedings of the IEEE 56th International Midwest Symposium on Circuits and Systems (MWSCAS 2013)*, Columbus, Ohio, USA, Aug. 2013, pp. 1079–1084. DOI: 10.1109/MWSCAS.2013.6674840

Abbreviations

ACF	Auto-correlation function
ADC	Analog-to-digital-converter
ASP	Analog signal processing
BB	Baseband
BPF	Band-pass filter
BW	Bandwidth
CACF	Complementary auto-correlation function
CBA	Circularity-based algorithm
CT	Continuous-time
DAC	Digital-to-analog-converter
DDC	Direct-downconversion
DSP	Digital signal processing
DT	Discrete-time
ERBW	Effective resolution bandwidth
FIR	Finite impulse response
FPBW	Full power bandwidth
FPGA	Field programmable gate arrays
FRM	Frequency response mismatch
FS	Full scale
FT	Fourier Transform
HPF	High-pass filter
HT	Hilbert Transform
HW	Hardware

I/Q	In-phase/quadrature
IC	Integrated circuit
LPF	Low-pass filter
LSB	Least significant bit
MFI	Mirror frequency interference
MIS	Mismatch identification signal
MSB	Most significant bit
OFDM	Orthogonal frequency division multiplexing
QPSK	Quadrature phase shift keying
RF	Radio frequency
RRR	Replica rejection ratio
SAR	Successive approximation register
SDR	Software defined radio
SINAD	Signal to noise and distortion ratio
SOS	Second order statistics
SW	Software
T&H	Track & hold
TI-ADC	Time interleaved analog-to-digital-converter

Symbols and Notations

$B_{4,2,1}(j\Omega)$	1st undesired I/Q signal pair formed in $I_{4,2B}(j\Omega)$.
$B_{4,2,2}(j\Omega)$	2nd undesired I/Q signal pair formed in $I_{4,2B}(j\Omega)$.
$B_{4,2,3}(j\Omega)$	3rd undesired I/Q signal pair formed in $I_{4,2B}(j\Omega)$.
$B_{4,2,4}(j\Omega)$	4th undesired I/Q signal pair formed in $I_{4,2B}(j\Omega)$.
c_τ	Complementary autocorrelation function with time lag τ.
γ_τ	Autocorrelation function with time lag τ.
δ(t)	Dirac pulse.
f	Frequency variable.
F_s	Sampling rate;$F_s = 1/T_s$.
$g_0(t)$	Impulse response of ADC0.
$G_0(j\Omega)$	Frequency response of ADC0.
$g_1(t)$	Impulse response of ADC1.
$G_1(j\Omega)$	Frequency response of ADC1.
$g_2(t)$	Impulse response of ADC2.
$G_2(j\Omega)$	Frequency response of ADC2.
$g_3(t)$	Impulse response of ADC3.
$G_3(j\Omega)$	Frequency response of ADC3.
$g_{I,BB}(t)$	I-branch impulse response at BB before the ADC.
$G_{I,BB}(j\Omega)$	I-branch frequency response at BB before the ADC.

$g_{I,RF}(t)$	I-branch impulse response at RF before the ADC.
$G_{I,RF}(j\Omega)$	I-branch frequency response at RF before the ADC.
$g_n(t)$	Impulse response of n-th ADC.
$G_n(j\Omega)$	Frequency response of n-th ADC.
$g_{Q,BB}(t)$	Q-branch impulse response at BB before the ADC.
$G_{Q,BB}(j\Omega)$	Q-branch frequency response at BB before the ADC.
$g_{Q,RF}(t)$	Q-branch impulse response at RF before the ADC.
$G_{Q,RF}(j\Omega)$	Q-branch frequency response at RF before the ADC.
$H_0(j\Omega)$	Frequency response of $V(j\Omega)$ after the I/Q downconversion, before the ADC.
$H_1(j\Omega)$	Frequency response of $V^*(-j\Omega)$ after the I/Q downconversion, before the ADC.
$h_{2,0}(t)$	Impulse response of 2-channel TI-ADC's desired signal component.
$H_{2,0}(j\Omega)$	Frequency response of 2-channel TI-ADC's desired signal component.
$h_{2,1}(t)$	Impulse response of 2-channel TI-ADC's interleaving spur component.
$H_{2,1}(j\Omega)$	Frequency response of 2-channel TI-ADC's interleaving spur component.
$h_{4,0}(t)$	Impulse response of 4-channel TI-ADC's desired signal component.
$H_{4,0}(j\Omega)$	Frequency response of 4-channel TI-ADC's desired signal component.
$h_{4,1}(t)$	Impulse response of 4-channel TI-ADC's 1st interleaving spur component.
$H_{4,1}(j\Omega)$	Frequency response of 4-channel TI-ADC's 1st interleaving spur component.
$h_{4,2}(t)$	Impulse response of 4-channel TI-ADC's 2nd interleaving spur component.
$H_{4,2}(j\Omega)$	Frequency response of 4-channel TI-ADC's 2nd interleaving spur component.
$h_{4,3}(jt)$	Impulse response of 4-channel TI-ADC's 3rd interleaving spur component.
$H_{4,3}(j\Omega)$	Frequency response of 4-channel TI-ADC's 3rd interleaving spur component.
$h_{BP}(t)$	Impulse response of the bandpass filter.
$H_{BP}(j\Omega)$	Fourier transform of $h_{BP}(t)$.
$h_{HP}(t)$	Impulse response of the highpass filter.
$H_{HP}(j\Omega)$	Fourier transform of $h_{LP}(t)$.

$h_{HT}(t)$	Impulse response of the lowpass filter.
$H_{HT}(j\Omega)$	Fourier transform of $h_{HT}(t)$.
$H_{I0}(j\Omega)$	Frequency response of desired signal component in $V_I(j\Omega)$in the 2-channel IQ-TIC architecture output.
$H_{I1}(j\Omega)$	Frequency response of interleaving spur component in $V_I(j\Omega)$in the 2-channel IQ-TIC architecture output.
$h_{LP}(t)$	Impulse response of the lowpass filter.
$H_{LP}(j\Omega)$	Fourier transform of $h_{LP}(t)$.
$H_{m,n}(j\Omega)$	N-th combination of the individual ADCs' frequency responses in m-channel TI-ADC
$H_{Q0}(j\Omega)$	Frequency response of desired signal component in $V_Q(j\Omega)$in the 2-channel IQ-TIC architecture output.
$H_{Q1}(j\Omega)$	Frequency response of interleaving spur component in $V_Q(j\Omega)$in the 2-channel IQ-TIC architecture output.
$H_{T0}(j\Omega)$	Frequency response of $V(j\Omega)$ in the 2-channel IQ-TIC architecture output.
$H_{T1}(j\Omega)$	Frequency response of $V^*(-j\Omega)$ in the 2-channel IQ-TIC architecture output.
$H_{T2}(j\Omega)$	Frequency response of $V(j\Omega)$ in the 2-channel IQ-TIC architecture output.
$H_{T3}(j\Omega)$	Frequency response of $V^*(-j\Omega)$ in the 2-channel IQ-TIC architecture output.
Im{.}	Imaginary part of signal.
$i_{2,1}(t)$	Mismatch identification signal for recreating $k_{2,1}(t)$ in the *Type I* 2-channel TI-ADC FRM.
$I_{2,1}(j\Omega)$	Fourier transform of $i_{2,1}(t)$.
$i_{2,2}(t)$	Mismatch identification signal for $k_{2,1}(t)$ in the *Type II* 2-channel TI-ADC FRM.
$I_{2,2}(j\Omega)$	Fourier transform of $i_{2,2}(t)$.
$i_{4,2}(t)$	Mismatch identification signal for recreating $k_{4,2}(t)$ in the *Type I* 2-channel TI-ADC FRM.
$I_{4,2}(j\Omega)$	Fourier transform of $i_{4,2}(t)$.
$I_{4,2D}(j\Omega)$	Desired I/Q signal pairs formed in $I_{4,2}(j\Omega)$.
$I_{4,2B}(j\Omega)$	Undesired I/Q signal pairs formed in $I_{4,2}(j\Omega)$.
$i_{k4,13}(t)$	Mismatch identification signal for recreating $k_{4,1}(t)$in the *Type II* 4-channel TI-ADC FRM.
$I_{k4,13}(j\Omega)$	Fourier transform of $i_{4,13}(t)$.
$i_{k4,2}(t)$	Mismatch identification signal for recreating $k_{4,2}(t)$ in the *Type II* 4-channel TI-ADC FRM.
$I_{k4,2}(j\Omega)$	Fourier transform of $i_{4,2}(t)$.

$IQ_{2,2a}(j\Omega)$	I/Q mismatch pair 1 in $i_{2,2}(t)$ of the *Type II* 2-channel TI-ADC FRM.
$IQ_{2,2b}(j\Omega)$	I/Q mismatch pair 2 in $i_{2,2}(t)$ of the *Type II* 2-channel TI-ADC FRM.
$IQ_{4,1,1}(j\Omega)$	I/Q mismatch pair 1 in $i_{4,1}(t)$of the *Type I* 2-channel TI-ADC FRM.
$IQ_{4,1,2}(j\Omega)$	I/Q mismatch pair 2 in $i_{4,1}(t)$of the *Type I* 2-channel TI-ADC FRM.
$IQ_{4,1,3}(j\Omega)$	I/Q mismatch pair 3 in $i_{4,1}(t)$of the *Type I* 2-channel TI-ADC FRM.
$IQ_{4,3,1}(j\Omega)$	I/Q mismatch pair 1 in $i_{4,3}(t)$ of the *Type I* 2-channel TI-ADC FRM.
$IQ_{4,3,2}(j\Omega)$	I/Q mismatch pair 2 in $i_{4,3}(t)$ of the *Type I* 2-channel TI-ADC FRM.
$IQ_{4,3,3}(j\Omega)$	I/Q mismatch pair 3 in $i_{4,3}(t)$ of the *Type I* 2-channel TI-ADC FRM.
$IQ_{k4,1}(j\Omega)$	I/Q mismatch pair in $i_{k4,13}(t)$ for the identification of $k_{4,1}(j\Omega)$ in the *Type II* 4-channel TI-ADC FRM.
$IQ_{k4,2}(j\Omega)$	I/Q mismatch pair in $i_{k4,2}(t)$ for the identification of $k_{4,2}(j\Omega)$ in the *Type II* 4-channel TI-ADC FRM.
$IQ_{k4,3}(j\Omega)$	I/Q mismatch pair in $i_{k4,13}(t)$ for the identification of $k_{4,3}(j\Omega)$ in the *Type II* 4-channel TI-ADC FRM.
$k_{2,0}(t)$	2-channel TI-ADC's desired signal; real-valued.
$K_{2,0}(j\Omega)$	Fourier transform of $k_{2,0}(t)$.
$k_{2,0c}(t)$	Analytical version of $k_{2,0}(t)$; complex-valued.
$K_{2,0c}(j\Omega)$	Fourier transform of $k_{2,0c}(t)$ signal.
$k_{2,1}(t)$	2-channel TI-ADC's interleaving spur's signal; real-valued.
$K_{2,1}(j\Omega)$	Fourier transform of $k_{2,1}(t)$.
$k_{2,1c}(t)$	Analytical version of $k_{2,1}(t)$; complex-valued.
$K_{2,1c}(j\Omega)$	Fourier transform of $k_{2,1c}(t)$ signal.
$k_{4,0}(t)$	4-channel TI-ADC's desired signal; real-valued.
$K_{4,0}(j\Omega)$	Fourier transform of $k_{4,0c}(t)$.
$k_{4,0c}(t)$	Analytical version of 4-channel TI-ADC's desired signal; complex-valued.
$K_{4,0c}(j\Omega)$	Fourier transform of $k_{4,0c}(t)$.
$k_{4,1}(t)$	4-channel TI-ADC's 1st interleaving spur's signal; real-valued.
$K_{4,1}(j\Omega)$	Fourier transform of $k_{4,1c}(t)$.
$k_{4,1c}(t)$	Analytical version of 4-channel TI-ADC's 1st interleaving spur's signal; complex-valued.
$K_{4,1c}(j\Omega)$	Fourier transform of $k_{4,1c}(t)$.
$k_{4,2}(t)$	4-channel TI-ADC's 2nd interleaving spur's signal; real-valued.

$K_{4,2}(j\Omega)$	Fourier transform of $k_{4,2c}(t)$.
$k_{4,2c}(t)$	Analytical version of 4-channel TI-ADC's 2nd interleaving spur's signal; complex-valued.
$K_{4,2c}(j\Omega)$	Fourier transform of $k_{4,2c}(t)$.
$k_{4,3}(t)$	4-channel TI-ADC's 3rd interleaving spur's signal; real-valued.
$K_{4,3}(j\Omega)$	Fourier transform of $k_{4,3c}(t)$.
$k_{4,3c}(t)$	Analytical version of 4-channel TI-ADC's 3rd interleaving spur's signal; complex-valued.
$K_{4,3c}(j\Omega)$	Fourier transform of $k_{4,3c}(t)$.
$K_{4,mc,F}(j\Omega)$	1st half of $K_{4,mc}(j\Omega)$; $k\Omega_s/2 \leq \Omega < (k+0.5)\Omega_s/2$.
$K_{4,mc,S}(j\Omega)$	2nd half of $K_{4,mc}(j\Omega)$;$(k+0.5)\Omega_s/2 \leq \Omega < (k+1)\Omega_s/2$.
$k_{m,n}(t)$	Signal resulting from the m-channel TI-ADC's n-th complex phasor summation.
$K_{m,n}(j\Omega)$	Fourier transform of $k_{m,n}(t)$.
$k_{m,nc}(t)$	Analytical version of signal $k_{m,n}(t)$.
$K_{m,nc}(j\Omega)$	Fourier transform of $k_{m,nc}(t)$.
N_H	Number of taps for Hilbert filter.
N_{HP}	Number of taps for Highpass filter.
N_{LP}	Number of taps for Lowpass filter.
N_W	Number of taps for FRM spur correction filter.
Ω	Angular frequency variable.
Ω_{LO}	$\Omega_{LO} = 2\pi F_{LO}$.
Ω_s	$\Omega_s = 2\pi F_s$.
$\Omega_n^{[m]}$	Shorthand for $\Omega - n\Omega_s/m$.
Ω_s'	$\Omega_s = 2\pi[2F_s]$.
$p_n^{[m]}(t)$	Shorthand for $\exp(j[n\Omega_s/m]t) = \exp(j2\pi[nF_s/m]t)$.
$q_2(t)$	2-channel IQ-TIC output signal's after I/Q mismatch spur's and image of interleaving spur's correction.
$Q_2(j\Omega)$	Fourier transform of $q_2(t)$.
$q_{2a}(t)$	Signal $q_{2,up}(t)$ convoluted with bandpass filter $h_{BP}(t)$.
$Q_{2a}(j\Omega)$	Fourier transform of $q_{2a}(t)$.
$q_{2b}(t)$	Signal $q_{2,m}(t)$ convoluted with bandpass filter $h_{BP}(t)$.
$Q_{2b}(j\Omega)$	Fourier transform of $q_{2b}(t)$.
$q_{2,m}(t)$	Signal $q_{2,up}(t)$ frequency shifted by $\Omega_s'/8$.
$Q_{2,m}(j\Omega)$	Fourier transform of $q_{2,m}(t)$.

$q_{2,up}(t)$	Signal $q_2(t)$ upsampled by a factor of 2.
$Q_{2,up}(j\Omega)$	Fourier transform of $q_{2,up}(t)$.
Re{.}	Real part of signal.
$RRR_{2,1}(j\Omega)$	Replica rejection ratio in the 2-channel TI-ADC Case.
$RRR_{4,1}(j\Omega)$	Replica rejection ratio of the 1st spur in the 4-channel TI-ADC Case.
$RRR_{4,2}(j\Omega)$	Replica rejection ratio of the 2nd spur in the 4-channel TI-ADC Case.
$RRR_{4,3}(j\Omega)$	Replica rejection ratio of the 3rd spur in the 4-channel TI-ADC Case.
$RRR_{4,m}(j\Omega)$	Replica rejection ratio of the m-th spur in the 4-channel TI-ADC Case.
$s_2(t)$	2-channel IQ-TIC output signal's after I/Q mismatch spur's, image of interleaving spur's and interleaving spur's correction.
$S_2(j\Omega)$	Fourier transform of $s_2(t)$.
t	Time variable.
T_s	Sampling period.
$u_2(t)$	2-channel IQ-TIC output signal's after I/Q mismatch spur correction.
$U_2(j\Omega)$	Fourier transform of $u_2(t)$.
$v_{2I}(t)$	I-channel output signal of the 2-channel IQ-TIC's architecture.
$V_{2I}(j\Omega)$	Fourier transform of $v_{2I}(t)$.
$v_{2,IP}(t)$	Signal $v_2(t)$ interpolated by a factor of 2.
$V_{2,IP}(j\Omega)$	Fourier transform of $v_{2,IP}(t)$.
$V_{2,IQ}(j\Omega)$	I/Q image spur component in the 2-channel IQ-TIC's output.
$V_{2,IT}(j\Omega)$	Interleaving spur's image component in the 2-channel IQ-TIC's output.
$V_{2,LD}(j\Omega)$	Desired signal component in the 2-channel IQ-TIC's output.
$v_{2Q}(t)$	Q-channel output signal of the 2-channel IQ-TIC's architecture.
$V_{2Q}(j\Omega)$	Fourier transform of $v_{2Q}(t)$.
$V_{2,TI}(j\Omega)$	Interleaving spur component in the 2-channel IQ-TIC's output.
$v_{2,TI,I}(t)$	Signal $v_{2,TI}(t)$ interpolated by a factor of 2.
$V_{2,TI,I}(j\Omega)$	Fourier transform of $v_{2,TI,I}(t)$.
$v_{RF}(t)$	Signal $v(t)$ frequency shifted to RF by Ω_{LO};
$V_{RF}(j\Omega)$	FT of $v_{RF}(t)$.

$v_2(t)$	Output signal of the 2-channel IQ-TIC's architecture.
$V_2(j\Omega)$	Fourier transform of $v_2(t)$.
$V_{I,0}(j\Omega)$	Fourier transform of $v_I(t) * g_0(t)$.
$V_{I,1}(j\Omega)$	Fourier transform of $v_I(t) * g_1(t)$.
$v_I(t)$	I/Q downconverted I-channel signal with RF and BB mismatches before the ADCs.
$V_I(j\Omega)$	Fourier transform of $v_I(t)$.
$V_{I,H0}(j\Omega)$	Desired signal component in the 2-channel IQ-TIC's I-channel signal.
$V_{I,H1}(j\Omega)$	Interleaving spur component in the 2-channel IQ-TIC's I-channel signal.
$v_Q(t)$	I/Q downconverted Q-channel signal with RF and BB mismatches before the ADCs.
$V_{Q,2}(j\Omega)$	Fourier transform of $v_Q(t) * g_2(t)$.
$V_Q(j\Omega)$	Fourier transform of $v_Q(t)$.
$V_{Q,3}(j\Omega)$	Fourier transform of $v_Q(t) * g_3(t)$.
$V_{Q,H0}(j\Omega)$	Desired signal component in the 2-channel IQ-TIC's Q-channel signal.
$V_{Q,H1}(j\Omega)$	Interleaving spur component in the 2-channel IQ-TIC's Q-channel signal.
$v(t)$	Signal $x_c(t)$ frequency shifted by $-\Omega_s/4$;
$V(j\Omega)$	Fourier transform of $v(t)$.
$w_{2,1}(t)$	Compensation filter for the interleaving spur in the *type 1* 2-channel TI-ADC compensation architecture.
$W_{2,1}(j\Omega)$	Fourier transform of $w_{2,1}(t)$.
$w_{2,2}(t)$	Compensation filter for the interleaving spur in the *type 2* 2-channel TI-ADC compensation architecture.
$W_{2,2}(j\Omega)$	Fourier transform of $w_{2,2}(t)$.
$w_2(t)$	Compensation filter for the interleaving spur in the 2-channel TI-ADC compensation architecture.
$W_2(j\Omega)$	Fourier transform of $w_2(t)$.
$w_{2,IQ}(t)$	Compensation filter for the I/Q spur in the I/Q downconversion with 2-channel TI-ADC architecture.
$W_{2,IQ}(j\Omega)$	Fourier transform of $w_{2,IQ}(t)$.
$w_{2,IT}(t)$	Compensation filter for the image of the interleaving spur in the I/Q downconversion with 2-channel TI-ADC architecture.
$W_{2,IT}(j\Omega)$	Fourier transform of $w_{2,IT}(t)$.
$w_{2,TI}(t)$	Compensation filter for the interleaving spur in the I/Q downconversion with 2-channel TI-ADC architecture.
$W_{2,TI}(j\Omega)$	Fourier transform of $w_{2,TI}(t)$.

$w_{4,1}(t)$	Compensation filter for the 1st interleaving spur in the *type 1* 4-channel TI-ADC compensation architecture
$W_{4,1}(j\Omega)$	Fourier transform of $w_{4,1}(t)$.
$w_{4,2}(t)$	Compensation filter for the 2nd interleaving spur in the *type 1* 4-channel TI-ADC compensation architecture
$W_{4,2}(j\Omega)$	Fourier transform of $w_{4,2}(t)$.
$w_{4,3}(t)$	Compensation filter for the 3rd interleaving spur in the *type 1* 4-channel TI-ADC compensation architecture
$W_{4,3}(j\Omega)$	Fourier transform of $w_{4,3}(t)$.
$w_{k4,13}(t)$	Compensation filter for the 1st & 3rd interleaving spur in the *type 2* 4-channel TI-ADC compensation architecture.
$W_{k4,13}(j\Omega)$	Fourier transform of $w_{k4,13}(t)$.
$w_{k4,2}(t)$	Compensation filter for the 2nd interleaving spur in the *type 2* 4-channel TI-ADC compensation architecture.
$W_{k4,2}(j\Omega)$	Fourier transform of $w_{k4,2}(t)$.
$x_2(t)$	$x(t)$ sampled by a 2-channel TI-ADC.
$X_2(j\Omega)$	Fourier transform of $x_2(t)$.
$x_{2c,D}(t)$	Signal $x_2(t)$ frequency shifted by $-\Omega_s/4$; the same as $i_{2,1}(t)$.
$X_{2,D}(j\Omega)$	Fourier transform of $x_{2c,D}(t)$.
$x_{2c,H}(t)$	Analytical signal of $x_2(t)$ obtained via HT.
$X_{2c,H}(j\Omega)$	Fourier transform of $x_{2c,H}(t)$.
$x_{2c,m}(t)$	Signal $x_{2c,H}(t)$ frequency shifted by $\pm\Omega_s/2$.
$X_{2c,m}(j\Omega)$	Fourier transform of $x_{2c,m}(t)$.
$x_{2H}(t)$	Signal $x_2(t) * h_{HT}(t)$.
$X_{2H}(j\Omega)$	Fourier transform of $x_{2H}(t)$.
$x_{2,IQ}(t)$	Signal $x_{2c,H}(t)$ frequency shifted by $-\Omega_s/4$; the same as $i_{2,1}(t)$.
$X_{2,IQ}(j\Omega)$	Fourier transform of $x_{2,IQ}(t)$.
$x_{2,m}(t)$	Signal $x_2(t)$ frequency shifted by $\pm\Omega_s/2$.
$X_{2,m}(j\Omega)$	Fourier transform of $x_{2,m}(t)$.
$x_4(t)$	Signal $x(t)$ sampled by a 4-channel TI-ADC.
$X_4(j\Omega)$	Fourier transform of $x_4(t)$.
$x_{4c,H2}(t)$	Signal $x_{4c,H}(t)$ frequency shifted by $\pm\Omega_s/2$.
$X_{4c,H2}(j\Omega)$	Fourier transform of $x_{4c,H2}(t)$.
$x_{4c,H}(t)$	Analytical signal of $x_4(t)$ obtained via HT.
$X_{4c,H}(j\Omega)$	Fourier transform of $x_{4c,H}(t)$.
$x_{4H}(t)$	Signal $x_4(t) * h_{HT}(t)$.
$X_{4H}(j\Omega)$	Fourier transform of $x_{4H}(t)$.

$x(t)$	A CT analog signal, whose spectral content spans between $-\Omega_s/2 < \Omega < \Omega_s/2$
$x_c(t)$	Analytical signal of $x(t)$, whose spectral content spans between $0 \leq \Omega < \Omega_s/2$.
$y_2(t)$	Signal $x_2(t)$ signal after 2-channel TI-ADC FRM spur correction.
$Y_2(j\Omega)$	Fourier transform of $y_2(t)$.
$y_4(t)$	Signal $x_4(t)$ signal after 4-channel TI-ADC FRM spur $k_{4,2}(t)$'s correction.
$Y_4(j\Omega)$	Fourier transform of $y_4(t)$.
$y_{4c,1H}(t)$	Signal $y_4(t)$ highpass filtered and frequency shifted by $-\Omega_s/4$.
$Y_{4c,1H}(j\Omega)$	Fourier transform of $y_{4c,1H}(t)$.
$y_{4c,3H}(t)$	Signal $y_4(t)$ lowpass filtered and frequency shifted by $\Omega_s/4$.
$Y_{4c,3H}(j\Omega)$	Fourier transform of $y_{4c,3H}(t)$.
$y_{4c,H}(t)$	Analytical version of signal $y_4(t)$.
$Y_{4c,H}(j\Omega)$	Fourier transform of $y_{4c,H}(t)$.
$z_4(t)$	Signal $x_4(t)$ after correction of 4-channel TI-ADC FRM spurs $k_{4,1}(t)$, $k_{4,2}(t)$ and $k_{4,3}(t)$.
$Z_4(j\Omega)$	Fourier transform of $z_4(t)$.

CHAPTER 1

INTRODUCTION

1.1 Background and Research Motivation

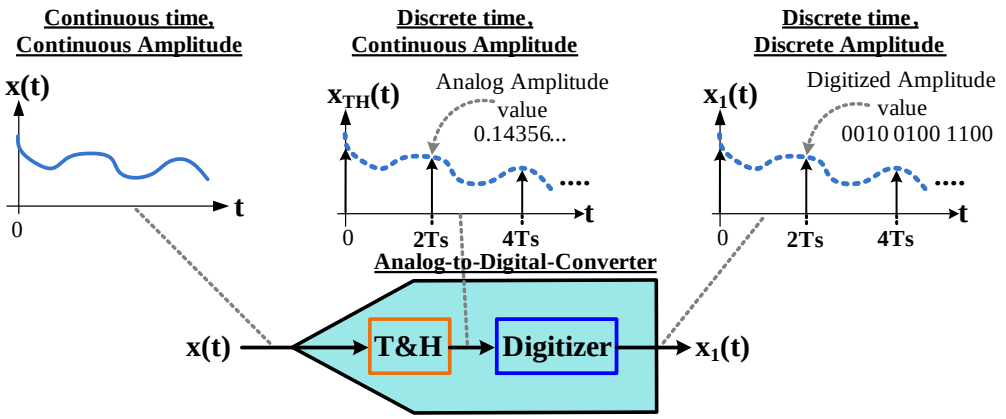

Figure 1.1: Converting an analog signal into digital form.

THE analog-to-digital-converter(ADC) is a device which measures an analog value, e.g. the voltage value of a signal, and outputs a digital value, consisting of 1's and 0's, to represent the result of the measurement. Measuring and quantizing an analog quantity into a digital value is the *raison d'êtere* of ADCs. The ADCs act as a bridge between natural world around us, which is analog in its nature, with the digital world. An analog signal is typically of continuous-time (CT) nature, i.e., the analog signal can have any given value which changes continuously w.r.t. time. The ADC quantizes the analog value of the CT in both time and value, i.e., it rounds-off at discrete time

intervals and so the digitized signal is a discrete-time (DT) version of the original analog one with discrete values [24, 54, 57]. The world around us is analog in its nature and transmitting information from one point to another, e.g. in communication systems, is commonly done using analog signals which consists of electromagnetic waves in case of radio communications. On the receiver side of this transmission, there are typically two options to process the received signal. The first option is to process the information contained in the signal in its analog form, known as analog signal processing (ASP), using analog circuitries. The second option is to convert the signal into the digital form, via the ADC, and then process it further with digital signal processing (DSP) using digital circuitry. Processing a signal after digitizing it using DSP offers some distinct advantages over processing it in analog form using ASP. Information in digital form can be processed using, e.g., processors and field programmable gate arrays (FPGA), which offer powerful computing platforms with the flexibility of defining the desired signal processing operations via software. The required computation precision in the digital domain can be arbitrarily adjusted by selecting an appropriate number of bits [24, 54, 57].

Another benefit of digital circuitry over its analog counterpart can be seen w.r.t. integrated circuits (ICs), which are of great interest when fabricating electronic circuits due to their small form factor, high power efficiency and suitability for high integration density of electronic components. The semiconductor process technology, utilized for the manufacturing of the ICs, is scaling downwards with each new process generation [7, 28, 99]. As a consequence of technology down-scaling, the size of the transistors, the elementary building blocks of circuits, is continuously decreasing. Therefore, a bigger number of circuitries can be constructed per unit area, e.g., the digital logic on a processor chip. Furthermore, the smaller transistor size leads to a smaller supply voltage. Digital circuitries benefit directly from this process technology scaling. Consequently, digital circuits are also becoming cheaper, have higher logic density and have less power consumption per unit operation. This is a strong driving factor for processing information using digital circuitry [7, 28, 99]. Unlike their digital counterparts, whose circuit functionalities remain relatively unchanged after the migration to the smaller transistor size, the functionalities of analog circuits can be effected by the transition to a smaller process technology. Smaller transistor size typically means that there is a higher degree of mismatches between the components due to the manufacturing process variations, which can affect the functionality and performance of analog circuits. Furthermore, a lower supply voltage of the transistor, due to technology down-scaling, can also affect the performance of the analog circuitry as it becomes more susceptible to noise [28, 99]. Digital circuits are clearly more robust not only against process variations but also against temperature changes, which affects the analog circuitry's functionality. Due to the aforementioned advantages, processing information using DSP is many times

favored over ASP as the former is more robust, precise, flexible and powerful signal processing tool. Therefore, the ADC is an important key element in electronic systems that desire to process information digitally [2, 7, 28].

Many electronic systems today are demanding higher data rates, larger processing bandwidth (BW) and higher resolution. This creates increasing demands on the ADC that it has to digitize a larger BW, i.e., a larger set of frequencies, and a provide a higher resolution, i.e., digitize the signal with higher number of bits and therefore digitize the signal with a higher accuracy [2, 7, 28]. Typically, an ADC has either a large digitization BW, known as its digital BW, or a high resolution with either one obtained at the cost of the other. Digitizing a larger signal BW requires that the ADC digitizes each analog sample value of the signal faster, meaning that the time window available to digitize one analog value becomes smaller. On the other hand, a longer conversion time is typically required if a more accurate digitization of the analog value is desired. This is because the ADC has to resolve the analog value of the signal from a higher number of more closely spaced quantization levels. Hence, the ADC's digital BW, determined by its operating speed, and the ADC's resolution are the bottleneck factors which restrict the performance of the electronic information processing systems which rely on DSP [2, 7, 28].

One way to overcome the dilemma of sacrificing either high conversion BW or resolution of the ADC is to utilize multiple ADCs operating in parallel. Each ADC can operate at a slower conversion rate and can therefore have the conversion time required for the targeted resolution. However, each ADC is tasked to perform the conversion at a different point in time and so each ADC provides the digitized sample value of the signal at mutually different time instants. The output of these ADCs can then be rearranged or interleaved, according to the order in which each ADC has sampled the signal, to produce a higher output data rate. This concept is known as a time interleaved analog-to-digital-converter (TI-ADC) and was first implemented in [8]. However, each of the ADCs, operating in parallel, will have a mismatch in its characteristics compared to the other ADCs. This is unavoidable due to inevitable analog circuit fabrication mismatches. These mismatches between the ADCs cause a loss in the TI-ADC's effective resolution, which may severely compromise the original goal of time interleaving the ADCs. Hence, these mismatches must be removed or mitigated to recover the TI-ADC's effective resolution, e.g., via mismatch correction techniques. So techniques and algorithms that are able to detect and correct the mismatches between the interleaved ADCs are of great interest [65, 97].

Also, each ADC has a limited analog BW, due to its analog circuitry, and the analog signal to be digitized must be located within this analog BW as the ADC's digitization performance typically degrades outside this range, i.e, the digitized value starts to deviate considerably from the original analog value. In general, time interleaving of the ADCs

only allows for increasing the total conversion BW for a certain targeted resolution as long as the total BW remains within each individual ADC's limited analog BW. Thus, during the reception of high frequency signals, transmitted, e.g., for communication purposes, frequency translation is typically carried out down to the ADC analog BW range by a receiver circuit before it can be digitized by the ADC [55, 58]. Therefore, some analog processing of the signal is typically required, depending on the used center-frequencies, to downconvert the signal into the ADC's analog BW. Hence, it is also of interest to find cost, space and power efficient methods to increase the ADC's analog BW as this will increase the overall BW of the signal that can be digitized by the ADC as well as simplify the downconversion stage. This tendency is also well in-line with the software defined radio (SDR) paradigm, where the goal is to digitize the analog signal as early as possible in the receiver chain and define and implement the rest of the receiver functionalities in DSP Software (SW) [2, 7, 28].

Hence, the importance of developing techniques to push the boundaries of the ADC's performance beyond its analog circuitry limitations is clearly evident with the ADC being a key component in the digital information processing age.

1.2 Thesis Scope and Objectives

The primary scope of this thesis is related to the frequency response mismatches (FRMs) in TI-ADCs, which were at the early stages of the thesis work one of the most critical open research challenges in the field of TI-ADCs, in particular when it comes to blind online estimation. The aim of the research work carried out in this thesis is to find suitable methods to identify and correct the TI-ADC's FRM in an adaptive and blind manner, i.e., without using known training signals and interrupting the operation of the TI-ADC. Therefore, the behavior of the TI-ADC's FRM is thoroughly studied and modeled to facilitate the achievement of this goal. Digital FRM estimation and correction algorithms are then developed, based on this modeling, to remove the FRM induced spur components and recover the TI-ADC's lost effective resolution. The work covers different kinds of TI-ADCs, namely 2-channel and 4-channel TI-ADCs with real-valued input signals as well as I/Q TI-ADCs with parallel I and Q signals. The performance and proper operation of all developed estimation and correction methods are evaluated and verified through TI-ADC hardware measurements, including also very challenging case of input waveforms with close to 1GHz instantaneous BW. The secondary scope of this thesis is to contribute to the extension of the TI-ADC's analog bandwidth.

It is also highlighted that the mitigation techniques for TI-ADCs mismatch spurs is a research topic with high industrial interest as can be seen from [13, 77, 85].

1.3 Outline and Main Results of the Thesis

The first main contribution of this thesis includes the finding that TI-ADC mismatch parameters can be identified by utilizing the mirror frequency interference techniques, which are classically encountered in the in-phase/quadrature (I/Q) direct-downconversion (DDC) transmitters and receivers. This resulted in, to the authors' best knowledge, first of its kind methods in the technical literature for solving the more challenging open challenges in the field of TI-ADCs' mismatch mitigation, i.e., the FRM correction. Firstly, it led to a new breed of solutions that allow efficient and comprehensive blind and adaptive identification of frequency dependent FRMs in the 2-channel TI-ADC case using I/Q mismatch correction solutions. Secondly, it led to the development of blind and adaptive identification of frequency dependent FRMs beyond the 2-channel TI-ADC case, e.g., the 4-channel TI-ADC case. Contributions w.r.t. this topic are listed and elaborated more specifically below.

1. *Complex modeling and analysis of FRM in real-valued TI-ADCs* [P1], [P2]. The complex modeling of the TI-ADC mismatch facilitates better understanding of the creation process and nature of the mismatch spurs due to FRM, particularly for higher order TI-ADCs. The complex model of the TI-ADC is easily mapped to the real valued TI-ADC.

2. *I/Q downconversion and 2-channel TI-ADC relationship* [P2],[P5],[P8]. It is shown in conjunction with the complex modeling mentioned above that a 2-channel TI-ADC spectrum and the I/Q DDC spectrum are connected via a lowpass bandpass transformation. Prior to this, no link was systematically established between the 2-channel TI-ADC and I/Q DDC field of work.

3. *2-channel TI-ADC frequency response mismatch correction* [P2],[P8]. The first known examples of blind adaptive FRM correction algorithms for 2- channel TI-ADCs are developed which are able to estimate and correct the FRM within the band of use without any specific calibration signals or waveforms.

4. *4-channel TI-ADC frequency response mismatch correction* [P1],[P6],[P7]. The first known examples of blind adaptive FRM correction algorithms for 4-channel TI-ADCs are developed which are able to estimate and correct the FRM within the band of use without any specific calibration signals or waveforms.

The second main contribution of this thesis is w.r.t. increasing the TI-ADC's analog BW. Here, the focus is specifically placed on the effects of FRM in wideband I/Q downconversion circuitry which utilizes TI-ADCs in its analog I and Q branches. This is followed by the estimation and correction of these FRM mismatches. Contributions w.r.t. this topic are listed and elaborated more specifically below.

5. *Modeling of wideband I/Q downconversion circuitry with 2-channel TI-ADC frequency response mismatches* [P4]. Here the interactions between the frequency response mismatches in the various analog stages, i.e., in the analog I/Q downconversion and TI-ADCs circuitry, are shown and analyzed and the nature of the resulting spur components is studied. This behavior was previously not systematically studied in the existing literature.

6. *Digital estimation and correction of frequency response mismatches in wideband I/Q downconversion circuitry with 2-channel TI-ADC* [P3]. Here the identification and compensation of the FRM spurs in the analog I/Q downconversion and the 2-channel TI-ADCs circuitry is performed. These are, to the author's best knowledge, the first known published methods and results which explicitly offers solutions to the mitigation of FRM spurs in the 2-channel I/Q TI-ADC.

7. *Relationship between 4-channel TI-ADC and I/Q downconversion circuitry with 2-channel TI-ADC* [P1]. Here it is shown that the 2-channel I/Q TI-ADC's spectrum, with its corresponding mismatches components, share a lowpass-bandpass relationship with a 4-channel TI-ADC and its corresponding FRM spurs.

1.4 Author's Contributions to the Publications

This thesis work was started in collaboration between Airbus Defence and Space GmbH and Tampere University of Technology under the scope of digitally assisted analog. The findings presented in [P1]-[P8] were developed by the author. Valuable feedback and constructive criticism were given by Prof. Dr. Mikko Valkama, Michael Epp, Dr. Lauri Antilla and Dr. Wolfgang Schlecker during the vigorous discussions and examination of the proposed FRM spurs analysis and the corresponding FRM spurs estimation and correction solutions. The findings and results of the work established a strong connection between TI-ADCs and I/Q downconversion. This allowed utilizing previously developed statistical based algorithms in the I/Q downconversion framework by Dr. Lauri Antilla and Prof. Dr. Mikko Valkama also for the TI-ADC mismatch estimation. The publications in [P1]-[P8] were vastly written by the author and Prof. Dr. Mikko Valkama contributed towards the structuring, revision as well as the final appearance of the publications. Support and proof-reading for the publications were also given by Michael Epp, Dr. Lauri Antilla and Dr. Wolfgang Schlecker.

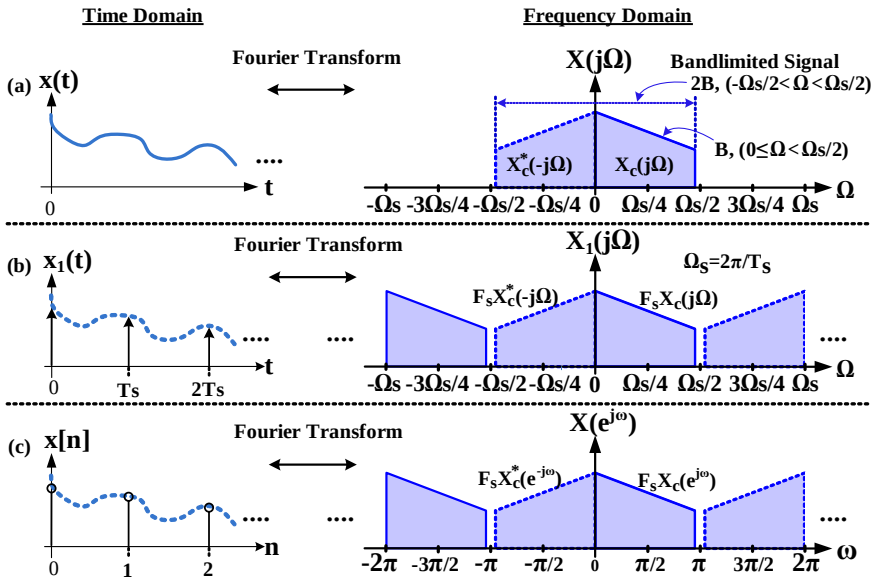

Figure 1.2: Respective spectra of continuous-time signal, discrete-time signal and discrete sequence.

1.5 Used Mathematical Notations and Basic Modeling of the Sampling Process

A time domain signal is denoted using lower case, e.g., $x(t)$ with t being the time variable and its frequency domain equivalent is denoted using upper case, e.g., $X(j\Omega)$ with $\Omega = 2\pi f$ being the angular frequency variable, f being the frequency variable in Hz and $j = \sqrt{-1}$. Re{.} denotes taking the real part of a complex signal and Im{.} denotes taking the imaginary part of the signal, i.e., $\text{Re}\{x_I(t) + jx_Q(t)\} = x_I(t)$ and $\text{Im}\{x_I(t) + jx_Q(t)\} = x_Q(t)$. The Hilbert Transform (HT) based operation on a signal, e.g., $x(t)$, is defined here as $x(t) + jh_{HT}(t) * x(t)$ with $h_{HT}(t)$ being the Hilbert filter. Such HT based operation produces a complex valued analytical signal out of $x(t)$, as elaborated further in Chapter 3. Notice that in this notation, an anti-causal (zero delay) HT is assumed, thus in practice a corresponding delay needs to be imposed accordingly in the respective branches. In the frequency domain, $X(j\Omega)$ and $X^*(-j\Omega)$ form a mirror frequency pair, which corresponds in time domain to the signal pair $x(t)$ and $x^*(t)$.

A Fourier Transform (FT) pair between time domain and frequency domain representations is denoted using $x(t)$ and $X(j\Omega)$. Performing the FT on a time domain signal, e.g., on $x(t)$ to obtain $X(j\Omega)$, enables analyzing $x(t)$'s frequency or spectral content as well as the location of the spectral content as depicted in Fig. 1.2(a). Alternatively, a

time domain signal, e.g., $x(t)$, can be synthesized from its spectral contents, i.e., $X(j\Omega)$. The FT relationship between $x(t)$ & $X(j\Omega)$ can be expressed in the form of a synthesis equation as

$$x(t) = \frac{1}{2\pi}\int_{-\infty}^{\infty} X(j\Omega)\exp(j\Omega t)d\Omega, \tag{1.1}$$

and in the form of an analysis equation as

$$X(j\Omega) = \int_{-\infty}^{\infty} x(t)\exp(-j\Omega t)dt. \tag{1.2}$$

The periodically sampled version of $x(t)$, denoted by $x_1(t)$, can be expressed or modeled mathematically as

$$x_1(t) = x(t)\sum_{k=-\infty}^{\infty}\delta(t-kT_s) \quad = \sum_{k=-\infty}^{\infty} x(kT_s)\delta(t-kT_s). \tag{1.3}$$

with k being the running integer index, T_s being the sampling interval and $\delta(t-kT_s)$ being the Dirac impulse occurring at timepoint kT_s. The FT of $x_1(t)$, denoted by $X_1(j\Omega)$, can be expressed as

$$X_1(j\Omega) = \sum_{k=-\infty}^{\infty} x(kT_s)\exp(-j\Omega kT_s). \tag{1.4}$$

Let a sequence $x[k]$ be defined representing the samples of the signal $x(t)$ sampled at intervals of kT_s, i.e., $x[k] = x(kT_s)$. The discrete-time FT of $x[k]$, $X(e^{j\omega})$, can be written as

$$X(e^{j\omega}) = \sum_{k=-\infty}^{\infty} x[k]\exp(-j\omega k). \tag{1.5}$$

From (1.4) and (1.5), the relationship $X_1(j\Omega) = X(e^{j\Omega T_s}) = X(e^{j\omega})|_{\omega=\Omega T_s}$ can be established. $X_1(j\Omega)$ can also be expressed as

$$X_1(j\Omega) = \frac{1}{2\pi}X(j\Omega) * \left(\frac{2\pi}{T_s}\sum_{k=-\infty}^{\infty}\delta(\Omega-k\Omega_s)\right) = F_s\sum_{k=-\infty}^{\infty} X(j[\Omega-k\Omega_s]), \tag{1.6}$$

with $*$ denoting convolution, $F_s = 1/T_s$ and $\Omega_s = 2\pi F_s$. The shorthand $\Omega_n^{[m]}$= $[\Omega - n\Omega_s/m]$ will be used in upcoming equations to denote translated or shifted frequencies. The shorthand $p_n^{[m]}(t)$= $\exp(j2\pi[n\Omega_s/m]t)$, denotes a complex exponential oscillating at $n\Omega_s/m$. The sampling process of the CT signal $x(t)$ is modeled using the periodically repeating Dirac pulses, in intervals of T_s, as in (1.3) and this corresponds to the convolution between $X(j\Omega)$ and the FT of the Dirac pulses in the frequency domain.

Therefore, the spectral components in $X(j\Omega)$ periodically repeat in intervals of Ω_s in $X_1(j\Omega)$ as depicted in Fig. 1.2(b). Similarly, $X(e^{j\omega})$ can also be expressed as

$$X(e^{j\omega}) = F_s \sum_{k=-\infty}^{\infty} X(j[\omega - k(2\pi)]/T_s) \tag{1.7}$$

and as is seen in Fig. 1.2(c) the only difference with the spectrum of $X_1(j\Omega)$ is the notion of normalized angular frequencies scaled by $1/T_s$ and the spectral components repeat in intervals of 2π.

In this thesis, the modeling of the TI-ADCs is carried out using the DT impulse function based signal models as in (1.3) along with its FT, $X_1(j\Omega)$, as in (1.6). The FT pair notations, e.g., $x_1(t)$ and $X_1(j\Omega)$, are used interchangeably depending on the convenience during the analysis to switch between time domain and frequency domain. Furthermore, the quantization stage and process in all the developments is neglected, and thus the focus is fully on the issues related to the sampling in terms of discretization of the time axis. In the analysis and modeling, a real-valued CT signal is frequently utilized, e.g., $x(t)$, whose spectral content is located between $-\Omega_s/2 < \Omega < \Omega_s/2$, which is then separated into its two analytical counterparts , i.e., $x_c(t)$ and $x_c^*(t)$, whose spectral content lies between $0 < \Omega \leq \Omega_s/2$ and $-\Omega_s/2 < \Omega \leq 0$ respectively, as depicted in Fig. 1.2(a). Also, due to the spectral replication in the sampled signal, only the region $-\Omega_s/2 < \Omega \leq \Omega_s/2$ is considered.

CHAPTER 2

Basic Concepts and State-of-the-Art of High Speed ADCs

This chapter gives an overview of the architectures of high speed ADCs followed by an introduction into the time interleaving of ADCs in combination with the frequency downconversion circuitry, e.g., Heterodyne and Homodyne downconversion circuitries. This forms the basis for the TI-ADC modelling carried out in chapter 3. An overview of existing TI-ADC mismatch correction methods is also provided which highlights the open challenges in the field of TI-ADCs mismatch correction and provides motivation for the new TI-ADC FRM estimation and correction methods in chapter 4.

2.1 An Overview of High Speed ADC Architectures

The two major types of ADCs are Nyquist ADCs and oversampling ADCs. In Nyquist ADCs, the sampling frequency must be more than twice the signal BW, in accordance with the Nyquist-Shannon theorem. In oversampling ADC, e.g., delta sigma ADC, the ADC's sampling frequency is typically much higher than the signal's BW, e.g., 16, 32 or 64 times higher [45]. The high oversampling is necessary to enable the quantization noise shaping mechanism which is followed by filtering of the quatization noise and decimation [45]. Nyquist ADCs are typically best suited in the construction of TI-ADCs [49]. Nyquist ADCs typically consist of a track & hold (T&H) stage and quantization stage. The T&H tracks the analog input and holds the analog value of the signal at a specific point in time. The quantizer then quantizes this analog value

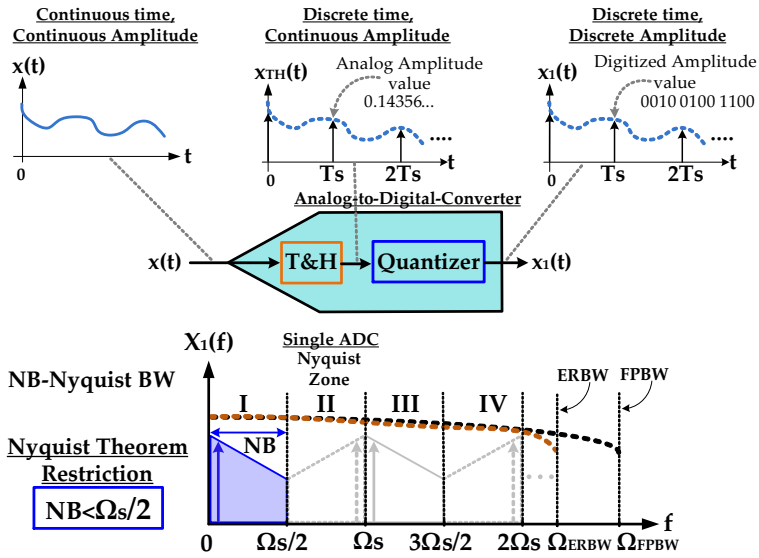

Figure 2.1: Nyquist BW and analog BW of an ADC.

and provides its digitized representation with finite accuracy. The T&H operates on the analog signal and the highest input signal frequency, for which it can capture the analog value without a 3 dB attenuation, determines the ADC's full power bandwidth (FPBW) as depicted in Fig. 2.1 [88, 89]. (Note that occasionally the terms FPBW and analog BW will be used interchangeably hereafter.) Typically, the T&H is able to operate much faster than the quantizer, i.e., the time needed by the T&H to capture the analog value of the signal is much shorter than the time needed by the quantizer to perform its quantization operation. The T&H's BW, i.e., the frequency range for which T&H can accurately hold the value of the analog signal without degrading the signal to noise and distortion ratio (SINAD) exceeding 3 dB, is referred to as the ADC's effective resolution bandwidth (ERBW). The ERBW is typically smaller than the FPBW as depicted in Fig. 2.1 [88, 89]. However, for simplicity in the discussions that follow, it is assumed that the FPBW equals the ERBW and the two terms will be used interchangeably.

Most ADC architectures typically differ in their quantizer architecture, which clearly impacts the quality of the amplitude quantization and therefore the ADC's effective resolution [12, 43, 49, 78]. Currently, the ADC architectures used in high speed ADCs with resolutions ranging from $10 - 16$ bits include folding-interpolating, successive approximation register (SAR), pipeline architecture as well as hybrid versions of the aforementioned architectures [1, 11, 12, 49, 75, 78]. The basic work principle of these ADC architectures are explained briefly below. The folding-interpolating architecture is built upon the flash ADC architecture where one flash ADC is used to perform coarse

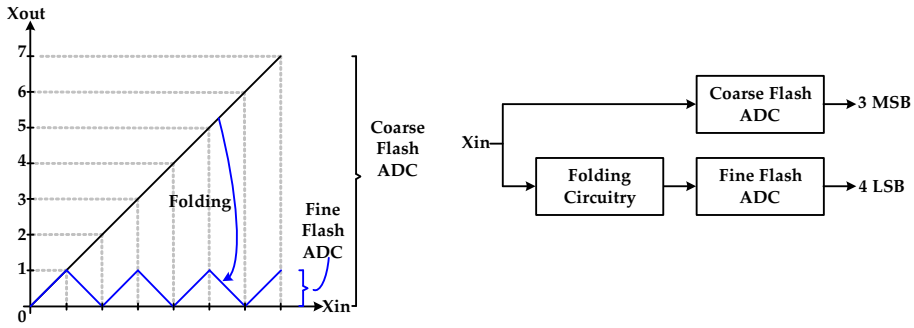

Figure 2.2: Folding-interpolating ADC architecture operating principle.

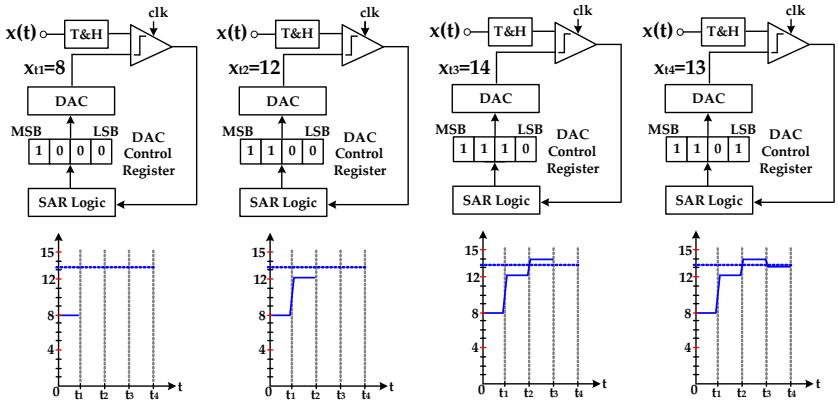

Figure 2.3: SAR ADC architecture operating principle.

quantization and another flash ADC is used to perform a finer quantization [22, 34, 91]. The coarse quantization gives the most significant bits (MSBs) and the fine quantization provides the least significant bits (LSBs) as shown in Fig. 2.2. The coarse quantization path consists simply of a typical flash ADC architecture. The fine quantization path consist of a folding circuitry which folds the analog input signal into the smallest quantization level of the coarse quantization ADC, which is then interpolated before being fed into the flash ADC [22, 34, 91].

Then, there is the SAR ADC architecture which consists generally of a T&H, a comparator, SAR logic and a digital-to-analog-converter (DAC) as seen in Fig. 2.3 [33, 78, 79]. The analog value held by the T&H is compared with the analog value generated by the DAC using the comparator. The output of the comparator is recorded by the SAR logic. The SAR logic controls the DAC to generate various analog voltages, starting with ADC's MSB followed by the next significant bit and this is repeated until the ADC's LSB is reached. The comparator output information is used by the SAR logic to determine if the DAC generated analog value is above or below the input value and the goal is to find which voltage level is the closest. If the voltage value of the DAC

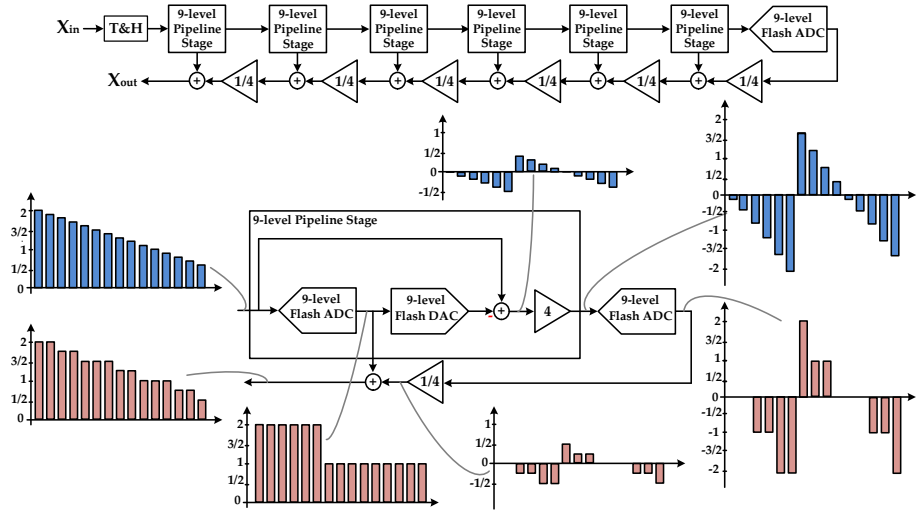

Figure 2.4: Pipeline ADC architecture operating principle.

exceeds the analog input value, then the current bit is set to 0 in the next cycle, where the next significant bit is set to 1. The SAR ADC conversion process is depicted in Fig. 2.3.

Next, the pipeline ADC architecture is explored. The pipeline ADC employs multiple cascaded pipeline stages consisting of a flash ADC, a DAC and a differential operational amplifier [1, 11, 25, 38, 43, 53, 75]. In the first stage, the signal is quantized using a low resolution flash ADC and then this quantized digital signal is converted back into an analog signal via the DAC. The analog value generated by the DAC is subtracted from the original signal to produce the quantization error in the analog form. Subsequent pipeline stages only process the quantization error in its analog form. The analog quantization error is amplified, quantized and then divided before being added to the original quantized signal. Each consecutive pipeline stage further minimizes the quantization error which allows constructing a high precision ADC with a low quantization error.

It can be partially seen through the operating principle of the ADC architectures that in order to achieve high ADC resolution with minimal quantization error, a sufficient time window must be allocated during the conversion of each analog sample value. For example, the comparator circuitry requires sufficient regeneration time to reduce its metastability error and the operational amplifier requires sufficient settling time during its amplification stage [43]. There is also a large increase in the ADC's power consumption, e.g. due to the amplifier and comparator, whose power consumption increases in a non-linear fashion as their operating speed approaches the limit of the given technology [12, 43, 78]. Therefore, the conversion rate of the ADC, for a certain target accuracy and reasonable power consumption, is limited.

2.2 Time Interleaving of ADCs

High conversion speed and high resolution are typically contradictory requirements in an ADC, i.e., one requirement is obtained at the price of sacrificing the other [49]. High conversion speed leads to a higher Nyquist BW but achieving a more accurate quantization generally requires allocating more time for conversion. Since the conversion time for accurate quantization bottlenecks the achievable conversion speed, one way to increase the conversion output rate would be to have multiple ADCs operating in parallel with each ADC performing the conversion process at the same rate but at a different point in time. The outputs of each ADC are then arranged in accordance with the sampling sequence of the respective ADCs to produce a higher output rate. This concept is known as the time interleaving of ADCs [8, 79].

If a single ADC is able to achieve the required sampling rate, with the desired conversion accuracy and power efficiency, then it would be the sensible to only utilize a single ADC for sampling the desired signal as shown in Fig. 2.5 a). If a single ADC cannot achieve this sample rate, then two ADCs can be time interleaved to achieve the desired sample rate, as depicted in Fig. 2.5 b) [61, 79]. Unfortunately, the mismatches between the two interleaved ADCs cause spurious components to appear in the spectrum, as seen in Fig. 2.5 b), and this leads to a loss in the effective resolution of the ADC. These mismatches between the ADCs can severely reduce the benefit of interleaving the ADCs [65, 97]. The linear mismatches in TI-ADCs can be separated into the channel offset mismatch and the FRM, which consist of frequency dependent gain and phase mismatch. These mismatches cause a deviation of sample value from the original value as shown in Fig. 2.6 [37]. The modeling of the FRMs and their effects on the TI-ADCs is done in chapter 3.

2.3 Downconversion Circuitry and TI-ADCs

Although time interleaving the ADCs increases the ADC's Nyquist BW, the spectrum to be sampled by the ADC must be located within the ADC's analog BW as shown in Fig. 2.5. In most cases, however, the signal to be digitized is located at higher frequencies outside the FPBW of the TI-ADC. Therefore, downconversion circuitries are required to translate the frequency band of interest into a lower frequency range, within the ADC's analog BW.

2.3.1 Real Sampling TI-ADCs

The Heterodyne receiver architecture is one option to downconvert the signal to be digitized into the ADC analog BW. With the emergence of radio frequency (RF) sampling

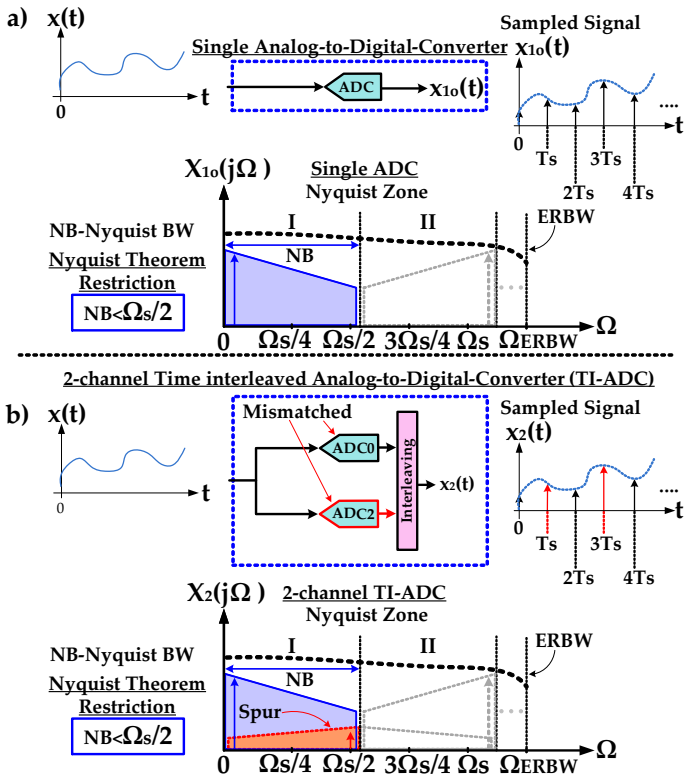

Figure 2.5: Example of time interleaved ADC.

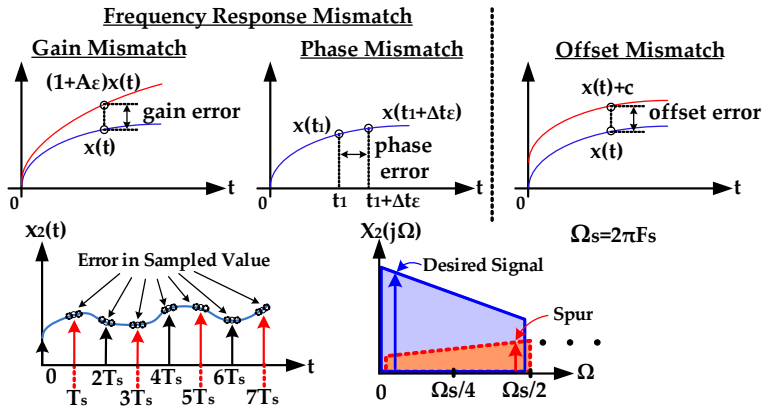

Figure 2.6: Overview of linear mismatches in time interleaved ADCs.

TI-ADCs, e.g. [3, 80, 82], signals located up to ~ 3 GHz can be sampled directly without the need of any downconversion circuitry. However, digitization of any frequency band located higher than the ADC's analog BW will require downconversion circuitry. In

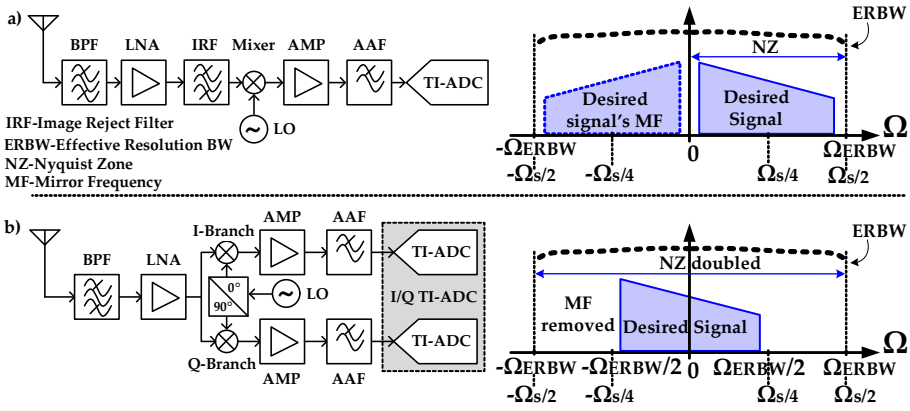

Figure 2.7: Downconversion circuitry with time interleaved ADCs.

this configuration, only a single real-valued TI-ADC output stream is produced as depicted in Fig. 2.7 a). The Heterodyne architecture requires high performance RF image rejection filters and it is challenging to implement as an IC solution [7, 89]. After the real downconversion, the signal is sampled in real-valued form and the final complex down-conversion to baseband, i.e., I/Q generation is done digitally. The total BW of the downconverted signal must be be less than the ERBW of the ADC [89], i.e. the signal's BW must be less than the ADC's ERBW angular frequency, Ω_{ERBW}, as seen in Fig. 2.7 a).

2.3.2 I/Q Sampling TI-ADCs

As an alternative to the real valued Heterodyne downconversion, I/Q downconversion may be used via the Homodyne circuitry, which results in a quadrature pair output stream as seen in Fig. 2.7 b). The Homodyne architecture consist of more simple analog components with less stringent analog performance requirements, especially in terms of RF image rejection filtering, compared to the heterodyne downconversion circuitry [7, 86, 89]. However, it suffers from the mirror frequency interference due to finite matching of its I and Q branch [7, 86, 89]. Utilizing the I/Q downconversion provides also the benefit of removing the mirror frequency component, which leads to the doubling of the ADC's ERBW compared to the same ADC used injunction with a Heterodyne receiver, as seen in Fig. 2.7 a).

2.4 An Overview of existing TI-ADC Mismatch Correction Methods

The potential of TI-ADCs has fueled much research efforts in their development from the circuit designer community [12, 27, 43, 78]. Similarly, the TI-ADC's performance enhancement via the mitigation of the unavoidable analog mismatches has equally received a lot of attention [17, 19, 35, 44, 48, 50, 59, 61, 62, 65, 90, 96, 100–102]. The individual types of mismatches that occur in the TI-ADC, i.e., gain, timing and offset mismatches, have been discussed and analyzed extensively in, e.g., [18, 37, 92]. This section aims to survey the available background TI-ADC mismatch correction techniques, capable of mitigating the mismatches beyond the 2-channel TI-ADC case. The two current mainstream mismatch correction solutions researched are mixed-signal domain solutions and all-digital domain solutions. Both of these approaches perform interleaving mismatch detection in the digital domain using DSP. Due to DSP's mismatch detection accuracy and robustness against variation effects it achieves good mismatch parameter identification results. Once the mismatch detection is done, the mismatch correction can then be done either in the analog domain, e.g. via circuit parameter tuning for the mixed domain solutions, or in the digital domain e.g. via the digital correction filter.

Many mismatch calibration techniques developed focused on static gain, timing and offset mismatch correction [17, 19, 35, 44, 50, 59, 61, 62, 90, 96, 100–102]. For mediocre resolution TI-ADC, e.g. 8-10 bits, it is sufficent to correct these frequency independent mismatches [29]. Global frequency independent mismatch parameter detection is generally easier compared to frequency dependent mismatches [50]. Static gain and offset mismatch parameters are the easiest to detect and correct [50]. The timing mismatch's detection is more difficult and its correction more challenging due to the frequency dependent linear phase mismatch caused by the sample time offset mismatch [50, 94]. Frequency dependent mismatches' detection is more challenging than the aforementioned mismatches as it involves detecting frequency dependent gain and phase mismatch. Frequency dependent mismatches are the main research topic of this thesis work, and have been earlier identified as the main research challenge in the TI-ADC field in [50, 93, 94].

2.4.1 Mixed-signal Correction Methods

Mixed-signal domain correction methods focus mainly on the timing mismatch detection and correction [16, 60, 61, 74, 78]. In these methods, first the timing mismatch parameter identification is done in the digital domain followed by fine-tuning of the ADC sample clock phase in the analog domain to minimize the sample time offset [15, 16, 43, 60, 61, 74, 78]. Background timing mismatch estimation is done e.g. by utilizing statistical properties of the signal [43, 60, 74] and the ADC clock phase is then fine-tuned to

remove the sample time offset. This enables a power efficient correction method with low complexity, in contrast to digital correction filters. It tackles the timing mismatch problem at its source and allows for a timing mismatch correction throughout the full Nyquist zone, an advantage over digital correction filters which typically require some oversampling [74]. It can be easily scaled to an arbitrary number of ADC channels, provided however that the individual ADC timing mismatch parameter values have been extracted. It does, however, come with an analog circuit challenge to design a variable delay line which does not increase the ADC's aperture jitter for a target sampling frequency causing a degradation to its signal-noise-ratio (SNR) [16, 50, 61, 74, 78]. This needs to be redesigned if a technology migration is made. The method in [74] relies on the wide-sense-stationary (WSS) property of the TI-ADC output signal and attempts to restore the assumed shift-invariance of the auto-correlation function by iteratively searching for the timing mismatch value in a 4-channel TI-ADC case and also include the static gain mismatch correction.

The non-blind correction methods involve deploying certain specific reference signals obtained via additional hardware e.g. from an auxiliary ADC channel that operates in parallel. Using a reference channel, a non-blind method in [16] estimates the timing mismatch by measuring the cross-correlation between the reference channel to the respective ADC branches. A different non-blind calibration technique is presented in [78], which also uses a reference ADC channel to obtain the sample value deviation and then uses the least-mean-square (LMS) algorithm to estimate the sample time offset. A timing mismatch detection algorithm for the 2-channel TI-ADC case is presented in [60, 61]. By summing up the multiplication product between the time shifted output samples of the two ADC, a DC term is generated in the presence of a timing mismatch which is used as reference for the ADC clock phase adjustment. The techniques listed above have been mostly tested using a single tone CW signal and shown to require multiple iteration cycles before reaching convergence (e.g. [74] required 300 search iterations and [61] required 12 x 8k clock cycles). In summary, correction in the analog domain typically involves only the global mismatches (gain, timing and offset mismatch) and the effects of the frequency specific mismatches are tried to be minimized through design and monolithic implementation [48, 78].

2.4.2 All-Digital Correction Methods

The all-digital domain solutions utilize DSP algorithms for both detection and mitigation of the TI-ADC mismatches. The mitigation of ADC non-idealities in the digital domain is an idea that dates back to the early days of data converters [48]. All digital correction algorithms are independent of the ADC's semiconductor technology, are not effected by process variations and benefits from technology down-scaling [48, 94]. One of the first

example was published in [25, 26] which involved extracting the static gain and timing mismatch parameters before performing the correction in the digital domain for the 2-channel TI-ADC case. The basic idea is to align interleaving spur with the input signal and measure the correlation between the two in order to estimate the static gain and timing mismatch parameters. These parameters were extracted separately as the gain and timing mismatch component are mutually orthogonal [25, 26]. This method was later extended to the 4-channel TI-ADC case in [38]. An early attempt in the combined estimation of the static gain and timing mismatch was probably first done in [73] for 2 TI-ADCs which is based on restoring the assumed WSS property of the TI-ADC output. It uses a parametrized filter banks to make the auto-correlation function shift-invariant by iteratively adjusting the static gain and timing mismatch in each channel. The same principle of WSS restoration is applied to the 4-channel TI-ADC mixed-signal domain mismatch correction solution in [74]. In [46, 47], a mismatch compensation technique is presented which aims to correct M-channel TI-ADC's static gain and timing mismatch. It generates $M-1$ pseudo aliases and then performs the frequency alignment followed by measuring the correlation for estimating the static gain and timing mismatch separately. Another scalable structure for the correction of static gain and timing mismatch is presented in [96]. It requires some degree of oversampling to allocate a region where the interleaving mismatch components are present separately from the desired signal. The desired signal must also have interleaving spurs which fall into this allocated region to obtain a reference for the mismatch parameter identification.

A 4-channel TI-ADC timing offset correction is presented in [23] which also uses oversampling and adaptive null steering filter bank to estimate the timing mismatch. An M-channel TI-ADC timing mismatch identification using oversampling was proposed in [69]. Another strategy involves using tone injection to identify the interleaving mismatch parameter in a semi-blind way. Such methods requires allocating two regions in the spectrum; one region where the test tone can be injected and the other region where its interleaving spur is positioned. The method proposed in [20, 21] uses tone injection to estimate the static gain and timing mismatch. Tone injection methods for the TI-ADC mismatch identification have complications when going beyond the 2 TI-ADC case, e.g., for the 4 TI-ADC case where the other two interleaving FRM spurs fall into different regions of the spectrum. These regions have to be kept free for this reason and causes the usable spectrum to become fragmented, which in some applications can easily be undesirable or unacceptable. Correcting only the TI-ADC's static gain and linear phase mismatch (from timing mismatch) causes a residual frequency dependent gain and phase mismatch to remain. This restricts the post correction improvement of the interleaving mismatches, which naturally limits the effective resolution in higher resolution TI-ADCs [29].

Up until around 2007, known blind mismatch identification techniques focused on extracting static gain and timing mismatch parameters only. Then, the question on how to estimate the frequency dependent mismatches in TI-ADC was opened [71]. In an offline procedure with a dedicated measurement setup, CW single tone calibration signals can be injected sequentially to characterize the individual ADC's FRM followed by a filter design to compensate the FRMs [72]. Such a method, however, is susceptible to mismatch variations that occur over time which led to the mentioned performance degradation of the designed filter in [72]. Recalibration would be required and this would mean interrupting the system's operation. Online calibration methods are thus of interest as these methods run in the background and do not interrupt the system's operation. However, online blind identification of the TI-ADC's FRM is also the most challenging to do. A semi-blind method which tackles the relative bandwidth mismatch detection between the T&H's of two interleaved ADC is described in [66, 67]. It models the T&H as a first-order RC circuit and the relative mismatch between the T&Hs is extracted using the mismatch spur information of the injected tone.

A proposal for using polynomial based mismatch modeling was made in [70, 71] and was equally adopted by solutions developed further in [29, 64]. Static gain and timing mismatches correspond to the 1st order polynomial approximation of the FRM [64]. The method in [73] is extended for correcting frequency dependent gain and phase mismatch in 2 TI-ADC using polynomial modeling by the investigations carried out in [70, 71].The mismatch correction principle was illustrated with a second-order polynomial mismatch model, which required about 500 search iterations on a 10^6 sample data set to estimate the mismatch parameters that restore the assumed WSS property in the TI-ADC's output signal using 61-tap filters. It is stated that the proposed method requires the condition that the desired signal and interleaving spur component do not overlap and such a multitone CW scenario was used in the verification of the proposed method. The method's suitability for real-time mismatch identification needs to be validated as well as showing its extendability beyond the 2-channel case. Also, the actual TI-ADC mismatches will need a higher order polynomial to be corrected [29, 64]. The method in [64] relies on oversampling to have a region in the spectrum where only the interleaving mismatch spurs are present. This is used as reference to adaptively identify the polynomial coefficients needed to reconstruct an estimate of the spur component before subtracting it from the TI-ADC output signal, thus suppressing the spur components. One limitation here is that since the reference for the adaptation only comes from a small portion of the bandwidth, sufficient information on the FRMs inside the band-of-use may not be obtained. A similar polynomial-based compensation structure is presented in [29], which showcases efficient mismatch correction results assuming the mismatch parameter identification has already been done. It is briefly

mention that the required parameter identification could be done via monitoring a cost function similar to e.g. in [70], which required multiple search iterations and was only shown for the 2-channel TI-ADC case. The methods mentioned above have used a predetermined FRM model. In practice, however, analog front-end circuit mismatch behavior is application-specific and its characteristics can be different from the assumed model [70].

As can be concluded from [42, 93] *suitable online blind identification methods* are of interest that can operate in the background and provide the TI-ADC mismatch parameters in the form that can directly be used in the mismatch compensation step. For efficient mitigation of the TI-ADC FRMs, estimates must come from within the band of use because relying on a mismatch reference obtained via oversampling may not be sufficient. Also, it is desirable to have correction methods which are not restricted by specific model-based assumption of the mismatch's characteristics. For example, having a fixed second-order polynomial model [70] or assuming a simplified model such as a first-order RC circuit BW mismatch in the S/H [66] might not be sufficient. This is because the analog front-end mismatch characteristics may differ from the assumed model [70]. Methods have been proposed to handle the mismatch correction process without these restriction assuming, however, that the mismatch parameters are known [29, 31, 32, 39, 72, 95]. Alternatively, an additional ADC can be used as reference for detecting the sample value deviation in estimating the frequency response mismatches e.g. [63]. The simulation shown required 2^{23} samples to converge and exhibits a trade-off between the reference ADC's resolution and the achievable improvement. In 2014, 2 proposals were made towards non-blind FRM identification in 4-channel TI-ADC [42, 84]. In [84], by feeding a known signal into the ADC, the mismatch estimation and compensation is done using variable digital filter which builds upon the Gauss-Seidl iteration method. Similarly, [42] uses an internal reference signal consisting of a band-limited pseudo-random noise sequence. Least-mean-square algorithm based adaptive filters are then designed to minimize the error between the known ideal reference and the collected TI-ADC's output. The method of [84] partially interrupts the TI-ADC's operation to inject a calibration signal. Therefore, the missing samples of the operational signal must be recovered via additional signal processing operations, which leads to additional complexity and higher computational resources consumption [56, 84].

Lately, a new breed of algorithms have been emerging for tackling TI-ADC mismatch identification and compensation process, where the TI-ADC's mismatch identification problem is converted into an I/Q mismatch identification problem. First known examples of these types of algorithms, which map the 2-channel TI-ADC problem into an I/Q mismatch problem are [76],[P8]. This mapping allows using powerful complex signal processing based techniques that measure the mirror frequency correlation. The spectrum

of a 2-channel TI-ADC with its mismatch spurs can be directly converted into an I/Q downconversion spectrum with mirror frequency interference spurs, i.e., the two are connected via a lowpass-bandpass transformation. This relationship was presented and studied in [30] and [P5] independently. [30] also examined performing I/Q mismatch correction after converting it into a 2-channel TI-ADC mismatch problem. It will be highlighted in the framework of this thesis that correcting the TI-ADC mismatches in cases beyond the classical 2-channel TI-ADC requires novel methods which goes beyond the lowpass-bandpass transformation as shown in [30] and [P5]. It will also be shown that a Hilbert transformation, e.g., as utilized in [30] and [P5], can be bypassed when converting the TI-ADC mismatch identification problem into an I/Q mismatch problem.

It is also interesting to note that very recently other types of methods have also been presented for the 2-channel and 4-channel TI-ADC FRM correction which also utilize complex signal processing correlation techniques [9, 10]. Complex valued signals are generated out of the real-valued TI-ADC outputs such that the desired signals' spectral component are aligned with the interleaving spur components. Once the alignment is done, the correlation is measured between the desired signal and the interleaving spur components in the process of reconstructing and removing the TI-ADC mismatch spur components. Calculating the correlation between the desired signal and spur component after the frequency component alignment is the main difference of these methods as opposed to the mirror frequency correlation based techniques used in the I/Q mismatch corrrection methods. As stated in [9, 10], it is required that the desired signal and interleaving spur components do not overlap for the proposed method to work.

CHAPTER 3

Modeling of Frequency Response Mismatches in TI-ADCs

This chapter touches upon the modeling of the FRMs in TI-ADCs and in I/Q TI-ADCs. The modeling of the FRMs in real valued TI-ADCs is carried out using a complex valued CT analog signal $x_c(t)$, whose FT $X_c(j\Omega)$ is depicted in Fig. 3.1 a). $x_c(t)$ is the analytical version of the actual real-valued TI-ADC input signal $x(t)$, i.e., $x(t) = \mathrm{Re}\{x_c(t)\}$ and $x_c(t) = x(t) + jh_{HT}(t) * x(t)$. Therefore, the spectral content of $X(j\Omega)$ contains also the mirror frequency components as shown in Fig. 3.1 b) as opposed to $X_c(j\Omega)$. The TI-ADC's FRM modeling is done using the complex valued signal $x_c(t)$ and is then mapped to the real-valued signal $x(t)$. This works in tandem with the FRM identification process in chapter 4 which generates a complex valued signal from the real valued TI-ADC output and uses complex signal processing techniques for blindly identifying the FRM. The modeling of the I/Q TI-ADCs is, in turn, carried out using $v(t)$, which is simply $x_c(t)$ frequency shifted by $-\Omega_s/4$. This naturally corresponds to the case where parallel TI-ADCs are used to sample the analog I and Q components which are already generated through analog I/Q downconversion and filtering. Offset mismatches are neglected in the analysis as they can be assumed to be independent of the input signal and since methods already exist for their compensation [29, 50].

The modeling reported in this chapter builds primarily on the thesis publications [P1], [P2] and[P4]. In the literature, real valued FRM modeling related to TI-ADCs has also been reported, e.g., in [65] and also in [97], which utilizes non-linear hybrid filter banks in the TI-ADC's non-idealities. In this chapter, complex valued FRM modeling of

the TI-ADCs is done which facilitates the study of the nature of the FRM spurs in the TI-ADCs and also in performing the identification of the FRM spur parameters using complex valued mirror frequency interference techniques.

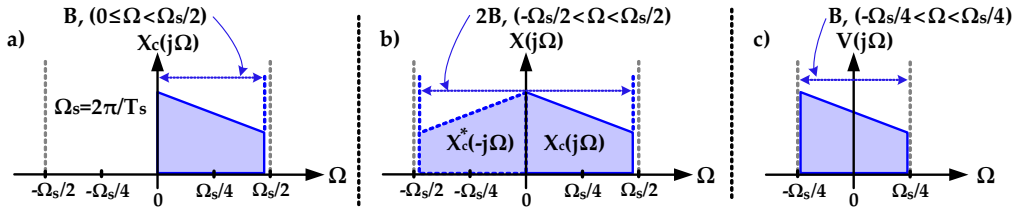

Figure 3.1: Basic illustration of complex-valued analytic (a) and ordinary real-valued (b) signal spectra. In (c), the corresponding baseband I/Q signal spectrum is shown.

3.1 FRM Modeling of 2 TI-ADC

A first Nyquist IF-sampling case is considered, with $x_c(t)$ having its spectral content located between $0 \leq \Omega < \Omega_s/2$, as shown in Fig. 3.2 a). When $x_c(t)$ is sampled using a complex sampling ADC, which samples at intervals of $2T_s$, the spectrum of $X_c(j\Omega)$ is periodically repeating at integer multiples of $\Omega_s/2$, as is illustrated for $X_{1c}(j\Omega)$ in Fig. 3.2 b). When $\mathrm{Re}\{x_{1c}(t)\}$ is taken, i.e., to reflect a real sampling ADC, this introduces the mirror frequency components and can be viewed as the unfolding of the spectrum $X_{1c}(j\Omega)$, as shown in Fig. 3.2 c), causing aliasing of the spectral content.

In order to avoid aliasing, the spacing between the periodically repeating spectral replicas in $X_{1c}(j\Omega)$ can be doubled by interleaving 2 ADCs. The time interleaving of these 2 ADCs is expressed as

$$x_{2c}(t) = g_0(t) * x_c(t) \sum_{k=-\infty}^{\infty} \delta(t - k2T_s) + g_1(t) * x_c(t) \sum_{k=-\infty}^{\infty} \delta(t - k2T_s - T_s), \quad (3.1)$$

with both ADCs sampling the signal $x_c(t)$ at the same interval $2T_s$ but with a relative time shift T_s. The ADC impulse responses are denoted using $g_m(t)$, where $m = 0, 1$. For modeling convenience, $G_m(j\Omega)$ is defined as having a non-zero frequency response only in the region where the spectral content of $x_c(t)$ is located, i.e., for the first Nyquist sampling case $G_m(j\Omega)$ is zero outside $0 \leq \Omega < \Omega_s/2$. When the output of the two ADCs are multiplexed, i.e., interleaved, an effective sample rate of T_s is achieved. The

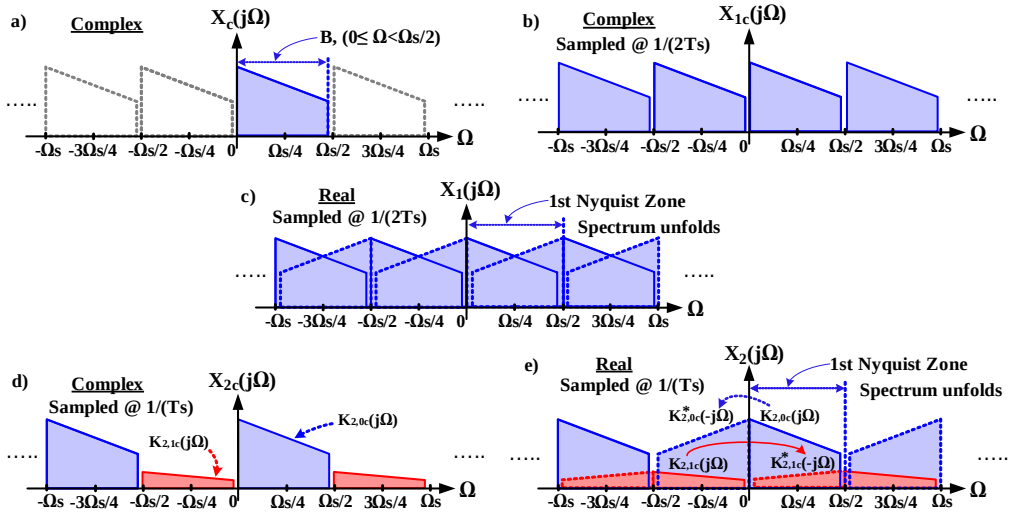

Figure 3.2: Various spectra in the two-channel TI-ADC modeling. Subfigure e) depicts the resulting spectrum of a real TI-ADC with frequency response mismatch and its FRM spurs.

frequency domain equivalent of (3.1) can be easily shown to read

$$X_{2c}(j\Omega) = \frac{1}{2T_s}\Bigg(\sum_{k=-\infty}^{\infty} G_0(j[\Omega - k\Omega_s/2])X_c(j[\Omega - k\Omega_s/2]) \\ +G_1(j[\Omega - k\Omega_s/2])X_c(j[\Omega - k\Omega_s/2])\exp(-j[\Omega_s/2]kT_s)\Bigg). \tag{3.2}$$

The effect of interleaving the time-domain signals can be studied in the frequency domain using (3.2). By simplifying the term $\exp(-j[\Omega_s/2]kT_s)$ into $(-1)^k$ it can be seen that, for values of k mod $2 = 0$, the periodically repeating spectral replicas of both ADCs sum up coherently. On the other hand, for values of k mod $2 = 1$, they are subtracted from one another. In the ideal case of the 2 ADCs having identical frequency responses, i.e., when $G_0(j\Omega) = G_1(j\Omega)$ for k mod $2 = 1$, the periodic replicas then cancel out each other completely and it is this replica cancellation that increases the Nyquist BW of the ADC. However, the inevitable mismatch between $G_0(j\Omega)$ and $G_1(j\Omega)$ in practice leads to incomplete replica cancellation as is depicted in Fig. 3.2 d). To reflect this remaining spectral residue resulting from the incomplete spectral cancellation, (3.2) can now be re-expressed as

$$X_{2c}(j\Omega) = K_{2,0c}(j\Omega) + K_{2,1c}(j\Omega) \tag{3.3}$$

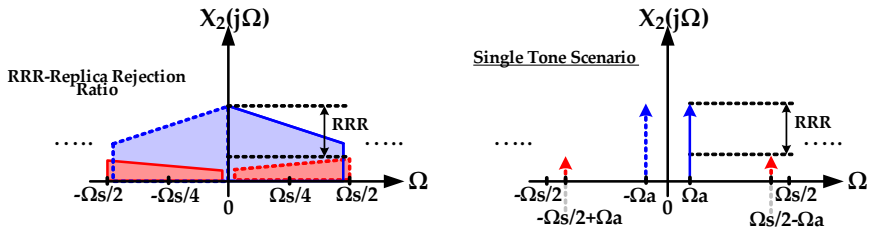

Figure 3.3: Illustration of finite RRR of real-valued two-channel TI-ADC spectrum.

with

$$K_{2,0c}(j\Omega) = \frac{1}{T_s}\sum_{k=-\infty}^{\infty} H_{2,0}(j[\Omega - k\Omega_s])X_c(j[\Omega - k\Omega_s]), \tag{3.4}$$

$$K_{2,1c}(j\Omega) = \frac{1}{T_s}\sum_{k=-\infty}^{\infty} H_{2,1}(j[\Omega_1^{[2]} - k\Omega_s])X_c(j[\Omega_1^{[2]} - k\Omega_s]), \tag{3.5}$$

$$H_{2,0}(j\Omega) = [G_0(j\Omega) + G_1(j\Omega)]/2, \tag{3.6}$$

$$H_{2,1}(j\Omega) = [G_0(j\Omega) - G_1(j\Omega)]/2. \tag{3.7}$$

The mapping of the modeling to the actual real 2 TI-ADC case is obtained by simply taking $\mathrm{Re}\{x_{2c}(t)\}$ which results in $x_2(t)$ with the corresponding frequency domain expression of the form

$$X_2(j\Omega) = \frac{\left[K_{2,0c}(j\Omega) + K^*_{2,0c}(-j\Omega)\right]}{2} + \frac{\left[K_{2,1c}(j\Omega) + K^*_{2,1c}(-j\Omega)\right]}{2}. \tag{3.8}$$

This is depicted in Fig. 3.2 e), where also the replica or spurious component structure is shown. This will be explored in more detail in subsection 3.1.1.

3.1.1 Quantifying Replica Rejection Ratio in 2 TI-ADC

The TI-ADC's FRM causes incomplete replica cancellation and the resulting spurs limit TI-ADC's SFDR. These FRM spurs can be quantified using the replica rejection ratio (RRR). The RRR, stemming directly from (3.4) and (3.5), can be expressed as

$$RRR(\Omega) = 20\log_{10}\frac{|H_{2,0}(j\Omega))|}{|H_{2,1}(j\Omega))|} \quad [dB]. \tag{3.9}$$

The illustration given in Fig. 3.3 includes also an example of a single CW tone at Ω_a. The deviations of the ADC's frequency response from the nominal values can be divided into the frequency-dependent gain response deviation, $A_\varepsilon(\Omega)$, and the frequency-dependent phase response deviation, $\varphi_\varepsilon(\Omega)$. The complex branch frequency response can first be

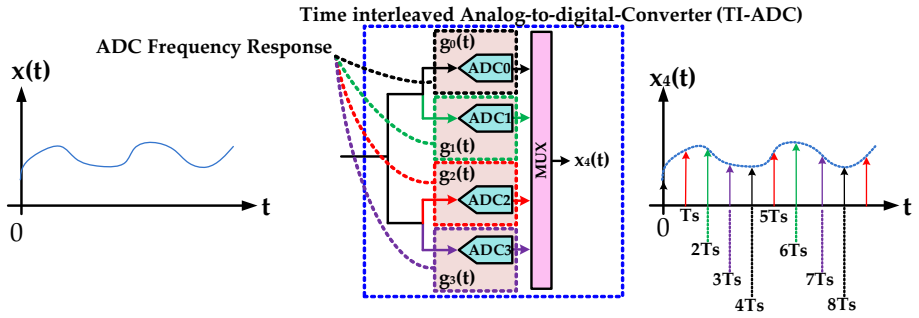

Figure 3.4: A conceptual 4 TI-ADC structure with different branch responses.

rewritten in the polar form as

$$G_m(j\Omega) = (1 + A_{\varepsilon,m}(\Omega))\exp(j\varphi_{\varepsilon,m}(\Omega)). \tag{3.10}$$

with $m = 0, 1$. By combining (3.10) with (3.6) and (3.7), the RRR expression can be approximated as

$$RRR_{2,1}(\Omega) \approx -10\log_{10}\left(\left(\frac{\Delta A_\varepsilon(\Omega)}{2}\right)^2 + \left(\frac{\Delta\varphi_\varepsilon(\Omega)}{2}\right)^2\right) \quad [dB], \tag{3.11}$$

with $\Delta A_\varepsilon(\Omega) = A_{\varepsilon,0}(\Omega) - A_{\varepsilon,1}(\Omega)$ and $\Delta\varphi_\varepsilon(\Omega) = \varphi_{\varepsilon,0}(\Omega) - \varphi_{\varepsilon,1}(\Omega)$. For 1% gain mismatch and 1 ° phase mismatch between the two branches in a 2 TI-ADC, the resulting RRR can be shown to be $\sim$ 40 dB using (3.10). To achieve a RRR in the order of $\sim$ 80 dB, a 0.01% gain and 0.01 ° phase matching is already required [87]. Such level of ADC frequency response matching is extremely challenging to achieve via careful analog matching alone.

3.2 FRM Modeling of 4 TI-ADC

The conceptual structure of a real-sampling 4-channel TI-ADC is shown in Fig. 3.4, depicting its operating principle and different frequency responses of the parallel ADCs. In the modeling of FRMs in 4 TI-ADC the analytical signal $x_c(t)$, with an angular BW B and non-zero spectral content only within $0 \leq \Omega < \Omega_s/2$ as shown in Fig. 3.5 a), is considered. In the 4-channel TI-ADC, 4 parallel ADCs are utilized to achieve the desired aggregate sample rate of $1/T_s$, where each ADC samples at rate $1/(4T_s)$ but with different time-shifts. When $x_c(t)$ is sampled using a single ADC with rate $1/(4T_s)$, this results in the spectrum of $X_c(j\Omega)$, periodically repeating at integer multiples of $(\Omega_s/4)$ as illustrated for $X_{1c}(j\Omega)$ in Fig. 3.5 b). It is seen in Fig. 3.5 b), that each individual

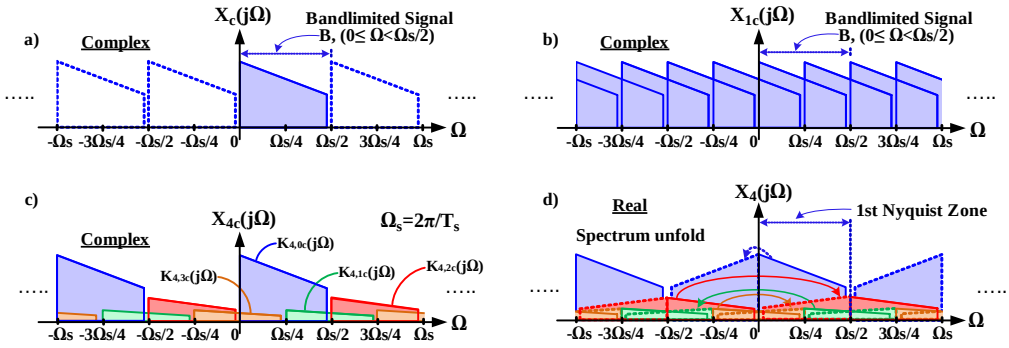

Figure 3.5: Various spectra in the 4 TI-ADC modeling. Subfigure d) shows the resulting spectrum of a real 4 TI-ADC with the response mismatch spurs.

ADC undergoes aliasing due to insufficient sampling rate. Only after interleaving the 4 TI-ADCs does the insufficient spacing between the periodically repeating spectral replicas in $X_{1c}(j\Omega)$ increase four fold. To see this, the interleaved time-domain signal is first expressed as

$$x_{4c}(t) = \sum_{m=0}^{3} \left(g_m(t) * x_c(t) \sum_{k=-\infty}^{\infty} \delta(t - k4T_s - mT_s) \right). \tag{3.12}$$

In general, each ADC samples the signal at the same intervals of $4T_s$ however with relative time shifts mT_s, $m = 0, 1, 2, 3$. A different frequency response is present in each ADC branch as denoted here with the impulse responses $g_m(t)$, or the corresponding frequency responses $G_m(j\Omega)$. When all ADC outputs are multiplexed together a four times higher output rate is produced, i.e., interleaving the output samples gives an effective sampling interval of T_s as shown in (3.12).

The frequency domain equivalent of (3.12) can then be expressed as

$$\begin{aligned} X_{4c}(j\Omega) &= \frac{1}{4T_s} \sum_{m=0}^{3} \left(\sum_{k=-\infty}^{\infty} (G_m(j[\Omega - k\Omega_s/4]) X_c(j[\Omega - k\Omega_s/4]) \exp\left[-jk\frac{2\pi}{4}m \right] \right) \\ &= \frac{1}{T_s} \sum_{k=-\infty}^{\infty} \left(\sum_{m=0}^{3} \frac{X_{c,gm}(j[\Omega - k\Omega_s/4])([-j]^m)^k}{4} \right), \end{aligned} \tag{3.13}$$

with

$$X_{c,gm}(j\Omega) = G_m(j\Omega) X_c(j\Omega). \tag{3.14}$$

The term $\exp\left[-jk\frac{2\pi}{4}m \right]$ can be simplified into $([-j]^m)^k$ as in (3.13) and shares close similarity to discrete Fourier transform (DFT). The term $([-j]^m)^k$ leads to a complex phasor summation of the spectral replicas and it is of particular interest as it plays the

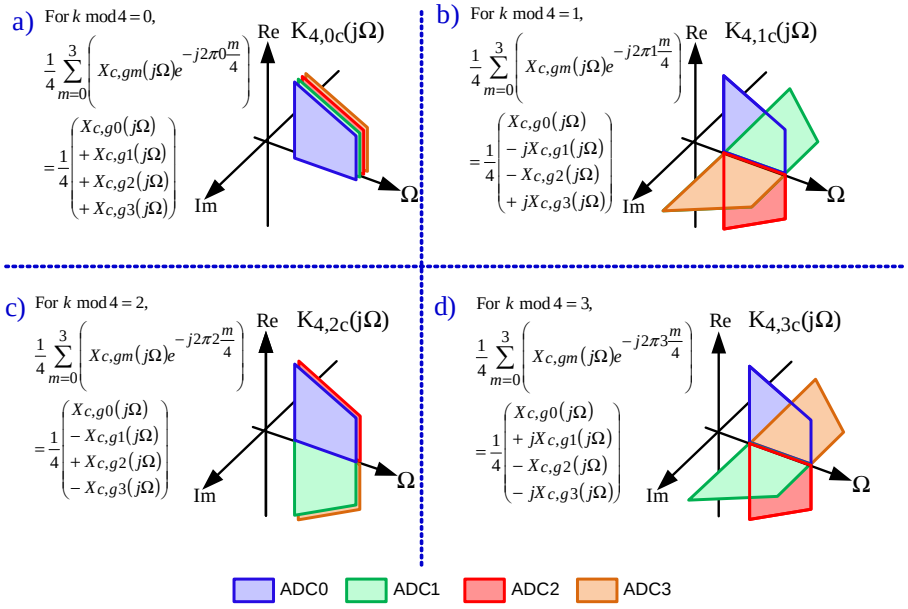

Figure 3.6: Cyclic summation and cancellation of periodically repeating replicas due to the complex phasor term in (3.15).

pivotal role in eliminating the aliasing replicas upon interleaving the constituent ADC signals. (3.13) can be expanded next into

$$X_{4c}(j\Omega) = \frac{1}{T_s}\sum_{k=-\infty}^{\infty}\frac{1}{4}\Big(X_{c,g0}(j[\Omega - k\Omega_s/4])(1)^k + X_{c,g1}(j[\Omega - k\Omega_s/4])(-j)^k + X_{c,g2}(j[\Omega - k\Omega_s/4])(-1)^k + X_{c,g3}(j[\Omega - k\Omega_s/4])(j)^k\Big), \tag{3.15}$$

Based on (3.15), it can be seen that there are 4 distinct replica rotation and summation patterns that lead to 4 distinct replica components, all of which repeat at intervals of 4 w.r.t. the summation index k. For values of $k \bmod 4 = 0$, these rotating periodic replicas add up. For values of $k \bmod 4 = 1, 2, 3$ the rotating replicas intend to cancel each other out in the configuration depicted in Fig. 3.6. By re-expressing (3.15) as

$$X_{4c}(j\Omega) = \sum_{m=0}^{3} K_{4,mc}(j\Omega). \tag{3.16}$$

with

$$\begin{aligned} K_{4,mc}(j\Omega) &= \frac{1}{T_s}\sum_{k=-\infty}^{\infty}\left[H_{4,m}(j\left[\Omega_m^{[4]}-k\Omega_s\right])X_c(j\left[\Omega_m^{[4]}-k\Omega_s\right])\right], \\ H_{4,m}(j\Omega) &= \frac{1}{4}\sum_{n=0}^{3}\left[G_n(j\Omega)([-j]^m)^n\right], \end{aligned} \tag{3.17}$$

the periodically repeating and rotating replicas are separated into $K_{4,mc}(j\Omega)$, for $m = 0, 1, 2, 3$, which represent the sum spectrum component for each value of $k \bmod 4 = m$. It is shown in Fig. 3.6 that for values of $k \bmod 4 = 0$, the spectral replicas of all ADCs are coherently summing up. For values of $k \bmod 4 = 1, 2, 3$, the spectral replicas are positioned in a configuration to cancel out one another. In the special case of identical constituent ADC frequency responses, i.e., $G_0(j\Omega) = G_1(j\Omega) = G_2(j\Omega) = G_3(j\Omega)$, the periodic replicas therefore completely cancel out each other. However, the inevitable differences between the ADCs' responses that occur in practice lead to incomplete replica cancellation as depicted in Fig. 3.5 c). This provides a spectral illustration of the most fundamental structure and nature of the mismatch spurs.

Then, the actual real-valued 4 TI-ADC signal $x_4(t)$ can be characterized by taking $\mathrm{Re}\{x_{4c}(t)\}$, which introduces the mirror-frequency contents in all spectral components in $x_{4c}(t)$. The mirror-frequency components of $K_{4,mc}(j\Omega)$ are in the form of $K_{4,mc}^*(-j\Omega)$, whose creation can be viewed as the unfolding of the spectrum $X_{4c}(j\Omega)$ as illustrated in Fig. 3.5 d). Next, (3.16) can be re-expressed to reflect the unfolding of the spectrum as

$$\begin{aligned} X_4(j\Omega) &= \frac{1}{2}[X_{4c}(j\Omega) + X_{4c}^*(-j\Omega)] = \sum_{m=0}^{3} K_{4,m}(j\Omega)) \\ &= \sum_{m=0}^{3} \underbrace{\left[K_{4,mc}(j\Omega) + K_{4,mc}^*(-j\Omega)\right]/2}_{K_m(j\Omega)}. \end{aligned} \tag{3.18}$$

The spectral content of $X_4(j\Omega)$ illustrated in Fig. 3.5 d) is decomposed and depicted separately in Fig. 3.6, where the spectral components $K_{4,m}(j\Omega)$ are depicted separately for better visualization and insight. If no FRM between the constituent ADC was present, only the fundamental component $K_{4,0}(j\Omega)$ would be present. The spur component $K_{4,2}(j\Omega)$ has in fact the same structure as in the 2-channel TI-ADC case [P1],[P2]. The other 2 spur components, $K_{4,1}(j\Omega)$ and $K_{4,3}(j\Omega)$, are additional spurious components present in the 4-channel TI-ADC case. It can also be seen in Fig. 3.6 b) and Fig. 3.6 d) that if no mismatches existed between $ADC0$ & $ADC2$ and between $ADC1$ & $ADC3$, then the spur components $K_{4,1}(j\Omega)$ and $K_{4,3}(j\Omega)$ are not present and it would correspond to the 2 TI-ADC case of subsection 3.1. It can also be inferred from Fig. 3.6

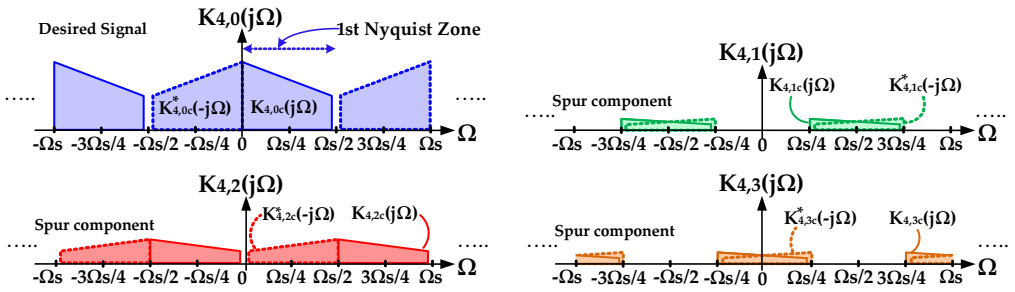

Figure 3.7: Decomposed spectral components of a real-valued 4-channel TI-ADC output spectrum.

c), that the spur $K_{4,2}(j\Omega)$ exists when either $ADC0$ or $ADC2$ has a mismatch with $ADC1$ or $ADC3$.

3.2.1 Quantifying Replica Rejection Ratio in 4 TI-ADC

Similar to subsection 3.1.1, the RRR in the 4 TI-ADC case refers to the ratio between the fundamental component $K_{4,0}(j\Omega)$ and the FRM spur components $K_{4,1}(j\Omega)$, $K_{4,2}(j\Omega)$, $K_{4,3}(j\Omega)$. Stemming from (3.17), the RRR which quantifies the TI-ADC's SFDR from a particular spur point of view can then be expressed as the logarithmic ratio between $H_{4,0}(j\Omega)$ and a specific $H_{4,m}(j\Omega)$, written as

$$RRR_{4,m}(\Omega) = 20\log_{10}\frac{|H_{4,0}(j\Omega))|}{|H_{4,m}(j\Omega))|} \quad [dB], \tag{3.19}$$

for $m = 1, 2, 3$.

3.3 FRM Modeling in I/Q Downconversion TI-ADCs

3.3.1 I/Q Downconversion Stage Mismatch Modeling

In the upcoming downconversion and sampling modeling, an arbitrary RF signal $v_{RF}(t)$ with an angular bandwidth B_Ω is used, as depicted in Fig. 3.8 a) and can be written as

$$v_{RF}(t) = 2\mathrm{Re}\{v(t)\exp\{j\Omega_{LO}t\}\}, \tag{3.20}$$

with $\Omega_{LO} = 2\pi F_{LO}$, F_{LO} being carrier center frequency. During the analog processing in the I and Q branches, $v_{RF}(t)$ is subject to different frequency responses. The RF impulse response already, e.g., in the I branch is denoted by $g_{I,RF}(t)$, and the corresponding baseband response is labeled by $g_{I,BB}(t)$ as seen in Fig. 3.8. The I branch downconverted

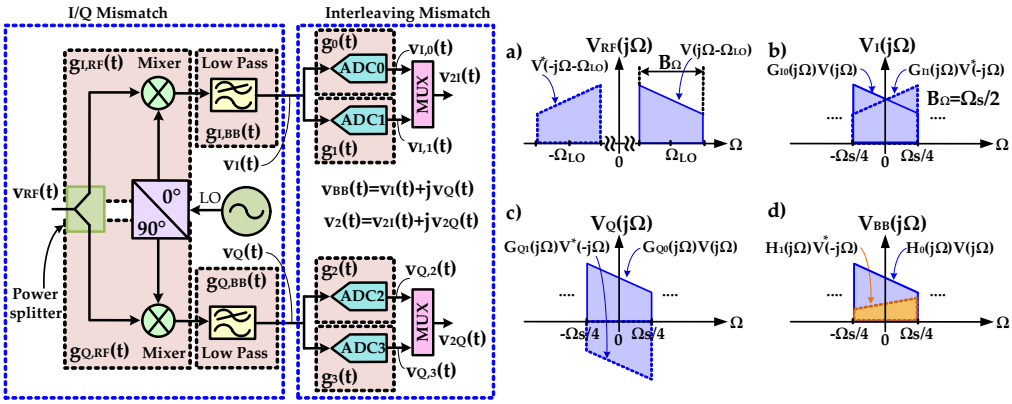

Figure 3.8: Analog Homodyne downversion stage employing 2 TI-ADCs in both the I and Q branches with spectral illustrations, before the TI-ADC sampling, of a) Real-valued signal $v_{RF}(t)$ at RF, b) Real-valued symmetrical signal $v_I(t)$ at baseband (BB), c) Real-valued anti-symmetrical signal $v_Q(t)$ at BB and d) Complex-valued signal $v_{BB}(t)$ at BB with I/Q mismatch.

and filtered signal $v_I(t)$, whose FT is depicted in Fig. 3.8 b), is expressed as

$$v_I(t) = \frac{[g_{I0}(t) * v(t) + g_{I1}(t) * v^*(t)]}{2}, \tag{3.21}$$

while the corresponding Q branch signal $v_Q(t)$, whose FT is depicted in Fig. 3.8 c), is expressed as

$$v_Q(t) = \frac{[g_{Q0}(t) * v(t) - g_{Q1}(t) * v^*(t)]}{2j}. \tag{3.22}$$

In the equations above, the impulse responses $g_{I0}(t)$, $g_{I1}(t)$, $g_{Q0}(t)$ and $g_{Q1}(t)$ denote the effective joint impulse responses and incorporate both the influences of RF and BB mismatches and their corresponding frequency responses can be expressed as

$$G_{I0}(j\Omega) = G_{I,BB}(j\Omega)G_{I,RF}(j[\Omega + \Omega_{LO}]), \tag{3.23}$$

$$G_{I1}(j\Omega) = G_{I,BB}(j\Omega)G^*_{I,RF}(-j[\Omega - \Omega_{LO}]), \tag{3.24}$$

$$G_{Q0}(j\Omega) = G_{Q,BB}(j\Omega)G_{Q,RF}(j[\Omega + \Omega_{LO}]), \tag{3.25}$$

$$G_{Q1}(j\Omega) = G_{Q,BB}(j\Omega)G^*_{Q,RF}(-j[\Omega - \Omega_{LO}]). \tag{3.26}$$

The downconverted signal $v_{BB}(t)$, shaped by the RF and BB frequency response mismatches, is expressed as

$$v_{BB}(t) = v_I(t) + jv_Q(t) = h_0(t) * v(t) + h_1(t) * v^*(t), \tag{3.27}$$

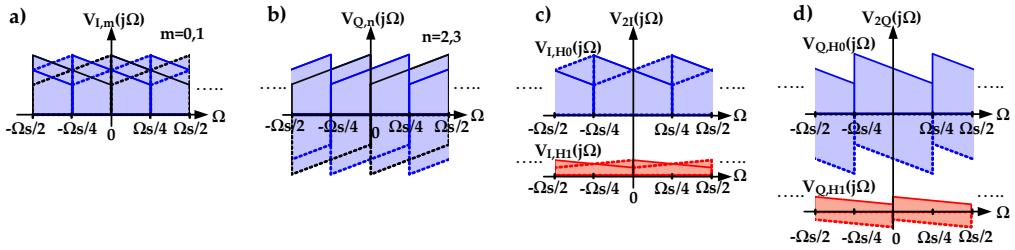

Figure 3.9: Spectral illustrations of A) Real-valued I branch signal $v_I(t)$ sampled at $1/(2T_s)$, B) Real-valued Q branch signal $v_Q(t)$ sampled at $1/(2T_s)$, C) Real-valued I branch interleaved signal $v_{2I}(t)$ and D) Real-valued Q branch interleaved signal $v_{2Q}(t)$.

and its FT $V_{BB}(t)$ can be expressed as

$$V_{BB}(j\Omega) = H_0(j\Omega)V(j\Omega) + H_1(j\Omega)V^*(-j\Omega), \tag{3.28}$$

with $H_0(j\Omega)V(j\Omega)$ being the linearly distorted version of $V(j\Omega)$, $H_1(j\Omega)V^*(-j\Omega)$ corresponding to the filtered mirror-frequency component and the responses $H_0(j\Omega)$ and $H_1(j\Omega)$ being of the form

$$H_0(j\Omega) = [G_{I0}(j\Omega) + G_{Q0}(j\Omega)]/2, \tag{3.29}$$

$$H_1(j\Omega) = [G_{I1}(j\Omega) - G_{Q1}(j\Omega)]/2. \tag{3.30}$$

The mirror-frequency component $V^*(-j\Omega)$ is only partially suppressed because of the FRM, i.e., $G_{I1}(j\Omega) \neq G_{Q1}(j\Omega)$, and can result in severely reduced SFDR in $v_{BB}(t)$, as illustrated in Fig. 3.8 d). The signal $v_{BB}(t)$ can be described using a widely linear signal model as shown in (3.28), which consists of filtering the ideal complex signal $v(t)$ and its conjugate $v^*(t)$ [6]. Traditionally, the ADCs in the I and Q branches of Homodyne receiver must have sample rate of $1/(2T_s)$, when sampling a signal with a BW of $\Omega_s/2$, to avoid aliasing of its periodically repeating spectrum. However, if the single ADC cannot achieve this sample rate, the TI-ADCs can be used in the I and Q branches to increase the sample rate. This, however, leads to further FRM-induced spur components in the complex spectrum. The modeling of these additional spurious components will be done in subsection 3.3.2 next.

3.3.2 Time Interleaved ADC Stage Mismatch Modeling

In the following modeling, it is assumed that the required I/Q ADC sample rate is $1/(2T_s)$ in the I and Q branches. A sampling rate of $1/(2T_s)$ is achieved using 2 TI-ADC, with each constituent ADC having a sample rate of $1/(4T_s)$, in the I and Q branches

respectively. As shown in Fig. 3.8, the I branch utilizes *ADC* 0 and *ADC* 1 while the Q branch utilizes *ADC* 2 and *ADC* 3. In the I-branch, a low sample rate of $1/(4T_s)$ per individual ADC leads to the periodically repeating spectrum of $v_I(t)$ with a BW of $\Omega_s/2$ incorporated in $v_{I,0}(t)$ and $v_{I,1}(t)$ to repeat at intervals of $\Omega_s/4$ and causes aliasing, as shown in Fig. 3.9 a). Similarly, aliasing also occurs in the Q branch, as shown in Fig. 3.9 b). In accordance with the 2 TI-ADC sampling architecture, e.g., in the I branch, *ADC* 1 samples $v_I(t)$ with a time shift $2T_s$ relative to *ADC* 0 and its time interleaved signal $v_{2I}(t)$ can be expressed as

$$v_{2I}(t) = \underbrace{g_0(t) * v_I(t)}_{v_{I,0}(t)} \sum_{k=-\infty}^{\infty} \delta(t - k4T_s) + \underbrace{g_1(t) * v_I(t)}_{v_{I,1}(t)} \sum_{k=-\infty}^{\infty} \delta(t - k4T_s - 2T_s), \tag{3.31}$$

with $g_0(t)$ denoting the impulse response of *ADC* 0 and $g_1(t)$ denoting the impulse response of *ADC* 1. The frequency domain equivalent of (3.31) can be expressed as

$$V_{2I}(j\Omega) = \frac{1}{4T_s} \sum_{k=-\infty}^{\infty} V_{I,0}([j(\Omega - k\Omega_s/4)]) + V_{I,1}([j(\Omega - k\Omega_s/4)])\exp(-j[\Omega_s/4]2kT_s). \tag{3.32}$$

with $V_{I,0}(j\Omega) = G_0(j\Omega)V_I(j\Omega)$ and $V_{I,1}(j\Omega) = G_1(j\Omega)V_I(j\Omega)$. The relative time shift $2T_s$ in *ADC* 1's sampling intervals creates the term $\exp(-j[\Omega_s/4]2kT_s)$ which simplifies into $(-1)^k$. Therefore, for values of $k \bmod 2 = 0$, the periodic spectral replicas of *ADC* 0 and *ADC* 1 add up coherently. For values of $k \bmod 2 = 1$, however, the spectral replica are 180° out of phase from one another. Therefore, in the ideal case where $G_0(j\Omega) = G_1(j\Omega)$, for $k \bmod 2 = 1$ the periodic replicas then cancel out each other completely. However, in practice, the inevitable dissimilarity between $G_0(j\Omega)$ and $G_1(j\Omega)$ leads to an incomplete replica cancellation. This can be quantified by rewriting (3.32) as

$$V_{2I}(j\Omega) = V_{I,H0}(j\Omega) + V_{I,H1}(j\Omega), \tag{3.33}$$

with $V_{I,H0}(j\Omega)$ being the resulting spectrum for $k \bmod 2 = 0$ and it can be described by

$$V_{I,H0}(j\Omega) = \frac{1}{2T_s} \sum_{k=-\infty}^{\infty} H_{I0}(j[\Omega - k\Omega_s/2])V_I(j[\Omega - k\Omega_s/2]), \tag{3.34}$$

and $V_{I,H1}(j\Omega)$ is then the spectrum for $k \bmod 2 = 1$ as expressed in

$$V_{I,H1}(j\Omega) = \frac{1}{2T_s} \sum_{k=-\infty}^{\infty} H_{I1}\Big(j\Big[\Omega_1^{[4]} - k\Omega_s/2\Big]\Big)V_I\Big(j\Big[\Omega_1^{[4]} - k\Omega_s/2\Big]\Big), \tag{3.35}$$

with

$$H_{I0}(j\Omega) = [G_0(j\Omega) + G_1(j\Omega)]/2, \tag{3.36}$$

$$H_{I1}(j\Omega) = [G_0(j\Omega) - G_1(j\Omega)]/2. \tag{3.37}$$

Both the individual spectra of $V_{I,H0}(j\Omega)$ and $V_{I,H1}(j\Omega)$ contained in $V_{2I}(j\Omega)$ are shown in Fig. 3.9 c). The Q branch signal $v_{2Q}(t)$ can be expressed in a similar way as $v_{2I}(j\Omega)$ in (3.31). The FT of $v_{2Q}(t)$, $V_{2Q}(j\Omega)$, can be expressed similar to (3.32) using $V_{Q,2}(j\Omega) = V_Q(j\Omega)G_2(j\Omega)$ and $V_{Q,3}(j\Omega) = V_Q(j\Omega)G_3(j\Omega)$. $V_{2Q}(j\Omega)$, can also be expressed in a similar fashion to (3.33) as

$$V_{2Q}(j\Omega) = V_{Q,H0}(j\Omega) + V_{Q,H1}(j\Omega), \tag{3.38}$$

where $V_{Q,H0}(j\Omega)$ is the resulting spectrum from $k \bmod 2 = 0$ as in

$$V_{Q,H0}(j\Omega) = \frac{1}{2T_s} \sum_{k=-\infty}^{\infty} H_{Q0}(j[\Omega - k\Omega_s/2])V_Q(j[\Omega - k\Omega_s/2]), \tag{3.39}$$

and $V_{Q,H1}(j\Omega)$ is the resulting spectrum from $k \bmod 2 = 1$ as given by

$$V_{Q,H1}(j\Omega) = \frac{1}{2T_s} \sum_{k=-\infty}^{\infty} H_{Q1}\Big(j\Big[\Omega_1^{[4]} - k\Omega_s/2\Big]\Big)V_Q\Big(j\Big[\Omega_1^{[4]} - k\Omega_s/2\Big]\Big), \tag{3.40}$$

with

$$H_{Q0}(j\Omega) = \frac{G_2(j\Omega) + G_3(j\Omega)}{2}, \tag{3.41}$$

$$H_{Q1}(j\Omega) = \frac{G_2(j\Omega) - G_3(j\Omega)}{2}. \tag{3.42}$$

The respective spectra of $V_{Q,H0}(j\Omega)$ and $V_{Q,H1}(j\Omega)$ contained in $V_{2Q}(j\Omega)$ are shown in Fig. 3.9 d).

3.3.3 Combined Effect of All Frequency Response Mismatches

The 2 I/Q TI-ADC output spectrum $V_2(j\Omega)$ can be expressed using $V_{2I}(j\Omega)$ and $V_{2Q}(j\Omega)$ as

$$\begin{aligned} V_2(j\Omega) &= V_{2I}(j\Omega) + jV_{2Q}(j\Omega) \\ &= V_{I,H0}(j\Omega) + V_{I,H1}(j\Omega) + j(V_{Q,H0}(j\Omega) + V_{Q,H1}(j\Omega)). \end{aligned} \tag{3.43}$$

In the I/Q downconversion without TI-ADCs, only the frequency components $V_{I,H0}(j\Omega)$ and $V_{Q,H0}(j\Omega)$ are present. If 2-channel TI-ADCs are deployed, then additional spurious components $V_{I,H1}(j\Omega)$ and $V_{Q,H1}(j\Omega)$ are introduced due to the interleaving mismatches.

Therefore (3.43) is rewritten in terms of $V(j\Omega)$, $V^*(-j\Omega)$, $V(j\Omega_1^{[4]})$ and $V^*(-j\Omega_1^{[4]})$ as

$$\begin{aligned} V_2(j\Omega) = & \underbrace{\frac{1}{2T_s}\sum_{k=-\infty}^{\infty} H_{T0}(j[\Omega - k\Omega_s/2])V(j[\Omega - k\Omega_s/2])}_{V_{2,LD}(j\Omega)} \\ & + \underbrace{\frac{1}{2T_s}\sum_{k=-\infty}^{\infty} H_{T1}\Big(j\Big[\Omega_1^{[4]} - k\Omega_s/2\Big]\Big)V\Big(j\Big[\Omega_1^{[4]} - k\Omega_s/2\Big]\Big)}_{V_{2,TI}(j\Omega)} \\ & + \underbrace{\frac{1}{2T_s}\sum_{k=-\infty}^{\infty} H_{T2}(j[\Omega - k\Omega_s/2])V^*(-j[\Omega - k\Omega_s/2])}_{V_{2,IQ}(j\Omega)} \\ & + \underbrace{\frac{1}{2T_s}\sum_{k=-\infty}^{\infty} H_{T3}\Big(j\Big[\Omega_1^{[4]} - k\Omega_s/2\Big]\Big)V^*\Big(-j\Big[\Omega_1^{[4]} - k\Omega_s/2\Big]\Big)}_{V_{2,IT}(j\Omega)}, \end{aligned} \tag{3.44}$$

with $\Omega_1^{[4]} = \Omega - \Omega_s/4$ and

$$H_{T0}(j\Omega) = [G_0(j\Omega) + G_1(j\Omega)]G_{I0}(j\Omega)/4 + [G_2(j\Omega) + G_3(j\Omega)]G_{Q0}(j\Omega)/4, \tag{3.45}$$

$$H_{T1}(j\Omega) = [G_0(j\Omega) - G_1(j\Omega)]G_{I0}(j\Omega)/4 + [G_2(j\Omega) - G_3(j\Omega)]G_{Q0}(j\Omega)/4, \tag{3.46}$$

$$H_{T2}(j\Omega) = [G_0(j\Omega) + G_1(j\Omega)]G_{I1}(j\Omega)/4 - [G_2(j\Omega) + G_3(j\Omega)]G_{Q1}(j\Omega)/4, \tag{3.47}$$

$$H_{T3}(j\Omega) = [G_0(j\Omega) - G_1(j\Omega)]G_{I1}(j\Omega)/4 - [G_2(j\Omega) - G_3(j\Omega)]G_{Q1}(j\Omega)/4. \tag{3.48}$$

The frequency response mismatches of the I and Q branch, i.e., $G_{I0}(j\Omega)$, $G_{I1}(j\Omega)$, $G_{Q0}(j\Omega)$ and $G_{Q1}(j\Omega)$, interact with the frequency response mismatches of the constituent ADCs, i.e., $G_0(j\Omega)$, $G_1(j\Omega)$, $G_2(j\Omega)$ and $G_3(j\Omega)$, and result in the frequency responses $H_{T0}(j\Omega)$, $H_{T1}(j\Omega)$, $H_{T2}(j\Omega)$ and $H_{T3}(j\Omega)$. In $H_{T0}(j\Omega)$ all the frequency responses are summed up and causes the desired component $V(j\Omega)$ to therefore undergo only linear distortion and does not lead to a degradation in the SFDR as shown in Fig. 3.10. The other combinations of the frequency response terms, i.e., $H_{T1}(j\Omega)$, $H_{T2}(j\Omega)$ and $H_{T3}(j\Omega)$ do not amount to zero due to the mismatches, although they are considerably smaller compared to $H_{T0}(j\Omega)$. This results in the filtered versions of $V^*(-j\Omega)$, $V(j\Omega_1)$ and $V^*(-j\Omega_1)$ to be present in $V_2(j\Omega)$ as depicted in Fig. 3.10 and results in a loss of the SFDR. These decomposed spurious components, illustrated separately in Fig. 3.10, reveal upon analysis an interesting observation w.r.t. the exact nature of different spurs. As shown in Fig. 3.10 b), the I/Q mismatch spur is

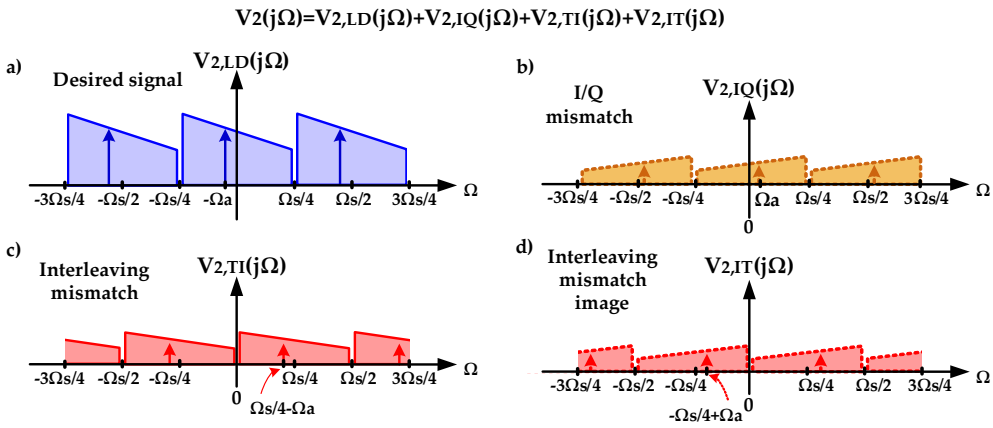

Figure 3.10: Decomposed spectral content of $V_2(j\Omega)$ due to I/Q and TI-ADC mismatches. Also shown is a single-tone example case with original complex tone at $-\Omega_a$.

mirror-symmetric around DC w.r.t. the desired signal, depicted in Fig. 3.10 a). The figure also shows an example with a single complex tone positioned at $-\Omega_a$ and the corresponding mirror component is then located at Ω_a. The interleaving mismatch spur has a frequency-shift of $+\Omega_s/4$ compared to the fundamental term and is located at $\Omega_s/4 - \Omega_a$. The interleaving mismatch image spur component is a shifted mirror image, located at $-\Omega_s/4 + \Omega_a$.

3.3.4 The Relationship of I/Q downconversion and 2 TI-ADC FRM Spurs

Observing the spectral illustrations in Fig. 3.2 e) and Fig. 3.8 d), a certain similarity between the I/Q FRM spur and the 2 TI-ADC mismatch spur can be detected. The I/Q FRM produces spur structure which is symmetric around DC to the desired frequency components in the complex signal spectrum, while the 2 TI ADC FRM produces a spur structure which is symmetric around $\Omega_s/4$ with the desired frequency components for the real signal spectrum. This similarity implies that the I/Q downconversion spectrum and the real-valued 2 TI-ADC spectrum are indeed connected by a bandpass-lowpass transformation. One method to perform this bandpass-lowpass transformation is via the HT, which can be performed as

$$X_{2c,H}(j\Omega) = X_2(j\Omega) + j[H_{HT}(j\Omega)X_2(j\Omega)]. \tag{3.49}$$

After the HT stage, the mirror spectral contents in the range $-\Omega_s/2$ to 0 are eliminated and therefore only $K_{2,0c}(j\Omega)$ alongside $K^*_{2,1c}(-j\Omega)$ remain in $X_{2c,H}(j\Omega)$, as illustrated

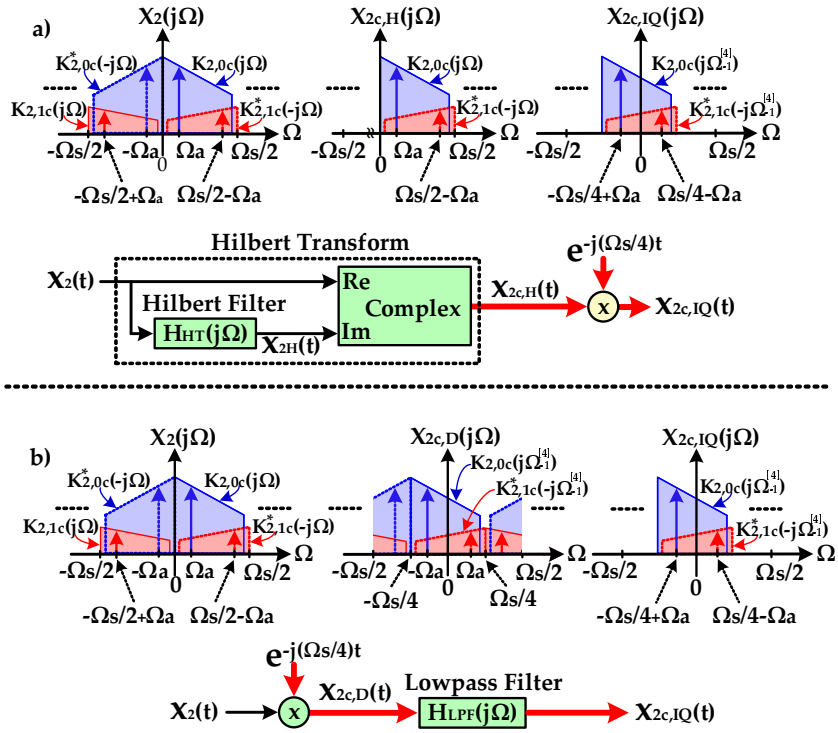

Figure 3.11: Mapping of a two-channel TI-ADC mismatch into an equivalent I/Q mismatch problem; a) Hilbert filtering and complex downconversion based processing, b) complex downconversion and lowpass filtering based processing.

in Fig. 3.11 a). Frequency shifting $X_{2c,H}(j\Omega)$ by $-\Omega_s/4$, via multiplication with $\exp(-j[\Omega_s/4]t)$, will place $K^*_{2,1c}(-j\Omega)$ at the mirror frequency location of $K_{2,0c}(j\Omega)$ producing $X_{2c,IQ}(j\Omega)$ as seen in Fig. 3.11 a), expressed more formally as

$$X_{2c,IQ}(j\Omega) = K_{2,0c}(j\Omega^{[4]}_{-1}) + K^*_{2,1c}(-j\Omega^{[4]}_{-1}). \tag{3.50}$$

The corresponding time-domain expression can be expressed in the form

$$\begin{aligned} x_{2c,IQ}(t) &= [x_2(t) + jh_{HT}(t) * x_2(t)]\exp(-j[\Omega_s/4]t) \\ &= k_{0c}(t)\exp(-j[\Omega_s/4]t) + k^*_{1c}(t)\exp(-j[\Omega_s/4]t). \end{aligned} \tag{3.51}$$

$K_{2,0c}(j\Omega^{[4]}_{-1})$ and $K^*_{2,1c}(-j\Omega^{[4]}_{-1})$ in $X_{2c,IQ}(j\Omega)$, shown in Fig. 3.11 a), have the same mirror-frequency interference relationship as the I/Q mismatched signal, i.e., as between $H_0(j\Omega)V(j\Omega)$ and $H_1(j\Omega)V^*(-j\Omega)$ in $V_{BB}(j\Omega)$, depicted in Fig. 3.8 d). The bandpass-lowpass transformation can be alternatively performed by directly deploying the I/Q

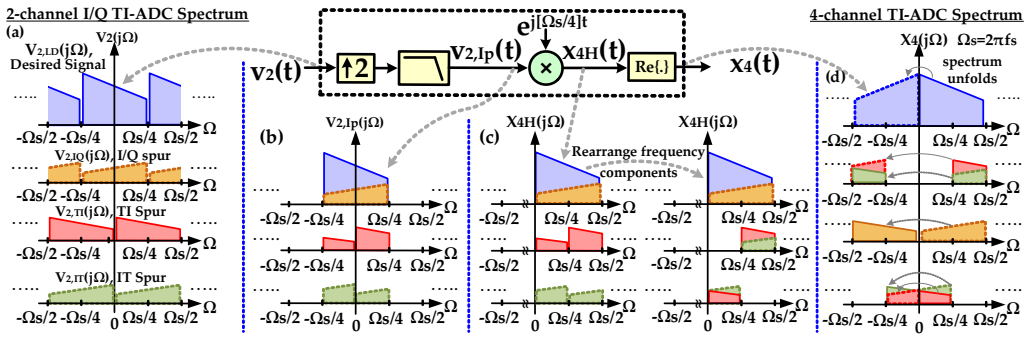

Figure 3.12: Time domain signal transformation illustration that shows the link between 2 I/Q TI-ADC conversion to 4-channel TI-ADC signal.

downconversion from $\Omega_s/4$ to DC followed by lowpass filtering using $h_{LP}(t)$. This operation, which results in the same complex-valued output as the Hilbert transform based processing, is written here as

$$x_{2c,IQ}(t) = [x_2(t)\exp(-j[\Omega_s/4]t)] * h_{LP}(t), \tag{3.52}$$

and is shown in Fig. 3.11 b). The strong connection between the two-channel TI-ADC FRM spurs and I/Q FRM spurs is formally established via the derivations above. This consequently means that the 2 TI-ADC FRM problem can be converted into an equivalent I/Q FRM problem and enables efficient blind identification of the 2 TI-ADC FRM. First known examples building on converting the TI-ADC problem into an I/Q mismatch problem are presented in [P8], [76] and the importance of this finding has also been reported and emphasized recently in [30]. The close connection between the TI-ADC and I/Q downconversion will be capitalized in the development of processing structures and algorithms for detecting and suppressing the FRM spurs in a blind manner in the context of TI-ADC with real-valued output, as will be described in more details in chapter 4.

3.4 The relationship of 2 I/Q TI-ADC and 4 TI-ADCs FRM Spurs

In this section, building upon the comprehensive modeling of the 4 TI-ADC carried out in subsection 3.2 and the 2 I/Q TI-ADC carried out in subsection 3.3, the relationship between a 4 TI-ADC and a 2 I/Q TI-ADC is examined. Both converter architectures do in fact adopt 4 ADC units in parallel but the ADCs are used in different configurations in the respective converter architectures. In the process of establishing the relationship between the 2 I/Q TI-ADC scenario and the earlier 4 TI-ADC, let the signal $v_2(t)$ first

be upsampled by a factor of 2 and then low pass filtered between $-\Omega_s/4 < \Omega < \Omega_s/4$ with $h_{LP}(t)$ to give an interpolated signal $v_{2,Ip}(t)$, as depicted in Fig. 3.12(b). In the next step, the interpolated signal $v_{2,Ip}(t)$ is frequency shifted by $\Omega_s/4$ via multiplication with $\exp(j[\Omega_s/4]t)$ to give $x_{4H}(t)$, as shown in Fig. 3.12(c). Taking the real part of the complex valued signal $x_{4H}(t)$ introduces the mirror frequency components and the spectrum unfolds, as shown in Fig. 3.12(d). The resulting signal is then labeled $x_4(t)$ due to it being the same as the 4 TI-ADC output signal with FRMs, and can be mathematically expressed as

$$x_4(t) = \mathrm{Re}\{v_{2,Ip}(t)\exp(j[\Omega_s/4]t)\}, \tag{3.53}$$

Therefore it is established that the 4 TI-ADC output signal, $x_4(t)$, and the 2 I/Q TI-ADC output signal, $v_2(t)$, do indeed share the lowpass-bandpass transformation relationship. It can be observed in Fig. 3.12(d) that the spectral components of $V_{2,TI}(j\Omega)$ and $V_{2,IT}(j\Omega)$ between $0 \leq \Omega < \Omega_s/4$ are grouped together as are also the spectral components between $\Omega_s/4 \leq \Omega < \Omega_s/2$. This facilitates examining the nature of the spectral components that unfold. In Fig. 3.12(d), it is observed that the structure of the spurs coincide with the structure of the spurs of a 4 TI-ADC depicted in Fig. 3.7. The spectral content of $V_{2,LD}(j\Omega)$ maps into $K_{4,0}(j\Omega)$ while $V_{2,IQ}(j\Omega)$ maps into $K_{4,2}(j\Omega)$, just as the lowpass-bandpass transformation of the direct downconversion receiver and the 2 TI-ADC [P2], [30]. The remaining spur components $K_{4,1}(j\Omega)$ and $K_{4,3}(j\Omega)$ both jointly map into $V_{2,TI}(j\Omega)$ and $V_{2,IT}(j\Omega)$. This lowpass-bandpass relationship does in fact open up the possibility of tackling the FRM identification problem of either one of these two alternative converter architectures using correction techniques developed for the other.

CHAPTER 4

Identification and Compensation of TI-ADCs mismatches

This chapter addresses the identification and compensation architectures of FRMs in TI-ADCs and I/Q TI-ADCs. The identification stage involves extracting the FRM spurs' parameters and the correction stage involves using the extracted parameters to reconstruct the FRM spur components. The compensation strategy involves subtracting the reconstructed FRM spurs from the TI-ADC or I/Q TI-ADC output, to recover the lost SFDR due to these mismatches. First, section 4.1 adresses the FRM's identification and compensation architectures in 2 TI-ADC. Then, section 4.2 proceeds to address the FRMs' identification and compensation architectures in 4 TI-ADC. Finally, section 4.3 addresses the FRMs' identification and compensation architecture in 2 I/Q TI-ADC. The actual blind mirror frequency based learning algorithms, common to all cases, are shortly described in section 4.4. In general, this chapter builds on the original publications [P1],[P2],[P3],[P5],[P6],[P7],[P8].

4.1 Identification and Compensation of FRM in 2 TI-ADC

The finite and insufficient replica rejection present in the 2 TI-ADC due to FRM can be improved by utilizing the error removal scheme depicted in Fig. 4.1, whose basic principle involves reconstructing an estimate of the FRM-induced spur component and then

subtracting it from the original 2 TI-ADC output. The proposed architecture involves taking a copy of $X_2(j\Omega)$ and frequency-shifting it by $\Omega_s/2$ to produce $X_{2,m}(j\Omega)$, which is now aligned with the undesired interleaving mismatch spur component in $X_2(j\Omega)$. Based on the 2 TI-ADC spur structure established in section 3.1, it is fairly evident that the spur $k_{2,1}(t)$ has mirror-symmetric nature around $\Omega_s/4$ relative to the desired signal component.

Due to the symmetry at $\Omega_s/4$ of the spur component $k_{2,1}(t)$ w.r.t. to the desired signal's spectral content $k_{2,0}(t)$, the classical highpass-lowpass transformation, i.e. utilizing frequency shifting by $\Omega_s/2$, will provide a proper basis for the cancellation of spur $k_{2,1}(t)$. The estimate of $k_{2,1}(t)$, denoted by $\tilde{k}_{2,1}(j\Omega)$, is constructed by convolving $x_{2,m}(t)$ with a compensation filter $w_2(t)$. The estimate $\tilde{k}_{2,1}(t)$ can then be subtracted from $x_2(t)$ to produce $y_2(t)$ with the component $k_{2,1}(t)$ being considerably reduced. This type of cancellation principle, due to the presence of small fundamental component in the cancellation signal, does cause some level of residual linear filtering effect on the fundamental signal component. This effect is, however, safely negligibly with practical spurious levels as will also be confirmed by the actual RF measurement results shown in Section 5.

The FRM spur reconstruction process shown above requires for the FRM parameters to be accurately known and the main challenge thus lies in identifying the TI-ADC's unknown FRM. The identification of the FRM parameters is preferably to be carried out in a blind manner with sufficient accuracy, in order to obtain a sufficiently accurate reconstruction of the interleaving mismatch component $k_{2,1}(t)$ [93, 94]. It was shown in Section 3.3.4 that the 2 TI-ADC problem can be mapped into an equivalent I/Q mismatch problem via using either (3.51) or (3.52) which allows performing the 2 TI-ADC FRM identification using mirror frequency interference (MFI) based techniques which were originally developed for the I/Q mismatch problem. Such signals, referred to as mismatch identification signal (MIS), can be generated to extract the parameters of spur $k_{2,1}(t)$.

The FRM spur $K_{2,1}(j\Omega)$'s blind identification and mitigation process is briefly elaborated as follows. The correction principle of the 2 TI-ADC FRM spur component $K_{2,1}(j\Omega)$ consists of recreating accurate estimates of the spur $K_{2,1}(j\Omega)$, $\tilde{K}_{2,1}(j\Omega)$. $\tilde{K}_{2,1}(j\Omega)$ can then be subtracted from the 2 TI-ADC output $x_2(t)$ to mitigate the effect of spur $K_{2,1}(j\Omega)$. For this, sufficiently accurate identification of the spur component's frequency response, i.e., $H_{2,1}(j\Omega)$, relative to the desired signal's frequency response, i.e., $H_{2,0}(j\Omega)$, is required. This is accomplished by generating appropriate complex-valued MIS in the form of MFI I/Q pairs between the spur component $K_{2,1}(j\Omega)$ and the fundamental signal term $K_{2,0}(j\Omega)$. The mapping into an equivalent I/Q mismatch problem allows for adaptive statistical learning algorithms, which were originally developed

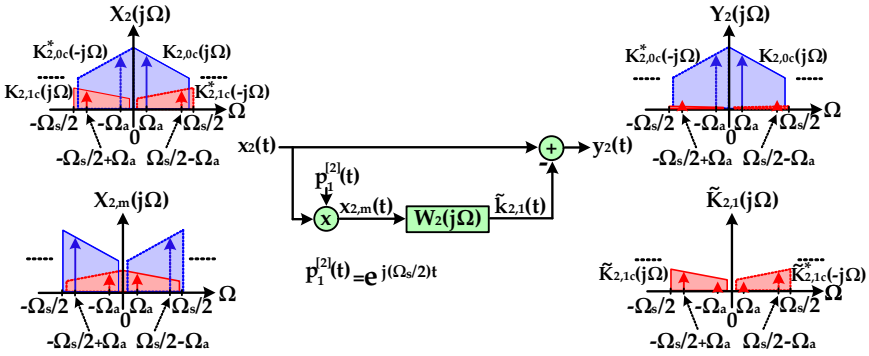

Figure 4.1: 2 TI-ADC mismatch cancellation structure with frequency-shifting by $\Omega_s/2$ together with linear filtering are used to form the cancellation signal.

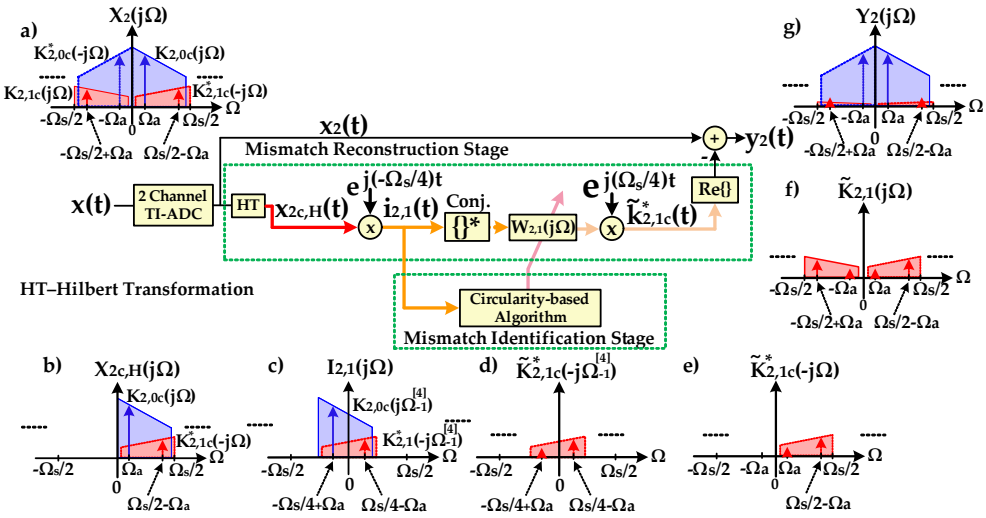

Figure 4.2: Developed *Type I* blind FRM identification and compensation structure for 2 TI-ADC using I/Q signal processing.

for blind I/Q mismatch estimation [6], to be utilized in the blind identification and reconstruction of the estimate of the spur component $K_{2,1}(j\Omega)$.

4.1.1 2 TI-ADC Identification and Compensation Structure - Type I

A MIS $i_{2,1}(t)$ can be generated via (3.51) for the purpose of extracting parameters of the interleaving spur $k_{2,1}(t)$. The identification signal $i_{2,1}(t)$ is fed into the circularity-based algorithm block depicted in Fig. 4.2 from which the following frequency response is

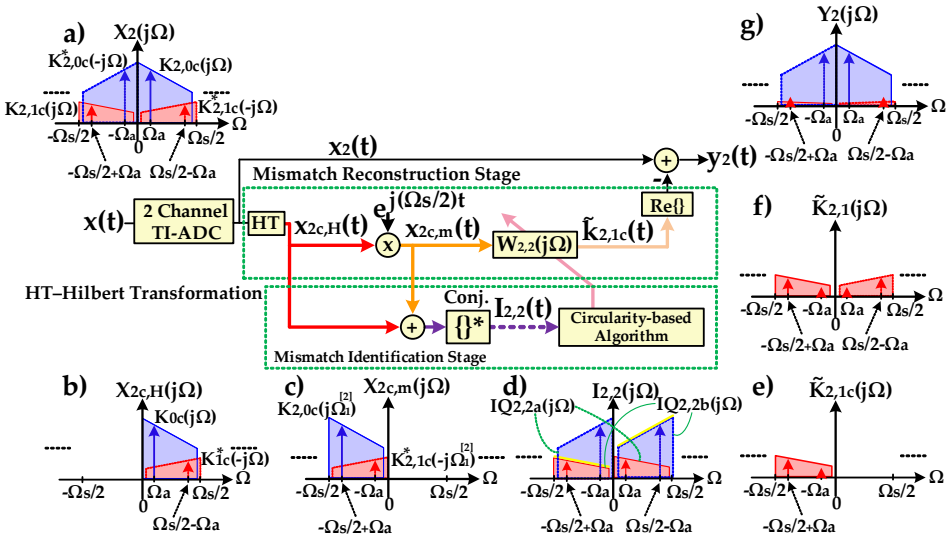

Figure 4.3: Developed *Type II* blind FRM identification and compensation structure for 2 TI-ADC using I/Q signal processing.

obtained for the compensation filter $W_{2,1}(j\Omega)$ given by

$$W_{2,1}(j\Omega) \approx \frac{H^*_{2,1}(-j\Omega^{[4]}_{-1})}{H^*_{2,0}(-j\Omega^{[4]}_{-1})}. \tag{4.1}$$

The obtained filter $w_{2,1}(t)$ is then used to filter $i^*_{2,1}(t)$ followed by frequency shifting it by $\Omega_s/4$ to obtain $\tilde{k}^*_{2,1c}(t)$, an estimate of the complex spur component $k^*_{2,1c}(t)$. Finally, the actual real-valued mismatch estimate $\tilde{k}_{2,1}(t)$ is obtained via $\mathrm{Re}\{\tilde{k}^*_{2,1c}(t)\}$. This process to obtain $\tilde{k}_{2,1}(t)$ is described as

$$\tilde{k}_{2,1}(t) = \mathrm{Re}\{\underbrace{[w_{2,1}(t) * i^*_{2,1}(t)]}_{\tilde{k}^*_{2,1c}(t)}\exp(j[\Omega_s/4]t)\}, \tag{4.2}$$

which is then subtracted from $x_2(t)$ to produce $y_2(t)$. This blind identification and compensation structure is depicted in Fig. 4.2 and is referred to as *Type 1*, essentially combining the basic spur cancellation principle in Fig. 4.1 with the earlier I/Q mismatch mapping developments depicted in Fig. 3.11 a).

4.1.2 2 TI-ADC Identification and Compensation Structure - Type II

A second further improved alternative architecture is presented for the blind identification of the FRM spur $k_{2,1}(t)$. It restructures the previous *Type I* architecture into an alternative processing structure. The restructured architecture performs the same task of extracting the parameters of the interleaving spur $k_{2,1}(t)$ by mapping it into an I/Q mismatch problem as the *Type I* architecture, however with less computational steps. By frequency shifting a copy of $X_{2c,H}(j\Omega)$ by $\Omega_s/2$, $X_{2c,m}(j\Omega)$ is produced with the spectral content as depicted in Fig. 4.3. Now, a MIS, called $i_{2,2}(t)$, for the identification of $K_{2,1c}(j\Omega)$ can be constructed by simply adding up $x^*_{2c,H}(t)$ and $x^*_{2c,m}(t)$ together as

$$i_{2,2}(t) = x^*_{2c,H}(t) + \underbrace{[(x_{2c,H}(t)\exp(j[\Omega_s/2]t))]^*}_{x^*_{2c,m}(t)}. \tag{4.3}$$

The identification signal $i_{2,2}(t)$ has two I/Q mismatched pairs, i.e., $IQ_{2,2a}(j\Omega)$ $IQ_{2,2b}(j\Omega)$, formed as shown in Fig. 4.3 d). The spectral components in $I_{2,2}(j\Omega)$ can be grouped as in

$$I_{2,2}(j\Omega) = \underbrace{K^*_{2,0c}(-j\Omega) + K_{2,1c}(j\Omega_1^{[2]})}_{IQ_{2,2a}(j\Omega)} + \underbrace{K^*_{2,0c}(-j\Omega_1^{[2]}) + K_{2,1c}(j\Omega)}_{IQ_{2,2b}(j\Omega)}. \tag{4.4}$$

$I_{2,2}(j\Omega)$ is then fed into the I/Q mismatch correction block into the circularity-based algorithm block depicted in Fig. 4.3, which yields the following frequency response

$$W_{2,2}(j\Omega) \approx \begin{cases} \frac{H_{2,1}(j\Omega_1^{[2]})}{H_{2,0}(j\Omega_1^{[2]})} & \text{for } 0 \leq \Omega < \Omega_s/2 \\ \frac{H_{2,1}(j\Omega)}{H_{2,0}(j\Omega)} & \text{for} -\Omega_s/2 \leq \Omega < 0\ . \end{cases} \tag{4.5}$$

It is seen in (4.5) that the same frequency response is sketched twice, one in the region $-\Omega_s/2 \leq \Omega < 0$ due to $IQ_{2,2b}(j\Omega)$ and the other in $0 \leq \Omega < \Omega_s/2$ due to $IQ_{2,2a}(j\Omega)$, since there are two I/Q pairs in $I_{2,2}(j\Omega)$, respectively. Since the spectral content of $X_{2c,m}(j\Omega)$ is located between $-\Omega_s/2 \leq \Omega < 0$ and the region $0 \leq \Omega < \Omega_s/2$ is empty, filtering $x_{2c,m}(t)$ using $w_{2,2}(t)$ produces $\tilde{k}_{2,1c}(t)$. Subtracting then $\tilde{k}_{2,1c}(t)$ from $x_2(t)$ gives $y_2(t)$ with an improved FRM RRR. The complete FRM identification and correction process flow is shown in Fig. 4.3 and is referred to as *Type II*. It closely resembles the structure in Fig. 4.1 as it performs the same steps after generating a complex-valued I/Q signal.

In summary, the two methods described above can both perform blind estimation and correction of the 2 TI-ADC FRM. Both the *Type I* and *Type II* architectures

employ complex I/Q signal processing and build upon circularity based algorithms that were originally developed for frequency-dependent I/Q mismatch spur extraction and compensation. The details on the actual blind circularity based estimation algorithm, developed originally in the I/Q mismatch correction framework, will be elaborated in more in section 4.4.

4.2 Identification and Compensation of FRMs in 4 TI-ADC

Similar to the 2 TI-ADC case, the 4 TI-ADC FRM correction process consists of the FRM spurs' identification and compensation stages. The adopted mismatch correction principle consists of recreating accurate estimates of the 4 TI-ADC FRM spur components, i.e., $K_{4,1}(j\Omega)$, $K_{4,2}(j\Omega)$ and $K_{4,3}(j\Omega)$, before subtracting them from the TI-ADC output $x_4(t)$. This requires sufficiently accurate identification of the spur components' frequency responses, i.e., $H_{4,1}(j\Omega)$, $H_{4,2}(j\Omega)$ and $H_{4,3}(j\Omega)$, relative to the desired signal's frequency response, i.e., $H_{4,0}(j\Omega)$. This is achieved by generating appropriate complex-valued MIS in the form of MFI I/Q pairs. Specific MFI I/Q pairs are created between the spur components and the fundamental signal term. This allows for adaptive statistical learning algorithms, which were originally developed for blind I/Q mismatch estimation [6], to be again deployed for blind identification of spur components $K_{4,1}(j\Omega)$, $K_{4,2}(j\Omega)$ and $K_{4,3}(j\Omega)$. The blind identification and correction of the different spur components is carried out in a sequential processing manner. The identification and correction of spur $K_{4,2}$ is carried out first, followed by the identification and correction of spurs $K_{4,1}$ and $K_{4,3}$.

4.2.1 4 TI-ADC Identification Structure Type I

Identification of 4 TI-ADC Spur $K_{4,2}$ *Type I*

An analytic complex-valued signal is first generated from $x_4(t)$ via Hilbert transform as

$$x_{4c,H}(t) = x_4(t) + j[h_{HT}(t) * x_4(t)]. \tag{4.6}$$

The identification of the spur component $K_{4,2}(j\Omega)$ is essentially the same as the 2 TI-ADC case as shown in Fig. 4.3. The MIS $i_{4,2}(t)$, for the identification of $K_{4,2}(j\Omega)$, can be constructed as

$$i_{4,2}(t) = x^*_{4c,H}(t) + \underbrace{x^*_{4c,H}(t)p_2^{[4]}(t)}_{x^*_{4c,H2}(t)}. \tag{4.7}$$

In $I_{4,2}(j\Omega)$, as shown in Fig. 4.4, the spur component $K_{4,2}(j\Omega)$ is deliberately placed at the mirror frequency position of $K_{4,0}(j\Omega)$ and is essentially done in the same manner as in the 2 TI-ADC case. However, $I_{4,2}(j\Omega)$ contains also additional interleaving spur components $K_{4,1}(j\Omega)$ and $K_{4,3}(j\Omega)$ as illustrated in Fig. 4.4. Thus, the spectral components in the mismatch identification signal $I_{4,2}(j\Omega)$ can be decomposed into $I_{4,2}(j\Omega) = I_{4,2D}(j\Omega) + I_{4,2B}(j\Omega)$ where the desired spectral component $I_{4,2D}(j\Omega)$ is of the form

$$I_{4,2D}(j\Omega) = \underbrace{K^*_{4,0c}(-j\Omega) + K_{4,2c}(j\Omega_2^{[4]})}_{IQ_{4,2,1}(j\Omega)} + \underbrace{K^*_{4,0c}(-j\Omega_2^{[4]}) + K_{4,2c}(j\Omega)}_{IQ_{4,2,2}(j\Omega)}, \tag{4.8}$$

where $IQ_{4,2,1}(j\Omega)$ and $IQ_{4,2,2}(j\Omega)$ are the desired I/Q signal pairs in the MIS $i_{4,2D}(t)$ utilized for the identification of spur $K_{4,2}(j\Omega)$ as illustrated in Fig. 4.4 a). The bias spectral component $I_{4,2B}(j\Omega)$, in turn, can be grouped as

$$\begin{aligned} I_{4,2B}(j\Omega) = &\underbrace{K_{4,3c,F}(j\Omega) + K^*_{4,1c,F}(-j\Omega_2^{[4]})}_{B_{4,2,1}(j\Omega)} + \underbrace{K^*_{4,3c,S}(-j\Omega) + K_{4,1c,S}(j\Omega_2^{[4]})}_{B_{4,2,2}(j\Omega)} \\ &+ \underbrace{K^*_{4,1c,F}(-j\Omega) + K_{4,3c,F}(j\Omega_2^{[4]})}_{B_{4,2,3}(j\Omega)} + \underbrace{K_{4,1c,S}(j\Omega) + K^*_{4,3c,S}(-j\Omega_2^{[4]})}_{B_{4,2,4}(j\Omega)} \end{aligned} \tag{4.9}$$

with $B_{4,2,1}(j\Omega)$, $B_{4,2,2}(j\Omega)$, $B_{4,2,3}(j\Omega)$ and $B_{4,2,4}(j\Omega)$ being the bias components in the I/Q signal as seen in Fig. 4.4 b). The first half of the spectral content, originating from $k\Omega_s/2 \leq \Omega < (k+0.5)\Omega_s/2$, is denoted by $K_{4,mc,F}(j\Omega)$. The second half of the spectral content, originating from $(k+0.5)\Omega_s/2 \leq \Omega < (k+1)\Omega_s/2$, is denoted by $K_{4,mc,S}(j\Omega)$.

By feeding $i_{4,2}(t)$ into the I/Q mismatch extraction block illustrated in Fig. 4.4, a measure of the relative strength between the spur $K_{4,2c}(j\Omega)$ and $K^*_{4,0c}(-j\Omega)$ is obtained in the filter $W_{4,2}(j\Omega)$ whose frequency response is of the form

$$W_{4,2}(j\Omega) \approx \begin{cases} \frac{H_{4,2}(j\Omega_2^{[4]})}{H_{4,0}(j\Omega_2^{[4]})} + B_{4,2}(j\Omega) & \text{for} -\Omega_s/2 \leq \Omega < 0 \\ \frac{H_{4,2}(j\Omega)}{H_{4,0}(j\Omega)} + B_{4,2}(j\Omega) & \text{for } 0 \leq \Omega < \Omega_s/2, \end{cases} \tag{4.10}$$

with $B_{4,2}(j\Omega)$ denoting the bias due to the other spur components, which can be ignored for practical RRR values, e.g., 40 dB RRR [P1]. More detailed analysis on the impact of $B_{4,2}(j\Omega)$ can be found in [P1]. By next convolving $w_{4,2}(t)$ with $x_{4c,H2}(t)$ gives an estimate of the spur, denoted by $\tilde{k}_{4,2c}(t)$. An estimate of the actual real-valued spur $k_{4,2}(t)$ can be obtained by taking $\mathrm{Re}\{\tilde{k}_{4,2c}(t)\}$. Subtraction of the spur estimate $\tilde{k}_{4,2}(t)$

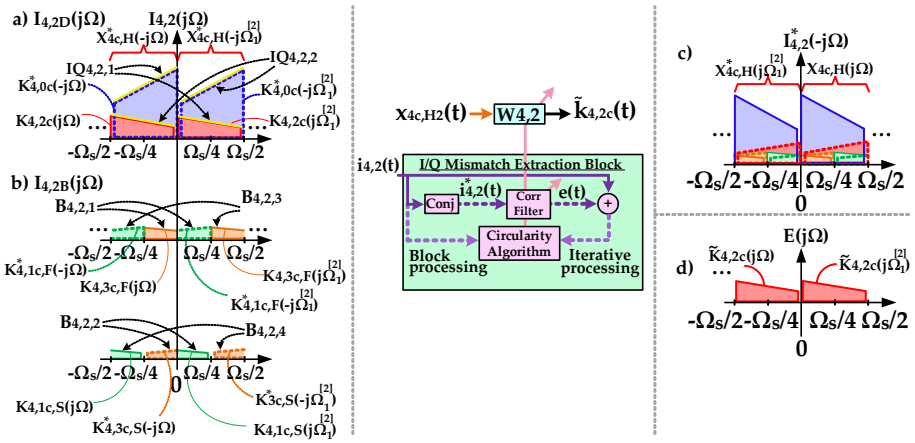

Figure 4.4: MIS $i_{4,2}(t)$ fed into to an I/Q mismatch extraction correction block for reconstruction of the spur $k_{4,2c}(t)$ in 4 TI-ADC.

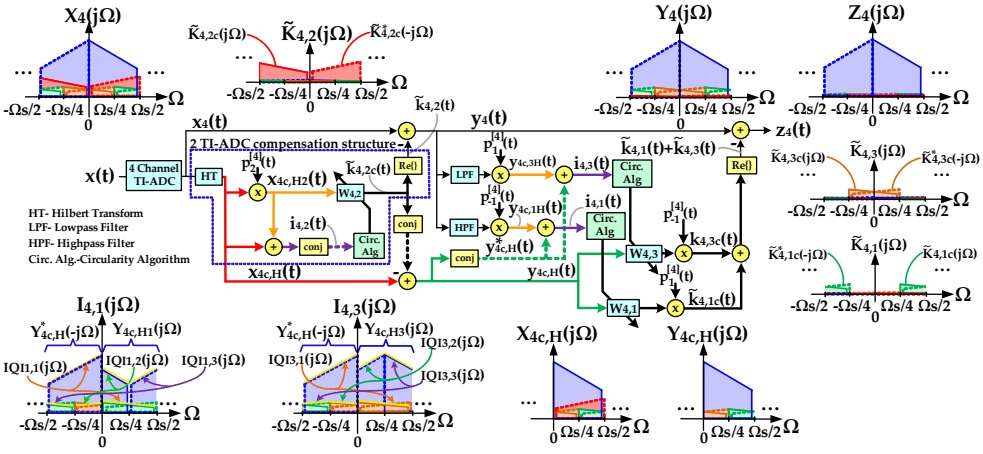

Figure 4.5: Developed *Type I* blind FRM identification and compensation structure for 4 TI-ADC using I/Q signal processing.

from $x_4(t)$ gives the compensated signal $y_4(t)$ of the form

$$y_4(t) = x_4(t) - \mathrm{Re}\{\underbrace{w_{4,2}(t) * x_{4c,H2}(t)}_{\tilde{k}_{4,2c}(t)}\} = \mathrm{Re}\{\underbrace{x_{4c,H}(t) - w^*_{4,2}(t) * x^*_{4c,H2}(t)}_{y_{4c,H}(t)}\}. \tag{4.11}$$

where the spur component $k_{4,2}(t)$ is considerably reduced. This compensation flow is depicted in Fig. 4.5.

Identification of 4 TI-ADC Spurs $K_{4,1}$ and $K_{4,3}$ *Type I*

Following the suppression of spur $k_{4,2}(t)$, the identification and reconstruction of $k_{4,1}(t)$ and $k_{4,3}(t)$ in $y_4(t)$ are to be dealt with next. This task is essentially different compared to the previous stage as $k_{4,1}(t)$ and $k_{4,3}(t)$ do not share common frequencies, as shown already in Fig. 3.7. A MIS for the identification of $k_{4,1}(t)$, denoted by $i_{4,1}(t)$, can be constructed by highpass filtering $y_4(t)$ around $\Omega_s/4 < \Omega < 3\Omega_s/4$ before performing a frequency shift of $-\Omega_s/4$ via multiplication with $p_{-1}^{[4]}(t)$ and adding it together with $y_{4c,H}^*(t)$. This creates mirror-frequency pairs where the spur components $k_{4,1}(t)$ are again in mirror-symmetric manner relative to the fundamental signal term $k_{4,0}(t)$. This is written more formally as

$$i_{4,1}(t) = y_{4c,H}^*(t) + \underbrace{[y_4(t) * h_{HP}(t)]p_{-1}^{[4]}(t)}_{y_{4c,H1}(t)}, \tag{4.12}$$

with $h_{HP}(t)$ denoting the high-pass filter (HPF) impulse response. The principal spectrum of the MIS, $I_{4,1}(j\Omega)$, is illustrated in Fig. 4.5 and whose spectral content is more formally described by

$$\begin{aligned} I_{4,1}(j\Omega) = &\underbrace{K_{4,0c}^*(-j\Omega) + K_{4,1c}(j\Omega_{-1}^{[4]})}_{IQ_{4,1,1}(j\Omega)} + \underbrace{K_{4,0c,S}(j\Omega_{-1}^{[4]}) + K_{4,3c,S}^*(-j\Omega)}_{IQ_{4,1,2}(j\Omega)} \\ &+ \underbrace{K_{4,0c,S}^*(-j\Omega_1^{[4]}) + K_{4,1c,S}(j\Omega)}_{IQ_{4,1,3}(j\Omega)} + K_{4,1c}^*(-j\Omega_{-1}^{[4]}) + K_{4,3c,F}(j\Omega) + K_{4,1c,F}^*(-j\Omega), \end{aligned} \tag{4.13}$$

with $IQ_{4,1,1}(j\Omega), IQ_{4,1,2}(j\Omega), IQ_{4,1,3}(j\Omega)$ being the I/Q mirror pairs created. Now, $i_{4,1}(t)$ can be fed into an I/Q mismatch extraction block which measures the relative strength of the spur $k_{4,1c}(t)$ to $k_{4,0c}^*(t)$ in the form of a filter $W_{4,1}(j\Omega)$, whose frequency response is given by

$$W_{4,1}(j\Omega) \approx \begin{cases} \frac{H_{4,1}(j\Omega_1^{[4]})}{H_{4,0}(j\Omega_1^{[4]})} & \text{for} -\Omega_s/2 \le \Omega < -\Omega_s/4 \\ \frac{H_{4,3}^*(-j\Omega_1^{[4]})}{H_{4,0}^*(-j\Omega_1^{[4]})} & \text{for } -\Omega_s/2 \le \Omega < 0 \\ \frac{H_{4,1}(j\Omega)}{H_{4,0}(j\Omega)} & \text{for } 0 \le \Omega < \Omega_s/2, \end{cases} \tag{4.14}$$

By filtering a copy of $y_{4c,H}(t)$ with $w_{4,1}(t)$ followed by a $\Omega_s/4$ frequency shift, an estimate of the spur $k_{4,1c}(t)$ is reconstructed, which can be written as

$$\tilde{k}_{4,1c}(t) = [w_{4,1}(t) * y_{4c,H}(t)]p_1^{[4]}(t). \tag{4.15}$$

A MIS $i_{4,3}(t)$ can be constructed for the identification of spur $k_{4,3}(t)$, in a similar fashion to MIS of spur $k_{4,1}(t)$, using the insight given by Fig. 3.7. $i_{4,3}(t)$ is constructed by filtering $y_4(t)$ with low-pass filter (LPF) $h_{LPF}(t)$, which has a passband around $-\Omega_s/4 < \Omega < \Omega_s/4$, followed by a frequency shift of $\Omega_s/4$ via multiplication with $p_1^{[4]}(t)$ before adding it with $y^*_{4c,H}(t)$. The overall process of constructing $i_{4,3}(t)$ is formally described in

$$i_{4,3}(t) = y^*_{4c,H}(t) + \underbrace{[y_4(t) * h_{LP}(t)]p_1^{[4]}(t)}_{y_{4c,H3}(t)}. \tag{4.16}$$

The spectral content $I_{4,3}(j\Omega)$ contains specific I/Q mirror-frequency pairs between the spur components $K_{4,3c}(j\Omega)$ and $K^*_{4,0c}(-j\Omega)$. Figure 4.5 depicts a principal spectrum of $I_{4,3}(j\Omega)$ with the spectral content being given by

$$\begin{aligned} I_{4,3}(j\Omega) = &\underbrace{K^*_{4,0c}(-j\Omega) + K_{4,3c}(j\Omega_1^{[4]})}_{IQ_{4,3,1}(j\Omega)} + \underbrace{K^*_{4,0c,F}(-j\Omega_1^{[4]}) + K_{4,3c,F}(j\Omega)}_{IQ_{4,3,2}(j\Omega)} \\ &+ \underbrace{K_{4,0c,F}(j\Omega_1^{[4]}) + K^*_{4,1c,F}(-j\Omega)}_{IQ_{4,3,3}(j\Omega)} + K^*_{4,3c}(-j\Omega_1^{[4]}) + K^*_{4,3c,S}(-j\Omega) + K_{4,1c,F}(j\Omega). \end{aligned} \tag{4.17}$$

$IQ_{4,3,1}(j\Omega), IQ_{4,3,2}(j\Omega)$ and $IQ_{4,3,3}(j\Omega)$ denote the I/Q mirror pairs as shown in Fig. 4.5. By feeding $i_{4,3}(t)$ into an I/Q mismatch extraction block, a compensation filter $W_{4,3}(j\Omega)$ is obtained with the frequency response

$$W_{4,3}(j\Omega) \approx \begin{cases} \frac{H^*_{4,1}(-j\Omega^{[4]}_{-1})}{H^*_{4,0}(-j\Omega^{[4]}_{-1})} & \text{for} -\Omega_s/2 \leq \Omega < -\Omega_s/4 \\ \frac{H_{4,3}(j\Omega^{[4]}_{-1})}{H_{4,0}(j\Omega^{[4]}_{-1})} & \text{for } -\Omega_s/2 \leq \Omega < 0 \\ \frac{H_{4,3}(j\Omega)}{H_{4,0}(j\Omega)} & \text{for } 0 \leq \Omega < \Omega_s/2, \end{cases} \tag{4.18}$$

An estimate of the spur $k_{4,3c}(t)$ can then be reconstructed by filtering $y_{4c,H}(t)$ with $w_{4,3}(t)$ and frequency shifting it by $-\Omega_s/4$ as described in

$$\tilde{k}_{4,3c}(t) = [w_{4,3}(t) * y_{4c,H}(t)]p^{[4]}_{-1}(t). \tag{4.19}$$

By taking $\mathrm{Re}\{\tilde{k}_{4,1c}(t)\}$ and $\mathrm{Re}\{\tilde{k}_{4,3c}(t)\}$, real-valued spur estimates $\tilde{k}_{4,1}(t)$ and $\tilde{k}_{4,3}(t)$ are obtained. By subtracting $\tilde{k}_{4,1}(t)$ and $\tilde{k}_{4,3}(t)$ from $y_4(t)$, the compensated signal $z_4(t)$ is finally obtained, expressed as

$$z_4(t) = y_4(t) - \mathrm{Re}\{\tilde{k}_{4,1c}(t)\} - \mathrm{Re}\{\tilde{k}_{4,3c}(t)\}. \tag{4.20}$$

This final corrected output signal $z_4(t)$ has all three interleaving spur components $K_{4,1}(j\Omega)$, $K_{4,2}(j\Omega)$ and $K_{4,3}(j\Omega)$ reduced. The FRM spur removal process is depicted as in Fig. 4.5 and incorporates all the identification and correction steps of spur components $K_{4,1}(j\Omega)$, $K_{4,2}(j\Omega)$ and $K_{4,3}(j\Omega)$. In general, the transition regions inherent with the use of the digital filters, i.e., HT, LPF, HPF, affect the reference spur components in the constructed identification signals $i_{4,1}(t)$, $i_{4,2}(t)$ and $i_{4,3}(t)$ in the baseband sampling scenario. The filter transition regions prohibit obtaining a complete spur components reference over exactly full digital bandwidth of the system. This, however, is not a problem in an IF-sampling scenario as the usage of anti-aliasing filters anyhow restrict the usage of the full digital BW at the edges [30]. It is also possible to decouple the spur reconstruction stage from its identification stage, so that the identification stage will be running in a separate platform, e.g., for an on-chip implementation [61].

4.2.2 4 TI-ADC Identification Structure Type II

In this subsection, an alternative method for the identification of the interleaving spur components $K_{4,1}(j\Omega)$, $K_{4,2}(j\Omega)$ and $K_{4,3}(j\Omega)$ is presented which does not require the HT, lowpass and highpass filters in the creation of the interleaving MISs. This reduces the computational complexity considerably compared to the developed *Type I* 4 TI-ADC FRM spur identification and compensation structure of subsection 4.2.1.

Spur $K_{4,2}$ Identification - *Type II*

The estimation and reconstruction of $K_{4,2}(j\Omega)$ can be done by creating a complex-valued MIS $i_{k4,2}(t)$ as follows

$$i_{k4,2}(t) = x_4(t)p_{-2}^{[8]}(t). \tag{4.21}$$

In the spectrum of $i_{k4,2}(t)$, $I_{k4,2}(j\Omega)$, shown in Fig. 4.6, it is seen that by performing a frequency shift of $-2\Omega_s/8$ the spur component $K_{4,2}(j\Omega)$ is deliberately placed at the mirror frequency position of $K_{4,0}(j\Omega)$. This allows for the FRM parameter extraction by measuring the relative strength of the spur $K_{4,2}(j\Omega_{-2}^{[8]})$ to $K_{4,0}(j\Omega_{-2}^{[8]})$ [5]. It is seen here that the MFI mapping in the MIS $i_{k4,2}(t)$ is done via a simple frequency translation by $-2\Omega_s/8$, without the HT stage. This therefore reduces the computational complexity considerably and allows using any I/Q mirror frequency correlation measurement method, e.g., the circularity-based algorithm reported in [5], which would yield a filter $w_{k4,2}(t)$

whose frequency response is of the form

$$W_{k4,2}(j\Omega) \approx \begin{cases} \frac{H_{4,2}(j\Omega_{-2}^{[8]})}{H_{4,0}(j\Omega_{-2}^{[8]})} & \text{for } -\Omega_s/2 \leq \Omega < -\Omega_s/4, \\ \frac{H_{4,2}^*(-j\Omega_{-2}^{[8]})}{H_{4,0}^*(-j\Omega_{-2}^{[8]})} & \text{for } -\Omega_s/4 < \Omega \leq \Omega_s/4 \\ \frac{H_{4,2}(j\Omega_{-2}^{[8]})}{H_{4,0}(j\Omega_{-2}^{[8]})} & \text{for } \Omega_s/4 \leq \Omega < \Omega_s/2. \end{cases} \tag{4.22}$$

Using the obtained filter $w_{k4,2}(t)$ to filter $i_{k4,2}^*(t)$ before frequency shifting it by $2\Omega_s/8$ via multiplication with $p_2^{[8]}(t)$, the real valued estimate of the spur $k_{4,2}(t)$, $\tilde{k}_{4,2}(t)$, is obtained. $\tilde{k}_{4,2}(t)$ can then be simply subtracted from $x_4(t)$ to yield a compensated signal $y_4(t)$. The overall process of obtaining $y_4(t)$ is expressed as

$$y_4(t) = x_4(t) - \underbrace{[w_{k4,2}(t) * i_{k4,2}^*(t)]p_2^{[8]}(t)}_{\tilde{k}_{4,2}(t)}, \tag{4.23}$$

in which the spur component $k_{4,2}(t)$ is considerably reduced as shown in Fig. 4.6.

Spur K1 and K3 Identification - *Type II*

In the subsequent stage, a MIS, labeled $i_{k4,13}(t)$, is constructed for the joint estimation and reconstruction of $K_{4,1}(j\Omega)$ and $K_{4,3}(j\Omega)$ via frequency shifting $y_4(t)$ by $-\Omega_s/8$ as described in

$$i_{k4,13}(t) = y_4(t)p_{-1}^{[8]}(t), \tag{4.24}$$

In $I_{k4,13}(j\Omega)$, shown in Fig. 4.6, it is seen that after the $-\Omega_s/8$ frequency shift, the spur component $K_{4,3c}^*(-j\Omega)$ is deliberately placed at the mirror frequency position of $K_{4,0c}(j\Omega)$. At the same time, the $-\Omega_s/8$ frequency shift also places the spur component $K_{4,1c}(j\Omega)$ at the mirror frequency position of $K_{4,0c}^*(-j\Omega)$. The I/Q mismatch MFI based algorithms can therefore once again be utilized to extract the FRM parameters using $i_{k4,13}(t)$. By inputting $i_{k4,13}(t)$ into a MFI extraction algorithm, the relative strength of the spur $K_{4,1c}(j\Omega_1^{[8]})$ to $K_{4,0c}^*(-j\Omega_1^{[8]})$ and $K_{4,3c}^*(-j\Omega_1^{[8]})$ to $K_{4,0c}(j\Omega_1^{[8]})$ can be measured and a filter $w_{k4,13}(t)$ is obtained whose frequency response is of the form

$$W_{k4,13}(j\Omega) \approx \begin{cases} \frac{H_{4,1}(j\Omega_1^{[8]})}{H_{4,0}(j\Omega_1^{[8]})} & \text{for } -\Omega_s/2 \leq \Omega < -3\Omega_s/8, \\ \frac{H_{4,3}^*(-j\Omega_1^{[8]})}{H_{4,0}^*(-j\Omega_1^{[8]})} & \text{for } -3\Omega_s/8 \leq \Omega < \Omega_s/8 \\ \frac{H_{4,1}(j\Omega_1^{[8]})}{H_{4,0}(j\Omega_1^{[8]})} & \text{for } \Omega_s/8 \leq \Omega < \Omega_s/2. \end{cases} \tag{4.25}$$

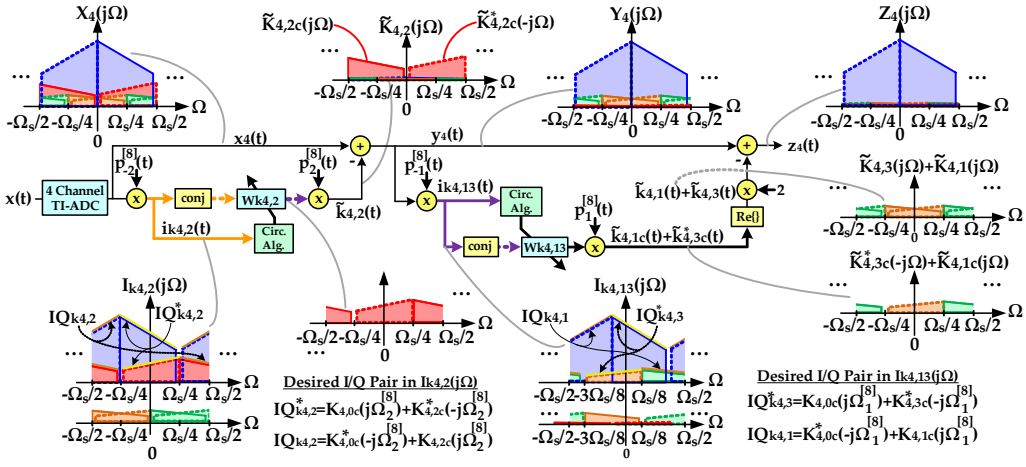

Figure 4.6: Developed *Type II* blind FRM identification and compensation structure for 4 TI-ADC using I/Q signal processing.

By filtering $i^*_{k4,13}(t)$ with the obtained filter $w_{k4,13}(t)$ and then frequency shifting it by $\Omega_s/8$ via multiplication with $p_1^{[8]}(t)$, estimates of the spurs $k_{4,1c}(t)$ and $k^*_{4,3c}(t)$, denoted with $\tilde{k}_{4,1c}(t)$ and $\tilde{k}^*_{4,3c}(t)$, are obtained. Finally, taking $2 \times \mathrm{Re}\{\tilde{k}_{4,1c}(t) + \tilde{k}^*_{4,3c}(t)\}$ yields estimates of the actual real-valued spurs $k_{4,1}(t)$ and $k_{4,3}(t)$ which can be subtracted from $x_4(t)$ giving a compensated signal $y_4(t)$ of the form

$$z_4(t) = y_4(t) - \underbrace{2 \times \mathrm{Re}\{[w_{k4,13}(t) * i^*_{k4,13}(t)]p_1^{[8]}(t)\}}_{\tilde{k}_{4,1}(t)+\tilde{k}_{4,3}(t)}. \tag{4.26}$$

where the spur components $k_{4,1}(t)$ and $k_{4,3}(t)$ are considerably reduced as seen in Fig. 4.6. The joint identification of $k_{4,1}(t)$ and $k_{4,3}(t)$ is another improvement over the prior 4 TI-ADC Type-I method, which identifies $k_{4,1}(t)$ and $k_{4,3}(t)$ separately.

4.2.3 Computational Complexity Analysis

A brief computational complexity analysis of key signal processing operations in the TI-ADC FRM identification and correction architectures is presented in this subsection. The goal is to give a brief overview and estimate of the required multiplier elements for the signal processing operations. The computational complexity analysis is separated into two parts, i.e., the interleaving FRM identification part and FRM reconstruction part.

First, the computational complexity of the TI-ADC's FRM spur identification part is analyzed. The HT is a signal processing operation utilized to obtain the complex-valued analytical signal of the TI-ADC output, i.e., $x_{2c,H}(t)$, for the proposed 2-channel TI-ADC

Type 1 and *Type 2* FRM compensation architecture depicted in Fig. 4.2 and Fig. 4.3. The HT is also utilized in the 4-channel TI-ADC *Type 1* FRM compensation architecture to obtain $x_{4c,H}(t)$ as depicted in Fig. 4.5. A total of $N_H/2$ real valued multiplications would be required due to the anti-symmetric Hilbert filter coefficients, i.e., employing a $\sim$ 100-tap would require $\sim$50 real multiplications. The 4-channel TI-ADC *Type 1* FRM identification part also requires a highpass and a lowpass filter, whose filter orders are denoted by N_{HP} and N_{LP}. These highpass and lowpass filters can be implemented using a halfband filter thus reducing their actual required multiplications to $N_{HP}/2$ and $N_{LP}/2$, i.e., using a $\sim$ 100-tap would result in $\sim$50 real multiplications. It is noted that the 4-channel TI-ADC *Type 2* FRM compensation architecture depicted in Fig. 4.6 does not require any Hilbert, lowpass and highpass filtering in its MISs' construction in the FRM identification path.

The $\pm\Omega_s/2$ and $\pm\Omega_s/4$ frequency shifting operations are required in the 2-channel TI-ADC *Type 1* and *Type 2* and 4-channel TI-ADC *Type 1* correction architectures. Frequency shifting a signal by $\pm\Omega_s/2$ amounts to multiplication by $\pm\{1, -1, 1, -1...\}$ and frequency shifting a signal by $\pm\Omega_s/4$ amounts to multiplication by $\pm\{1, j, -1, -j, 1, j, ...\}$ which consequently has negligible complexity. The 4-channel TI-ADC *Type 2* FRM compensation architecture requires $\pm\Omega_s/8$ frequency shifts. Frequency shifts by $\pm\Omega_s/8$ requires multiplication with $\pm\{1, (1+j)/\sqrt{2}, j, (-1+j)/\sqrt{2}, -1, (-1-j)/\sqrt{2}, -j, (1-j)/\sqrt{2}, 1, ...\}$. The complex multiplication of every alternate output sample with $1/\sqrt{2}$ increases computational complexity. However, it can be seen that the $\pm\Omega_s/8$ frequency shifting requires much less multiplication operations compared to the HT, LPF or HPF filtering operations.

The computational complexity of the circularity based algorithm, i.e., the required computation operation is mostly left out of this analysis. The circularity based algorithm's computational complexity depends upon if a block-based or iterative sample-based variant is taken and which variant of the circularity based algorithm is used, as mentioned in section 4.4. These different variants lead to different computational complexity [4, 40, 51, 52, 83]. If an iterative circularity based algorithm, e.g., comparable to (4.42) and (4.43) as shown in section 4.4, is used to calculate the complex compensation filter of length N_w, then $2N_w$ complex multiplications and $2N_w$ real multiplications are needed per iteration. This amounts to $10N_w$ real multiplications per iteration, e.g., for a 16-tap complex compensation filter, 160 real multiplication would be required per iteration.

Next, TI-ADC's FRM spur reconstruction part's computational complexity is analyzed. As shown earlier, the computational resources of the frequency shifting operations by $\pm\Omega_s/2$ and $\pm\Omega_s/4$ are negligible. The resources required for the $\pm\Omega_s/8$ frequency shift is relatively minimal. Each of the TI-ADC FRM spur reconstruction filters would

require N_w complex multiplications or $4N_w$ real multiplication per iteration. For a 16-tap complex compensation filter, this would amount to 64 real multiplications in the 2-channel TI-ADC *Type 1* & *Type 2* FRM compensation architecture case and 192 multiplications in the 4-channel TI-ADC *Type 1* FRM compensation architecture case. The 2-channel TI-ADC's *Type 1* & *Type 2* as well as the 4-channel TI-ADC *Type 1* FRM compensation architecture requires the HT filtering along with the TI-ADC FRM spurs' complex correction filters. Assuming a 100-tap Hilbert filter with anti-symmetric coefficients and 16 taps FRM spur compensation filters, this results to 114 real multiplications in the 2-channel TI-ADC case and 242 real multiplications for the 4-channel TI-ADC cases. For the 4-channel TI-ADC *Type 2* FRM compensation architecture, which does not require the HT and has two 16 taps FRM spur compensation filters, about 128 real multiplications are required. This shows about $\sim 45\%$ reduction in the total number of multiplications required compared to the the 4-channel TI-ADC *Type 1* FRM compensation architecture. The mismatch identification part does not have to be continuously running as opposed to the mismatch reconstruction part. Therefore, the mismatch identification part can be performed at a slower rate and with a smaller amount of computational resources.

4.3 Identification and Compensation of FRMs in I/Q Downconversion 2 TI-ADC

In this section, the behavioral model in (3.44) is used to develop a blind identification and correction of the FRM spurs. In (3.44) it is seen that the individual spur components are related to the fundamental signal term through (*i*) complex-conjugation, (*ii*) frequency shift by $\Omega_s/2$ and (*iii*) both complex-conjugation and frequency shift by $\Omega_s/2$. The observed signal's FRM spurs' identification is done in a cascaded manner building on this knowledge of the FRM spur structure in (3.44). The identification of the basic I/Q image spur $v_{2,IQ}(t)$ is carried out first. The identification of the image of the TI spur $v_{2,IT}(t)$ is carried out next before finally proceeding to the identification of the TI spur $v_{2,TI}(t)$. All of these identification and processing stages are, naturally, in the complex domain. Specific transformations, i.e., conjugation, frequency shifting and partially oversampling by factor of 2 are deployed in order to identify the necessary FRM spur parameters blindly. Specific MFI pairs are created, if not readily available, between each FRM spur and the fundamental term. Doing so allows I/Q mismatch based blind MFI identification algorithms to become applicable in the actual parameter estimation processing [6].

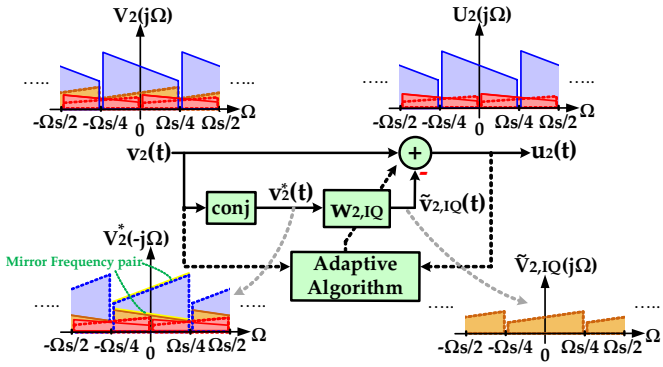

Figure 4.7: Principal I/Q mismatch correction architecture.

4.3.1 I/Q Mismatch Image Spur Identification and Correction

The reconstruction of spur $v_{2,IQ}(t)$ can be achieved by feeding the signal $v_2(t)$ into a MFI identification algorithm which measures the relative correlation strength between the spur $V_{2,IQ}(j\Omega)$ and the desired fundamental signal component $V_{2,LD}(j\Omega)$ [6]. This yields a correction filter $w_{2,IQ}(t)$ which has the frequency response of the form

$$W_{2,IQ}(j\Omega) \approx \frac{H_{T2}(j\Omega)}{H^*_{T0}(-j\Omega)} \tag{4.27}$$

when observed between the region $-\Omega_s/4 \leq \Omega < \Omega_s/4$. Applying the obtained filter $w_{2,IQ}(t)$ on the signal $v_2^*(t)$ creates an estimate of the spur $v_{2,IQ}(t)$, denoted by $\tilde{v}_{2,IQ}(t)$. $\tilde{v}_{2,IQ}(t)$ can then be subtracted from $v_2(t)$ to yield a compensated signal $u_2(t)$ of the form

$$u_2(t) = v_2(t) - \underbrace{[w_{2,IQ}(t) * v_2^*(t)]}_{\tilde{v}_{2,IQ}(t)}. \tag{4.28}$$

which leads to the spur component $v_{2,IQ}(t)$ being considerably reduced as depicted in Fig. 4.7.

4.3.2 TI Image Spur Identification and Correction

In the next stage, a MIS $i_{2,IT}(t)$ is constructed for the estimation and reconstruction of the spur component $V_{2,IT}(j\Omega)$. $i_{2,IT}(t)$ is constructed via frequency-shifting the signal $u_2(t)$ by a factor of $-1/4$ of the angular sampling frequency of the I and Q branch, which for the angular sampling frequency of $\Omega_s/2$ amounts to a shift by $-\Omega_s/8$ as described in

$$i_{2,IT}(t) = u_2(t)p^{[8]}_{-1}(t), \tag{4.29}$$

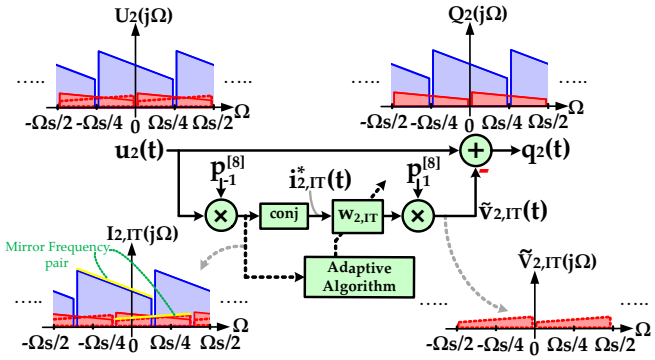

Figure 4.8: Proposed blind mismatch identification and compensation structure for interleaving mismatch's image spur correction for two-channel IQ-TIC.

In the spectrum of $i_{2,IT}(t)$, illustrated in Fig. 4.8, it can be observed that after the $-\Omega_s/8$ frequency shift, the spur component $V_{2,IT}(j\Omega)$ in $U_2(j\Omega)$ is strategically placed at the mirror frequency position of the shifted $V_{2,LD}(j\Omega)$. Hence, the I/Q mismatch based MFI algorithm becomes again applicable, operating on $i_{2,IT}(t)$, to extract the FRM parameters by measuring the strength of $V_{2,IT}(j\Omega)$ relative to $V_{2,LD}(j\Omega)$ in their frequency shifted form. Feeding $i_{2,IT}(t)$ into a MFI extraction algorithm results in a filter $w_{2,IT}(t)$ with the frequency response of the form

$$W_{2,IT}(j\Omega) \approx \frac{H_{T3}(j\Omega_{-1}^{[8]})}{H_{T0}^{*}(-j\Omega_{-1}^{[8]})} \tag{4.30}$$

when observed between the region $-3\Omega_s/8 \leq \Omega < -\Omega_s/8$. Using the obtained filter $w_{2,IT}(t)$ to filter $i_{2,IT}^{*}(t)$ before proceeding with a frequency shift of $\Omega_s/8$ creates an estimate of spur $v_{2,IT}(t)$, $\tilde{v}_{2,IT}(t)$. Now $\tilde{v}_{2,IT}(t)$ can be subtracted from $u_2(t)$ to yield a compensated signal $q_2(t)$ of the form

$$q_2(t) = u_2(t) - \underbrace{[w_{2,IT}(t) * i_{2,IT}^{*}(t)]p_1^{[8]}(t)}_{\tilde{v}_{2,IT}(t)}. \tag{4.31}$$

where the spur component $v_{2,IT}(t)$ is considerably reduced as seen in Fig. 4.8.

4.3.3 TI Spur Identification and Correction

For the estimation and reconstruction of the final remaining spur component $V_{2,TI}(j\Omega)$, a MIS $i_{2,TI}(t)$ is created using the auxiliary signals $q_a(t)$ and $q_b(t)$. The signal $q_2(t)$, which has spurs $v_{2,IQ}(t)$ and $v_{2,IT}(t)$ already suppressed, is first upsampled by a factor of

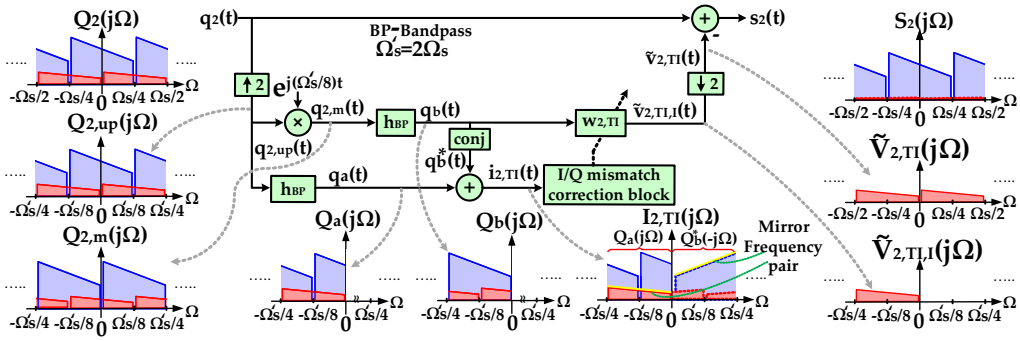

Figure 4.9: Proposed blind mismatch identification and compensation structure for interleaving mismatch's spur correction for 2-channel IQ-TIC.

2 to obtain $q_{2,up}(t)$. In the next step, $q_{2,up}(t)$ is filtered to create $q_a(t)$ using a bandpass filter, $h_{BP}(t)$, which has its passband located between $-\Omega'_s/4 < \Omega < 0$ with $\Omega'_s = 2\Omega_s$. $q_a(t)$ provides a reference for the spur component $v_{2,IT}(t)$. Next, the second auxiliary signal, $q_b(t)$, is constructed via performing a $\Omega'_s/8$ frequency shift via multiplication with $\exp(j[\Omega'_s/8]t)$ before applying the bandpass filter $h_{BP}(t)$. It is seen in Fig. 4.9 that the spectrum of $q_b^*(t)$, $Q_b^*(-j\Omega)$, has a free region in the spectrum between $-\Omega'_s/4 < \Omega < 0$ where the interpolated reference of the spur $v_{2,TI}(t)$ present in $q_a(t)$ can be placed. Therefore, $q_a(t)$ and $q_b^*(t)$ are added together to produce the MIS $i_{2,TI}(t)$, as illustrated in Fig. 4.9. The construction of $i_{2,TI}(t)$ can be expressed as

$$i_{2,TI}(t) = \underbrace{\left(q_{2,up}(t) * h_{bp}(t)\right)}_{q_a(t)} + \underbrace{\left(\left[q_{2,up}(t)\exp(j(\Omega'_s/8)t)\right] * h_{bp}(t)\right)}_{q_b(t)}{}^{*}. \tag{4.32}$$

It is seen in Fig. 4.9, that the interpolated spur component $V_{2,TI}(j\Omega)$ is deliberately placed at the mirror frequency position of the interpolated frequency shifted version of $V_{2,LD}^*(-j\Omega)$. This therefore allows for the identification of $V_{2,TI}(j\Omega)$ to be again carried out blindly via the usage of the MFI based algorithm. Feeding $i_{2,TI}(t)$ into a MFI block gives a filter with the frequency response of the form

$$W_{2,TI}(j\Omega) \approx \frac{H_{T1}(j\Omega_{-2}^{[8]})}{H_{T0}(j\Omega_{-2}^{[8]})} \tag{4.33}$$

when intepreted for the region $-\Omega'_s/4 \leq \Omega \leq 0$. Therefore using $w_{2,TI}(t)$ to filter $q_b(t)$ and then resynchronizing the sample rate via a downsampling by a factor of 2, an estimate of $v_{2,TI}(t)$, $\tilde{v}_{2,TI}(t)$, is constructed as illustrated in Fig. 4.9. $\tilde{v}_{2,TI}(t)$ is then simply subtracted from $q_2(t)$ to produce $s_2(t)$. In the final compensated signal $s_2(t)$, all the 3 mismatch spurs $v_{2,IQ}(t)$, $v_{2,TI}(t)$ and $v_{2,IT}(t)$ have been suppressed.

4.4 MFI-based Blind Learning Algorithms

In all of the various cases and the corresponding MISs created in section 4.1, section 4.2 and section 4.3, the mismatch spur to be identified is placed at the mirror frequency position of the desired fundamental signal component. This allows using blind MFI identification techniques such as second order statistics (SOS), e.g. circularity//properness based methods [6], to efficiently estimate the filters, e.g., $w_{2,1}(t), w_{4,2}(t)$ and $w_{2,TI}(t)$, needed to reconstruct estimates of the mismatch spur components, e.g., $k_{2,1}(t), k_{4,2}(t)$ and $v_{2,TI}(t)$.

Below, an arbitrary complex signal signal $v(t)$ is used to describe important SoS functions that are adopted in the estimation and learning algorithms. These are

- the expected value or mean, $\mu = E[v(t)]$.
- the auto-correlation function (ACF),
  $\gamma(\tau) \stackrel{\text{def}}{=} E[v(t)v^*(t-\tau)]$, with τ being the time-lag.
- the complementary auto-correlation function (CACF), $c(\tau) \stackrel{\text{def}}{=} E[v(t)v(t-\tau)]$.

The two fundamental prerequisites for using circularity to learn the optimal filter coefficients are:

- the ideal baseband equivalent signal $v(t)$ has zero mean, i.e., $E[v(t)] = 0$.
- there is no correlation between $v(t)$ and its own complex-conjugate $v^*(t)$ for any given τ, i.e., $c_v(\tau) = E[v(t)v(t-\tau)] = E[v(t)(v^*(t-\tau))^*] = 0$ [6].

In the following developments, the mismatch identification signal $i_{2,2}(t)$ is assumed to demonstrate how the circularity based algorithm can be utilized to obtain the mismatch spur reconstruction filter. For more complete descriptions, refer to the original publications [P1],[P2] and [6]. To illustrate this, let the spectral components in $I_{2,2}(j\Omega)$ with its I/Q pairs, given in (4.4), be first grouped as

$$I_{2,2}(j\Omega) = \underbrace{K^*_{2,0c}(-j\Omega) + K^*_{2,0c}(-j\Omega_1^{[2]})}_{I_{2,2D}(j\Omega)} + \underbrace{K_{2,1c}(j\Omega_1^{[2]}) + K_{2,1c}(j\Omega)}_{I_{2,2M}(j\Omega)}. \tag{4.34}$$

with $I_{2,2D}(j\Omega)$ being the desired spectral component and $I_{2,2M}(j\Omega)$ being the filtered mirror frequencies of $I_{2,2D}(j\Omega)$. Note that $I_{2,2D}(j\Omega)$ and $I_{2,2M}(j\Omega)$ are the same components previously grouped as $IQ_{2,2a}(j\Omega)$ and $IQ_{2,2b}(j\Omega)$ in (4.4) but are now simply grouped differently. The prerequisite to be able to utilize circularity to learn $w_{2,2}(t)$ is that $i_{2,2}(t)$ and its underlying components, $i_{2,2D}(t)$ and $i_{2,2M}(t)$ must have

zero mean, i.e. $E[i_{2,2}(t)] = E[i_{2,2D}(t)] = E[i_{2,2M}(t)] = 0$. The second prerequisite is that $i_{2,2D}(t)$ and $i_{2,2M}(t)$ must be circular, i.e., the CACF of, e.g., $i_{2,2D}(t)$ is of the form

$$\begin{aligned} c_{2,2D}(\tau) &= E[i_{2,2D}(t) i_{2,2D}(t-\tau)] \\ &= E[i_{2,2D}(t)\big(i^*_{2,2D}(t-\tau)\big)^*] = 0, \end{aligned} \tag{4.35}$$

implying that there should be no correlation between $i_{2,2D}(t)$ and $i^*_{2,2D}(t)$ for any given time lag τ [6]. However, the MIS $i_{2,2}(t)$ contains $i_{2,2D}(t)$ overlayed with a filtered version of $i^*_{2,2D}(t)$, in the form of $i_{2,2M}(t)$, due to the TI-ADC mismatch. Thus $i_{2,2}(t)$ will correlate with $i^*_{2,2}(t)$ and this results in $E[i_{2,2}(t)^2] \neq 0$ or more generally $E[i_{2,2}(t) i_{2,2}(t-\tau)] \neq 0$. Hence, circularity can be utilized to measure the content of $i_{2,2M}(t)$ in $i_{2,2D}(t)$ and thus to blindly identify the filter $w_{2,2}(t)$ needed to reconstruct the associated $i_{2,2M}(t)$ spur.

In a simple frequency-independent case, the filter parameter $w_{2,2}$ restoring the circularity can be calculated as [6]

$$w_{2,2} = \frac{c_{i2,2}(0)}{\gamma_{i2,2}(0) + \sqrt{\gamma^2_{i2,2}(0) - |c_{i2,2}(0)|^2}}, \tag{4.36}$$

where $c_{i2,2}(0) = E[(i_{2,2}(t))^2]$, $\gamma_{i2,2}(0) = E[|i_{2,2}(t)|^2]$ and the compensation filter impulse response is $w_{2,2}(t) = w_{2,2}\delta(t)$. In practice, the sample statistics over a block of samples can be used to approximate the involved ensemble statistics. An approximated simplified estimator, stemming from (4.36), reads

$$\tilde{w}_{2,2} = \frac{c_{i2,2}(0)}{2\gamma_{i2,2}(0)}. \tag{4.37}$$

The above frequency-independent solutions can, however, only correct for the mean value of the actual frequency-dependent mismatches. In order to accommodate true frequency-dependent mismatch identification and correction, the above frequency-independent solution in (4.37) can be extended as follows. By first expanding the circularity-based cost function $E[(i_{2,2}(t))^2]$ into $E[\mathbf{i}_{2,2}(t) i_{2,2}(t)]$, with $\mathbf{i}_{2,2}(t) = [i_{2,2}(t), i_{2,2}(t-1), \ldots, i_{2,2}(t-N+1)]^T$, a frequency-dependent identification solution, represented here as an N-tap compensation filter $\tilde{\mathbf{w}}_{2,2}$, can be calculated as [6]

$$\tilde{\mathbf{w}}_{2,2} = [\mathbf{\Gamma}_{i2,2} + \bar{\mathbf{\Gamma}}_{i2,2}]^{-1} \mathbf{c}_{i2,2} \tag{4.38}$$

where

$$\mathbf{c}_{i2,2} = E[\mathbf{i}_{2,2}(t) i_{2,2}(t)] = [c_{i2,2}(0),\ c_{i2,2}(1),\ \ldots, c_{i2,2}(N-1)]^T, \tag{4.39}$$

$$\mathbf{\Gamma}_{i2,2} = \begin{bmatrix} \gamma_{i2,2}(0) & \gamma_{i2,2}(1) & \dots & \gamma_{i2,2}(N-1) \\ \gamma^*_{i2,2}(1) & \gamma_{i2,2}(0) & \dots & \gamma_{i2,2}(N-2) \\ \vdots & \vdots & \ddots & \vdots \\ \gamma^*_{i2,2}(N-1) & \gamma^*_{i2,2}(N-2) & \dots & \gamma_{i2,2}(0) \end{bmatrix}, \tag{4.40}$$

$$\bar{\mathbf{\Gamma}}_{i2,2} = \begin{bmatrix} \gamma_{i2,2}(0) & \gamma_{i2,2}(1) & \dots & \gamma_{i2,2}(N-1) \\ \gamma_{i2,2}(1) & \gamma_{i2,2}(2) & \dots & \gamma_{i2,2}(N) \\ \vdots & \vdots & \ddots & \vdots \\ \gamma_{i2,2}(N-1) & \gamma_{i2,2}(N) & \dots & \gamma_{i2,2}(2N-2) \end{bmatrix}. \tag{4.41}$$

As observed in (4.38), this solution requires computing $[\mathbf{\Gamma}_{i2,2} + \bar{\mathbf{\Gamma}}_{i2,2}]^{-1}$ and the computational complexity increases with the number of taps N. An alternative computing method can be used where the above block solution in (4.38) is iteratively calculated, in the form of $\mathbf{w}_{2,2it}$, by using an internal feedback signal $f_{2,2}(t)$ as given in [5]

$$\mathbf{w}_{2,2it}(t) = \mathbf{w}_{2,2it}(t-1) - \boldsymbol{\lambda} \boldsymbol{f}_{2,2}(t-1) f_{2,2}(t-1). \tag{4.42}$$

Here, $\mathbf{w}_{2,2it}(t) = [w_{2,2it1},\ w_{2,2it2}, \dots, w_{2,2itN}]^T$, $\boldsymbol{f}_{2,2}(t) = [f_{2,2}(t),\ f_{2,2}(t-1), \cdots, f_{2,2}(t-N+1)]^T$ and $\boldsymbol{\lambda} = diag[\lambda_1,\ \lambda_2,\ \cdots, \lambda_N]$ denotes a diagonal step-size matrix controlling the convergence rate. Then, $\mathbf{w}_{2,2it}(t)$ is applied in the next iteration in filtering the identification signal $i_{2,2}(t)$ as given by

$$f_{2,2}(t) = i_{2,2}(t) - \mathbf{w}^T_{2,2it}(t) \boldsymbol{i}^*_{\mathbf{2,2}}(t), \tag{4.43}$$

where $\boldsymbol{i}^*_{2,2}(t) = [i^*_{2,2}(t),\ i^*_{2,2}(t-1),\ \cdots, i^*_{2,2}(t-N+1)]^T$. The initial value for $\mathbf{w}_{2,2it}(t)$ can be set to all zeros and its convergence is reached when $\boldsymbol{f}_{2,2}(t-1) f_{2,2}(t-1) \approx 0$, thus resulting in $\mathbf{w}_{2,2it}$ performing similar to $\mathbf{w}_{2,2}$ [5, 6].

The circularity-based learning algorithm adopted here represents only one of the different variations available in the literature [4, 40, 51, 52, 83]. The exact algorithm deployed to measure the circularity is essentially decoupled from the mismatch identification architecture presented for the various mismatch induced spur components, which places the mismatch spurs at the mirror frequency position and enables using mirror frequency correlation-based algorithms such as circularity. Thus, the same mismatch identification architecture can be used in conjunction with any other circularity-related computing algorithms with different learning and tracking capabilities [4].

An important condition to ensure successful blind identification can be summarized using a wideband signal as follows. For a wideband composite input signal consisting of multiple modulated carrier waveforms, the complex baseband equivalents of the individual modulated carriers are circular (which applies, e.g., to all typical M-PSK

and M-QAM modulated signals) and mutually uncorrelated. Therefore, the blind identification can be successfully carried out even if the original input signal components and spurious components are overlapping. The zero mean requirement on the input signal needed to utilize S.O.S. based learning methods can be ensured via notch filtering the mismatch identification signal before it is fed into the mismatch identification block to extract the mismatch parameters, [87].

CHAPTER 5

Hardware Measurements and Mismatch Correction Performance Evaluation

This chapter addresses the performance evaluation of the mismatch spur removal algorithms developed in chapter 4 and in the original thesis publications [P1]-[P6]. The validation is done using measurement data obtained from actual TI-ADC Hardware (HW) platforms. In total, 3 different HW platforms are utilized in the measurements, namely, a narrowband high resolution TI-ADC, a wideband medium resolution TI-ADC and a wideband I/Q downconversion unit combined with medium resolution TI-ADC. Data collected from these HW measurements are then used in the testing of the mismatch correction algorithms to evaluate and demonstrate the performance of the proposed correction algorithms. More examples can be found in the original publications [P1]-[P8].

5.1 Description of Various Measurement HW Platforms

For the purpose of validating and testing the mismatch correction architectures, the 3 different HW platforms which were utilized in the measurement are the following:

1. two 16-bit LTC2208 [41] ADCs operated in the time interleaved manner on PCB level as illustrated in Fig. 5.1.

2. a 4-channel 12-bit TI-ADC, ADC12D1800RF [80] as illustrated in Fig. 5.2.

3. a wideband I/Q downconversion circuitry together with the ADC12D1800RF in a 2-channel TI-ADC mode in its I and Q branch as illustrated in Fig. 5.3.

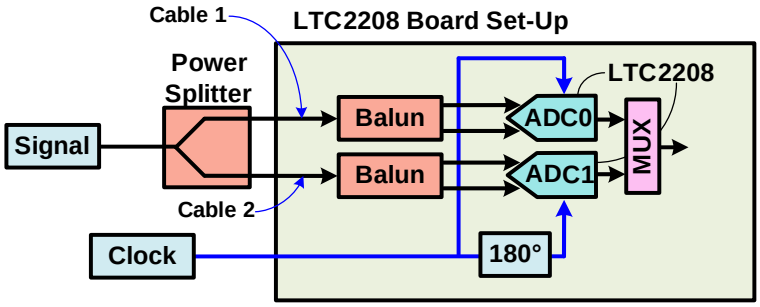

Figure 5.1: Measurement HW configuration of the two 16-bit LTC2208 ADCs operated in the time interleaved manner on PCB level.

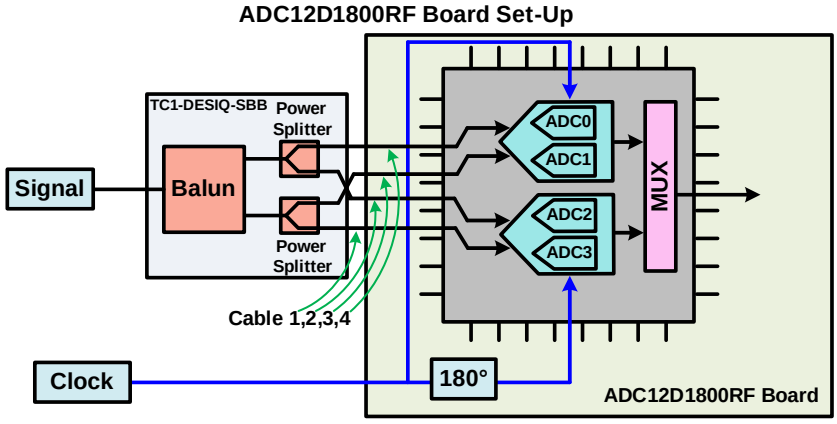

Figure 5.2: Measurement HW configuration of the 4-channel TI-ADC ADC12D1800RF in DESCLKIQ mode.

5.2 FRM Spur Characteristics of Measured HW

5.2.1 LTC2208 HW FRM Measurement

Two state-of-the-art 16-bit ADCs, each having a sampling rate of 120 MHz, were interleaved to achieve an interleaved sampling frequency of ~ 240 MHz. The hardware configuration diagram is shown in Fig. 5.1 . This setup is measured using single tone CW signals sweeped across the 1st and 2nd Nyquist zones with a total of about 100 frequency points. The measurements were carried out for different temperature values,

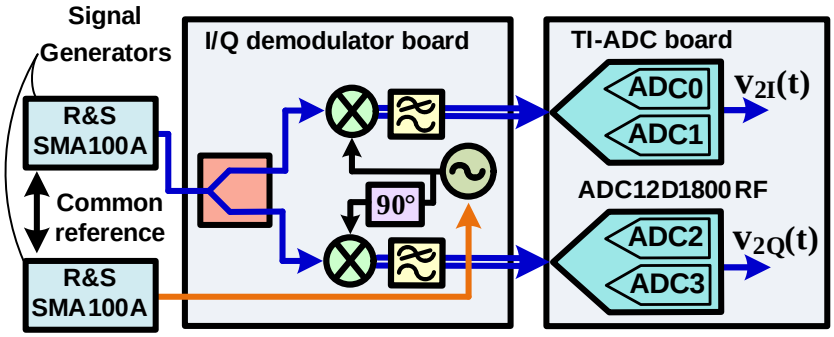

Figure 5.3: Measurement HW configuration of I/Q downconversion circuitry in combination with the ADC12D1800RF operated in 2 TI-ADC mode.

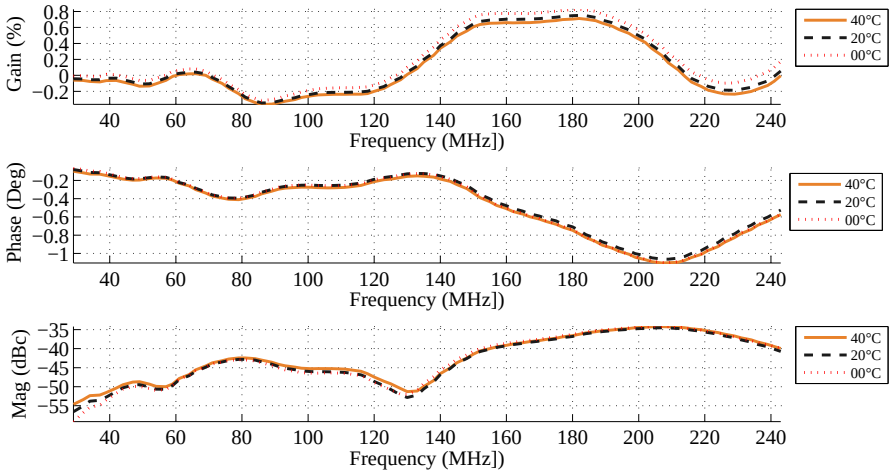

Figure 5.4: Measured FRM spur $k_{2,1}$ (gain and phase mismatch) and the RRR of two interleaved LTC2208 [41] ADCs with single tone CW signals @ -6dBFS input level at 40 °C, 20 °C & 0 °C. The interleaved sampling frequency is about 240 MHz and the mismatch measurement covers the 1st Nyquist zone (0 to 120 MHz) & 2nd Nyquist zone (120 MHz to 240 MHz).

i.e. 40 °C, 20 °C & 0 °C with the hardware placed in a temperature cupboard. The measured 2-channel TI-ADC FRM spurs for each temperature setting are depicted in Fig. 5.4. The data for the TI-ADC mismatch correction prototyping was collected from the LTC2208 evaluation platform hardware and the correction was performed on the PC.

5.2.2 ADC12D1800RF HW FRM Measurement

The ADC12D1800RF is set to operate at a sampling frequency of 2.9 GHz and using single tone CW signals swept across the 1st and 2nd Nyquist zones, estimates of the 4-channel TI-ADC FRM spurs for this hardware configuration are first measured for a total of about 100 frequency points at different temperature values, i.e. 40 °C, 20 °C & 0 °C. The measured strengths of the spurs $K_{4,1}(j\Omega), K_{4,2}(j\Omega)$ and $K_{4,3}(j\Omega)$ at 40 °C, 20 °C & 0 °C respectively are depicted in Fig. 5.5, Fig. 5.6 and Fig. 5.7. These measurements were carried out in the DESIQCLK mode, in which the ADC has the largest analog BW of 2.7 GHz available but it requires careful analog hardware matching when supplying the differential input signal to the two ADC channels [80] to minimize the interleaving mismatches. During these measurements, a single balun board, TC1 DESIQ, is used when providing the differential input signals to the two 1.8 GHz ADCs [81]. Due to the balun board's limited matching accuracy and the need to use external carefully matched cables to connect the inputs, additional frequency response mismatch is introduced. Consequently, the interleaving mismatch spurs cannot be significantly reduced by adjusting the clock phase alone [81]. As can be inferred from Fig. 5.5, Fig. 5.6 and Fig. 5.7, the performance of any offline designed mismatch correction filter, e.g., [72], will degrade during the TI-ADC's operation due to mismatch variations, stemming from temperature changes. This clearly demonstrates the need for either regular recalibration or adaptive online algorithms [70]. The data for the TI-ADC mismatch correction prototyping was collected from the ADC12D1800RF evaluation platform hardware and the correction was performed on the PC.

5.2.3 I/Q Downconversion Circuitry & ADC12D1800RF HW FRM Measurement

An experimental hardware platform was constructed for preliminary concept and model verification purposes, consisting of an I/Q demodulator circuitry followed by 2-channel TI-ADC HW [80] per I and Q branch as depicted in Fig. 5.3. The TI-ADC's aggregate sampling rate in the I and Q branches is 1690 MHz. This setup was measured using a set of single-tone continuous wave (CW) signals which are sequentially fed into the RF input and then downconverted into baseband. The RF center-frequency range used in the measurements was 2.7 GHz, which is also the LO frequency. A set of 22 tones injected sequentially, with tone frequencies ranging between -400MHz to +400MHz relative to the RF center-frequency, is used to measure the spur characteristics of the test setup. The complex signal spectra of the collected data are then evaluated and analyzed on the PC. Figure 5.8 plots the measured spurious components, relative to the fundamental signal term, consisting of the I/Q mismatch spur, i.e., $V_{2,IQ}(j\Omega)$, the interleaving spur,

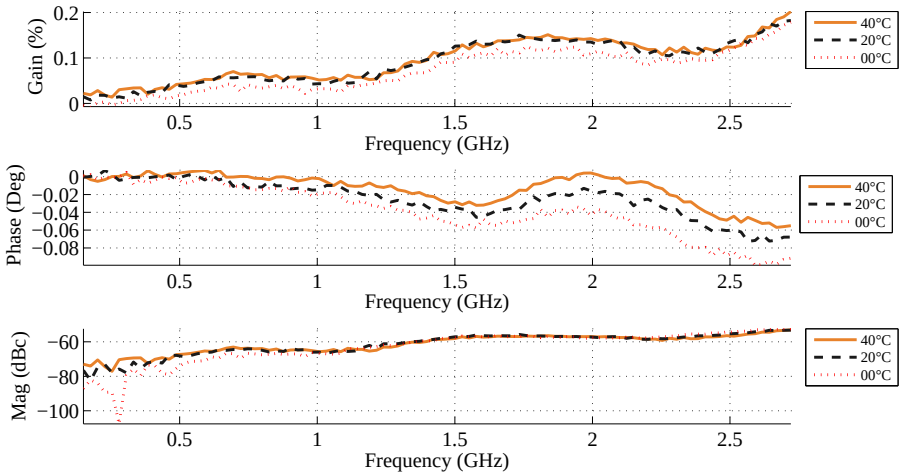

Figure 5.5: Measured FRM spur $k_{4.1}$ (including gain and phase mismatch components) and the RRR of an ADC12D1800RF in DESCLKIQ mode @ -3dBFS at 40 °C, 20 °C and 0 °C. The sampling frequency is 2.9 GHz and the mismatch measurement covers the 1st Nyquist zone (0 to 1.45 GHz) and 2nd Nyquist zone (1.45 GHz to 2.9 GHz).

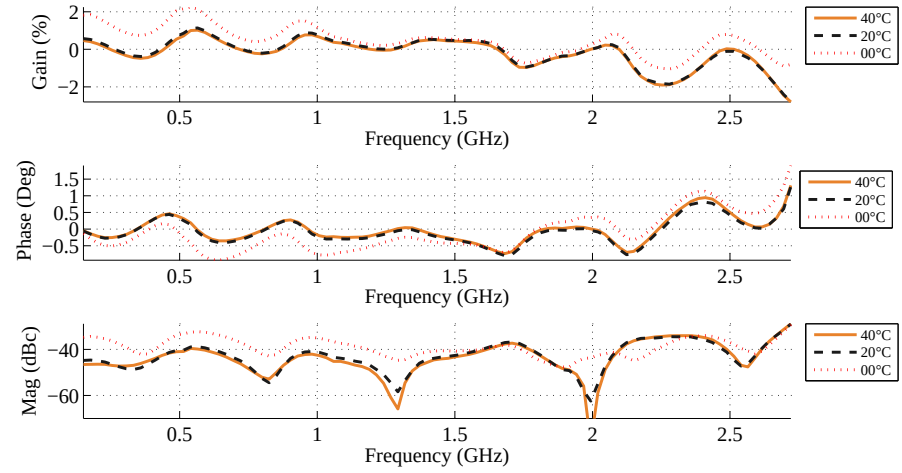

Figure 5.6: Measured FRM spur $k_{4.2}$ (including gain and phase mismatch components) and the RRR of an ADC12D1800RF in DESCLKIQ mode @ -3dBFS at 40 °C, 20 °C and 0 °C. The sampling frequency is 2.9 GHz and the mismatch measurement covers the 1st Nyquist zone (0 to 1.45 GHz) and 2nd Nyquist zone (1.45 GHz to 2.9 GHz).

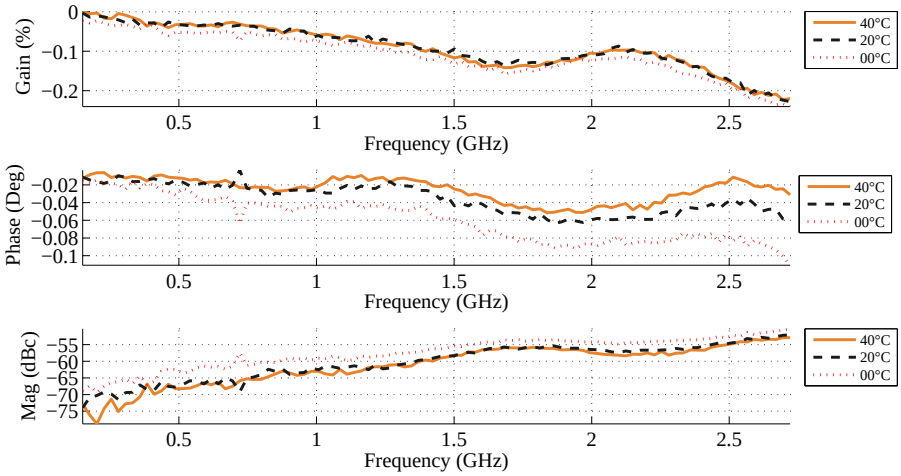

Figure 5.7: Measured FRM spur $k_{4,3}$ (including gain and phase mismatch components) and the RRR of an ADC12D1800RF in DESCLKIQ mode @ -3dBFS at 40 °C, 20 °C and 0 °C. The sampling frequency is 2.9 GHz and the mismatch measurement covers the 1st Nyquist zone (0 to 1.45 GHz) and 2nd Nyquist zone (1.45 GHz to 2.9 GHz).

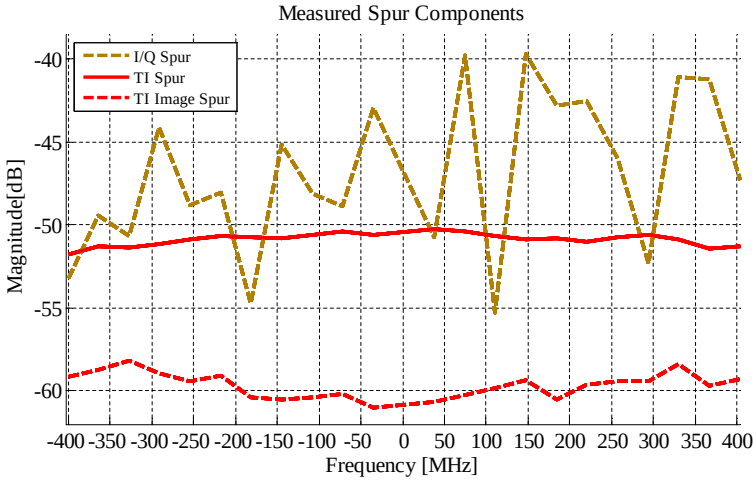

Figure 5.8: Measured suppression of different spurious components for input frequencies ranging between -400 MHz to 400 MHz relative to the 2.7 GHz RF center-frequency.

i.e., $V_{2,TI}(j\Omega)$ and the interleaving spur's image, i.e., $V_{2,IT}(j\Omega)$. It is clear that all three spurious components can limit the SFDR of high-end digital processing systems, thus giving a strong motivation for using digital post-processing methods to suppress all the associated spurs.

5.3 Measured Performance of Proposed Blind Identification and Correction of TI-ADC FRM Spurs

Suitable multi-tone test scenarios are created by adding multiple datasets of single tone signals that were injected into the 1st and 2nd Nyquist zone of the interleaved LTC 2208. This is used to create a challenging scenario to demonstrate and evaluate the TI-ADC's FRM spur correction performance, as seen in Fig. 5.9 and Fig. 5.10. This is also done for the ADC12D1800RF, where suitable multi-tone test scenarios are created by adding multiple datasets of single tone signals. The single tone signals are injected into the first and second Nyquist zones respectively to create a challenging scenario to demonstrate and evaluate the frequency response mismatch correction, as seen in Fig. 5.11 and Fig. 5.12. Creating the multi-tone scenario in such a manner leads to an increased noise spectral density in the respective spectrum. However, this is not an relevant issue for the purpose of evaluating and demonstrating the FRM spur rejection capabilities.

5.3.1 Validation of Proposed Blind Identification and Correction of 2-channel TI-ADC FRM Spurs using Measured Data

The FRM spur correction is first performed using the measured data obtained from the LTC2208. Using 8192 samples of measured data, a 30-tap TI-ADC mismatch spur correction filter is calculated as given in (4.38) using the *Type 1* correction architecture. The magnitude of the interleaving spur $k_{2,1}(t)$, for the multi-tone scenario in both the 1st Nyquist zone and the 2nd Nyquist zone, are reduced to the noise floor level after correction, as seen in Fig. 5.9 for the 1st Nyquist zone and in Fig. 5.10 for the 2nd Nyquist zone, verifying the functionality of the proposed method. The 2 TI-ADC's post correction RRR has increased by approximately 50 dBc.

Next, the 2-channel TI-ADC FRM spurs correction performance is evaluated and illustrated with the proposed *Type 2* blind mismatch identification and correction structure using the measured data from of the 4-channel TI-ADC ADC12D1800RF. The interleaving spur $k_{4,2}(t)$ is in its structure essentially the same as $k_{2,1}(t)$. Therefore, the correction of the spur $k_{4,2}(t)$ is performed with the *Type 2* 2-channel TI-ADC FRM spur correction architecture using 16384 samples of measured data that are used to calculate a 16-tap interleaving FRM spurs correction filter as given in (4.38). The time interleaving spur $k_{4,2}(t)$'s level for the 1st Nyquist zone and for the 2nd Nyquist zone, are reduced to the noise floor level after correction, as seen in Fig. 5.11 for the 1st Nyquist zone and in Fig. 5.12 for the 2nd Nyquist zone, verifying the functionality of the proposed method.

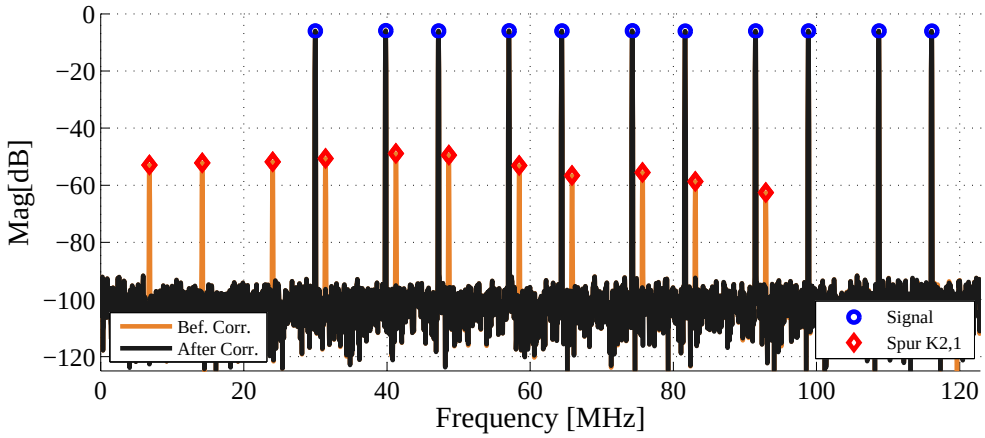

Figure 5.9: Spectrum of two interleaved LTC2208 [41] ADCs with multi-tone scenario in the 1st Nyquist (0 to 120 MHz) zone before and after correction using the proposed *Type 1* 2 TI-ADC FRM compensation architecture shown in Fig. 4.2.

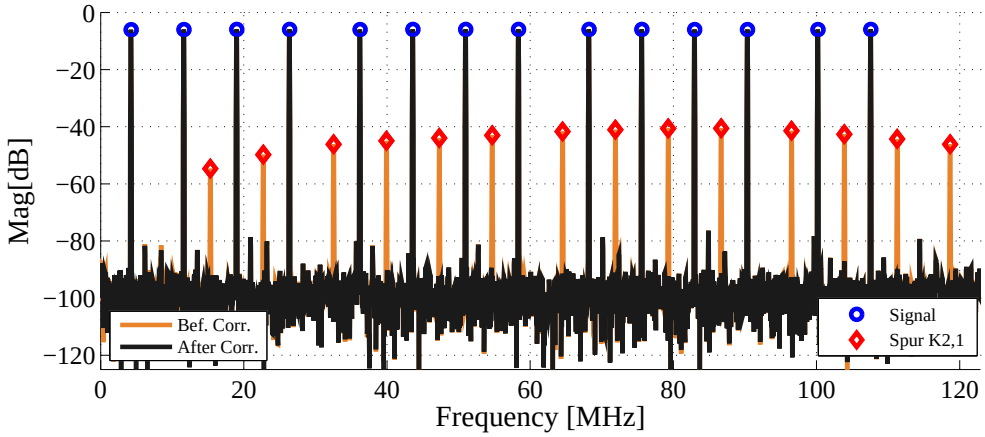

Figure 5.10: Spectrum of two interleaved LTC2208 [41] ADCs with multi-tone scenario in the 2nd Nyquist (120 MHz to 240 MHz) zone before and after correction using the proposed *Type 1* 2 TI-ADC FRM compensation architecture shown in Fig. 4.2.

5.3.2 Validation of Proposed Blind Identification and Correction of 4-channel TI-ADC FRM Spurs using Measured Data

In the next stage, the time interleaving FRM spurs correction performance is tested for 4-channel TI-ADC case using the ADC12D1800RF, in which all 3 interleaving spurs $k_{4,1}(t)$, $k_{4,2}(t)$ and $k_{4,3}(t)$ are mitigated. First, the mitigation of $k_{4,1}(t)$, $k_{4,2}(t)$ and $k_{4,3}(t)$ is

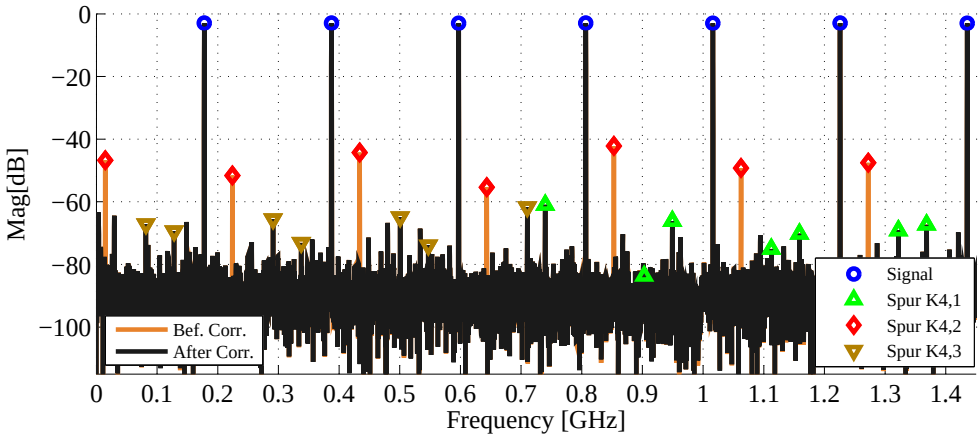

Figure 5.11: Measured ADC12D1800RF multi-tone spectrum at 20 °C in the 1st Nyquist zone (0 to 1.45 GHz) zone before and after correction using the proposed *Type 2* 2 TI-ADC FRM compensation architecture shown in Fig. 4.3.

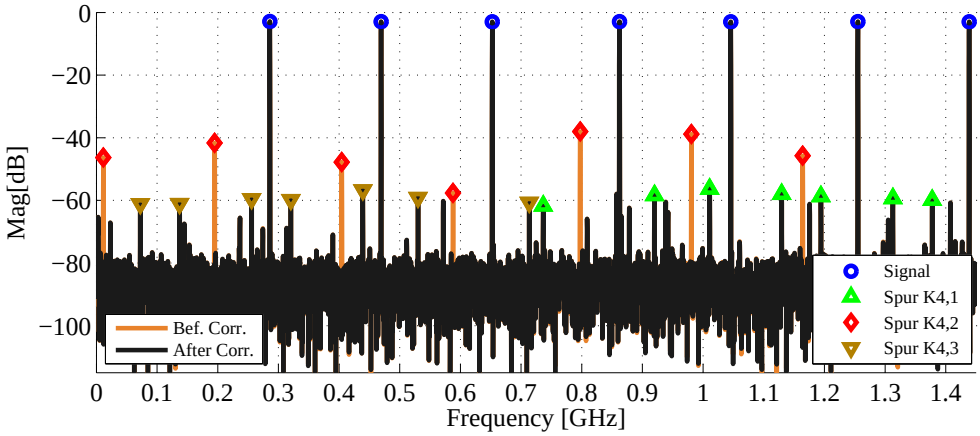

Figure 5.12: Measured ADC12D1800RF multi-tone spectrum at 20 °C in the second Nyquist (1.45 GHz to 2.9 GHz) zone before and after correction using the proposed *Type 2* 2 TI-ADC FRM compensation architecture shown in Fig. 4.3.

evaluated and illustrated with the proposed *Type 1* correction architecture shown in Fig. 4.5. Using the same multi-tone signal set with 16384 measured data samples, as utilized in section 5.3.2 for validating the *Type 2* 2 TI-ADC FRM compensation architecture, 3 sets of 16-tap interleaving FRM spur correction filters are calculated, as given in eq. (4.38), for the spurs $k_{4,1}(t)$, $k_{4,2}(t)$ and $k_{4,3}(t)$ each. The magnitude of the interleaving spurs $k_{4,1}(t)$, $k_{4,2}(t)$ and $k_{4,3}(t)$, for the multi-tone scenario in both the 1st Nyquist zone and for the 2nd Nyquist zone, are reduced to the noise floor level after

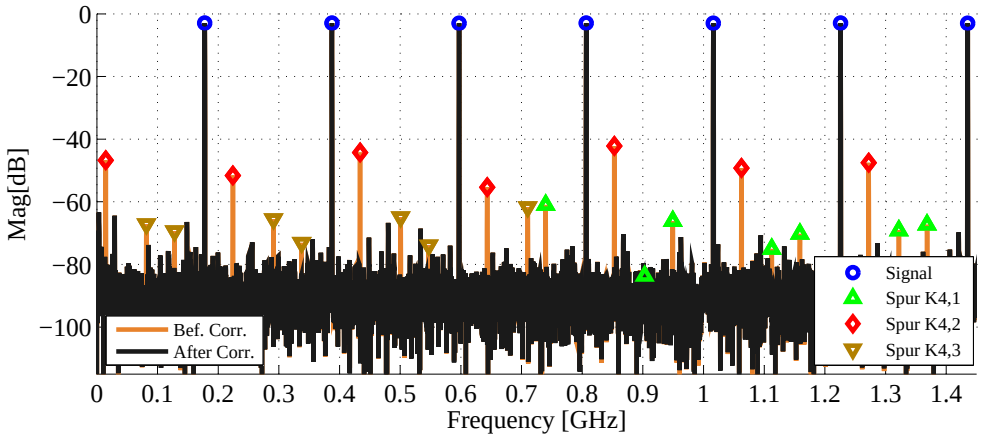

Figure 5.13: Measured ADC12D1800RF multi-tone spectrum at 20 °C in the 1st Nyquist zone (0 to 1.45 GHz) zone before and after correction using the proposed *Type 1* 4 TI-ADC FRM compensation architecture shown in Fig. 4.5.

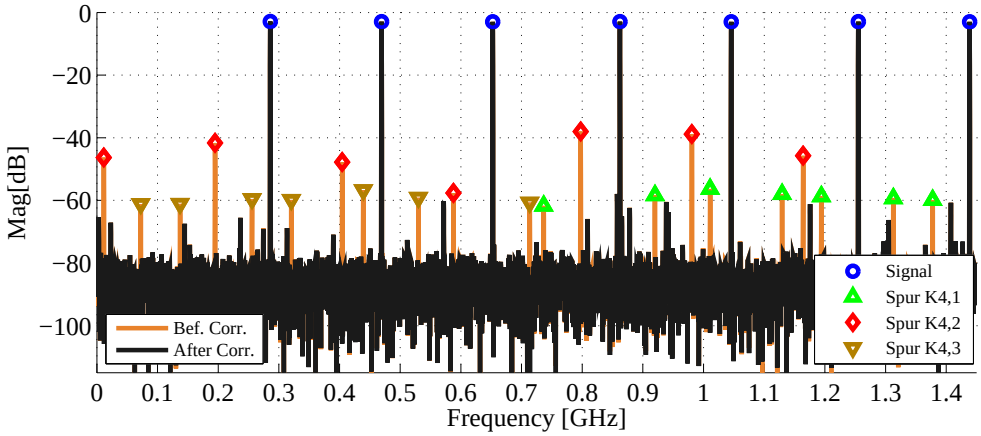

Figure 5.14: Measured ADC12D1800RF multi-tone spectrum at 20 °C in the second Nyquist (1.45 GHz to 2.9 GHz) zone before and after correction using the proposed *Type 1* 4 TI-ADC FRM compensation architecture shown in Fig. 4.5.

correction, as seen in Fig. 5.13 for the 1st Nyquist zone and in Fig. 5.14 for the 2nd Nyquist zone, verifying again the functionality of the proposed method.

The alternative *Type 2* version of the 4-channel TI-ADC FRM correction architecture depicted in Fig. 4.6, which has considerably reduced computational complexity compared to the *Type 1* correction architecture, is explored next. Using two multi-tone scenarios, as shown in Fig. 5.15 for the 1st Nyquist zone and in Fig. 5.16 for the 2nd Nyquist zone, the *Type 2* correction algorithm's validation is performed. Two sets of 20-tap correction

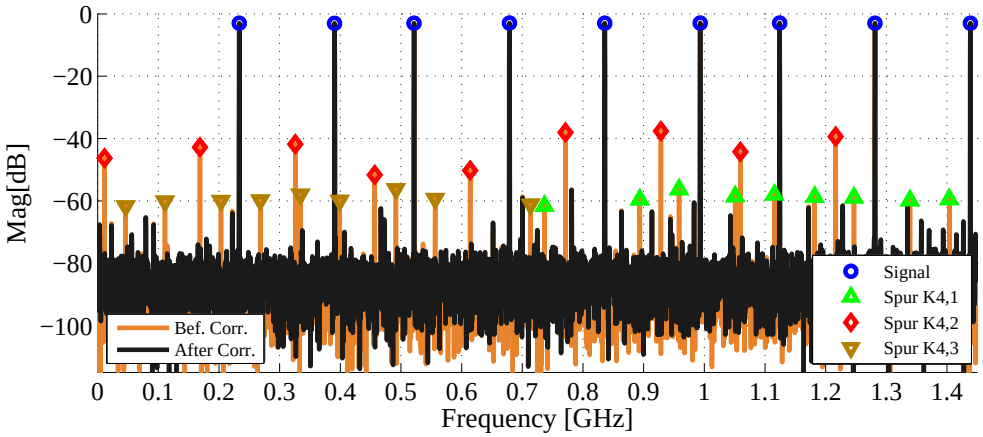

Figure 5.15: Measured ADC12D1800RF multi-tone spectrum at 20 °C in the 1st Nyquist zone (0 to 1.45 GHz) zone before and after correction using the proposed *Type 2* 4 TI-ADC FRM compensation architecture shown in Fig. 4.6.

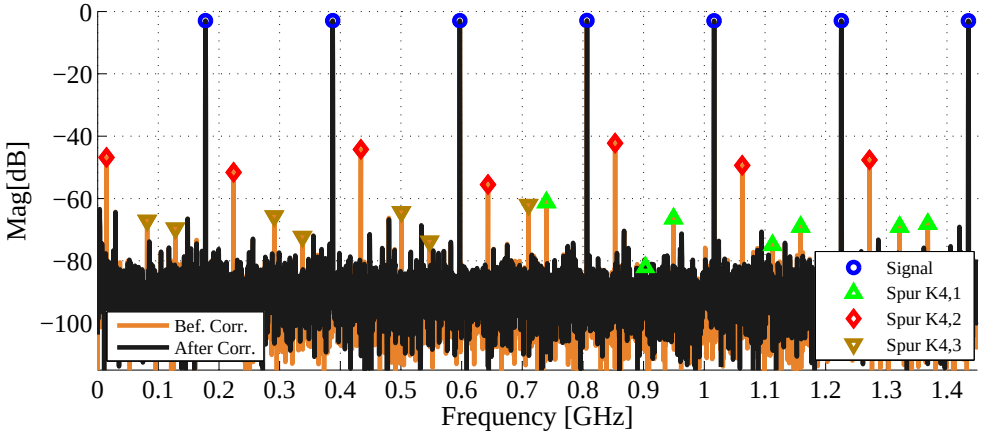

Figure 5.16: Measured ADC12D1800RF multi-tone spectrum at 20 °C in the second Nyquist (1.45 GHz to 2.9 GHz) zone before and after correction using the proposed *Type 2* 4 TI-ADC FRM compensation architecture shown in Fig. 4.6.

filters are calculated, as given in (4.38), one for the spur $k_{4,2}(t)$ and another for the joint reconstruction of $k_{4,1}(t)$ and $k_{4,3}(t)$. After being processed by the *Type 2* 4-channel TI-ADC FRM spurs correction architecture, the magnitude of the interleaving spurs $k_{4,1}(t)$, $k_{4,2}(t)$ and $k_{4,3}(t)$, are reduced to the noise floor level, as seen in Fig. 5.15 for the 1st Nyquist zone and in Fig. 5.16 for the 2nd Nyquist zone, verifying the functionality of the proposed method.

It is noted that the further reduction in computational complexity required to calculate the optimal filter via (4.38) can be reduced by utilizing (4.42). The block-wise solution in (4.38) requires computing $[\mathbf{\Gamma}_{i1} + \bar{\mathbf{\Gamma}}_{i1}]^{-1}$, which is circumvented by using the iteratively calculated optimal filter via (4.42).

5.3.3 Validation of Proposed Blind Identification and Correction of TI-ADC FRM Spurs using Modulated Communication Waveforms

Two measured examples with multiple wideband orthogonal frequency division multiplexing (OFDM) signals are provided in Fig. 5.17 and Fig. 5.18. The multiple wideband OFDM signals are located within the TI-ADC's second Nyquist zone between 1.45GHz to 2.9GHz. In the RF signal generation phase, the OFDM waveforms are filtered to further band limit the spectral content and suppress the inherent OFDM sidelobes. This is done for for better visualization of the TI-ADC's interleaving spurs' suppression after correction. The RF OFDM input signal is digitized by 4-channel TI-ADC, i.e., ADC12D1800RF. Blind identification of the FRM is performed using 32k samples of the 4-channel TI-ADC's output signal with the proposed *Type 2* 2-channel TI-ADC FRM compensation architecture using a 40-tap correction filter. Note that due to the large BW of the OFDM signal, the input power level of the OFDM signal needs to be reduced accordingly before being fed into the TI-ADC in order to avoid input signal clipping [2]. As the levels of the TI-ADC spurs $k_{4,1}(t)$ and $k_{4,3}(t)$ are considerably lower than spur $k_{4,2}(t)$, as seen in the measurement results in Fig. 5.5, Fig. 5.6 and Fig. 5.7, it suffices to perform only the correction of the spur $k_{4,2}(t)$ due to spurs $k_{4,1}(t)$ and $k_{4,3}(t)$ being already in the noise floor as in Fig. 5.17 and Fig. 5.18. It is shown in Fig. 5.17 and Fig. 5.18 that accurate spur suppression is achieved using the *Type 2* 2-channel TI-ADC FRM compensation architecture.

Next, a multiband quadrature phase shift keying (QPSK) signal scenario is created using multiple coexisting QPSK signals at different center frequencies. Multiple different QPSK signals at different center-frequencies, bandwidths and power levels are present in the simulation environment as depicted in Fig. 5.19. It is seen in Fig. 5.19 that the weaker signals are subject to interference from the FRM interleaving spurs of stronger signals. Non-linear distortion terms, i.e., 2nd and 3rd order distortion terms, have also been introduced into the spectrum and coexist alongside the 4-channel TI-ADC FRMs spurs. The proposed 4-channel TI-ADC FRM correction method shown in Fig. 4.5 is used. The circularity based algorithm, as given in (4.38), is utilized to calculate three 8 taps FRM spur correction filters using a signal block consisting of 262k samples. The obtained FRM interleaving spur correction filters are applied on a multitone CW test

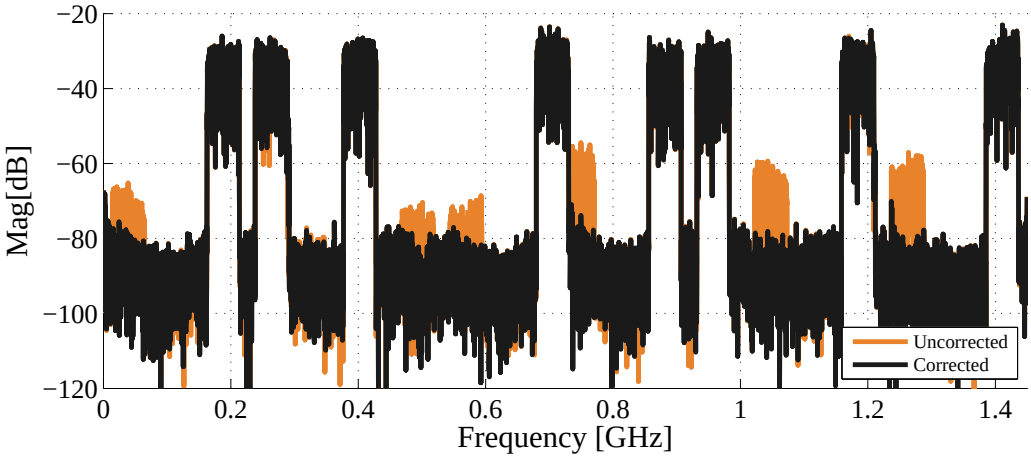

Figure 5.17: ADC12D1800RF spectra with non-contiguous OFDM input in the second Nyquist zone (1.45 GHz to 2.9 GHz), uncorrected and corrected using (4.38) and proposed2-channel TI-ADC *Type 2* FRM compensation architecture shown in Fig. 4.3 processing. Each OFDM waveform is $\sim$ 50 MHz wide.

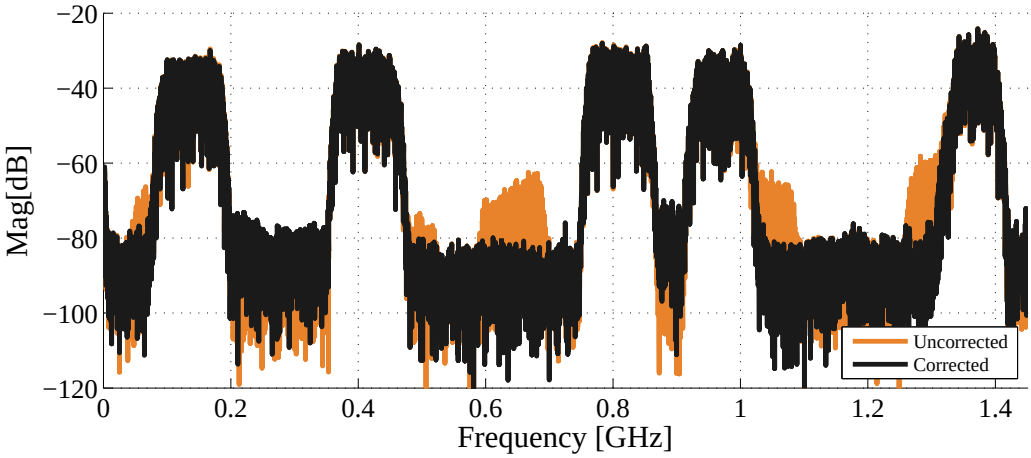

Figure 5.18: ADC12D1800RF spectra with non-contiguous OFDM input in the second Nyquist zone (1.45 GHz to 2.9 GHz), uncorrected and corrected using (4.38) and proposed 2-channel TI-ADC *Type 2* FRM compensation architecture shown in Fig. 4.3 processing. Each OFDM waveform is $\sim$ 80 MHz wide.

signal, which is subjected to the same 4 TI-ADC FRM mismatches. The non-linearity distortion spurs are not included in the multitone CW test signal scenario so that the interleaving FRM spur reduction achieved through the calculated filters can be better observed. It is seen in Fig. 5.20 that using the correction filters calculated from

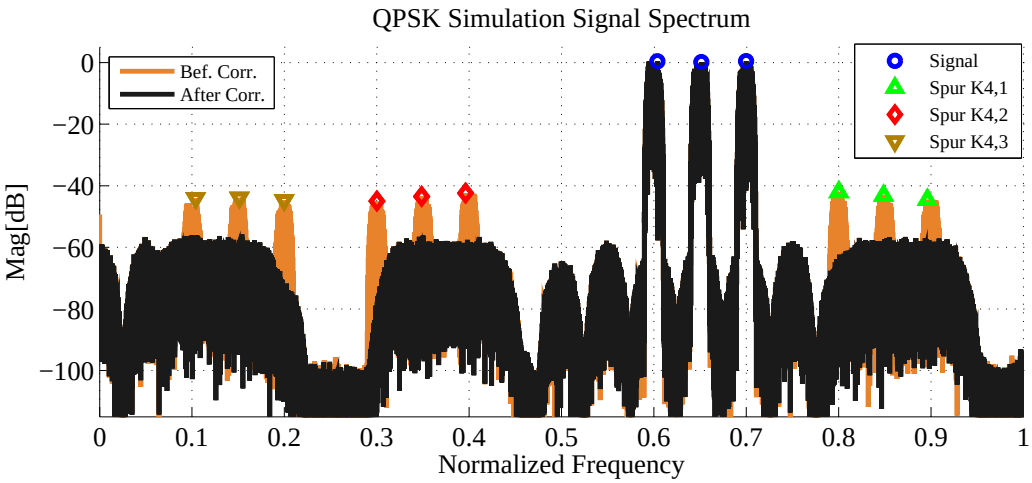

Figure 5.19: Simulated multi-QPSK signal spectrum subject to 4 TI-ADC mismatches before and after correction using (4.38) and proposed *Type 2* 4 TI-ADC FRM compensation architecture shown in Fig. 4.5.

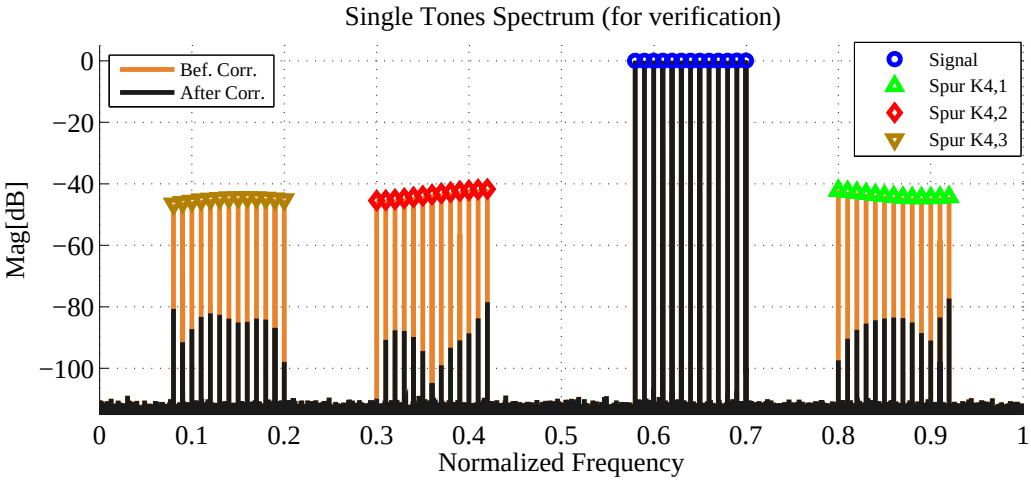

Figure 5.20: Simulated multi-tone test scenario to visualize and characterize the correction performance of the filters obtained with the signal in Fig. 5.19.

the multi-QPSK signal scenario adopting the correction architecture of Fig. 4.5 and (4.38) is able to reduce the interleaving FRM spurs close to the -80 dBc level. This demonstrates the functionality of the proposed identification method and validates the usage of circularity with actual modulated waveforms. It also shows that the circularity based algorithm can be used in the presence of the non-linear distortion components to accurately extract the FRM interleaving spurs.

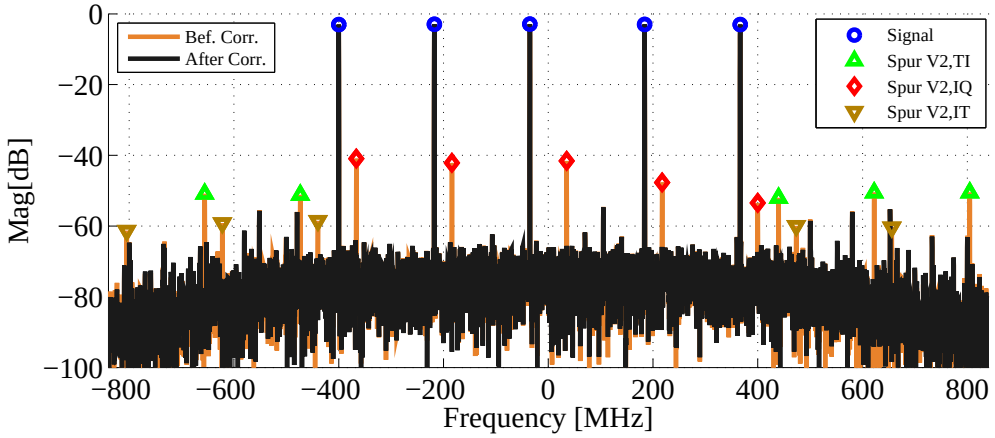

Figure 5.21: Measured 2-channel RF IQ-TIC Multi-tone spectrum before and after FRM spur correction.

The achieved results clearly demonstrate that the proposed blind schemes can provide high-performance FRM interleaving spur identification and correction even when evaluated using modulated waveforms used in communication systems and true-world TI-ADC board, which were tested with high frequency large bandwidth RF measurements and actual wideband waveforms.

5.4 Validation of Proposed Blind Identification and Correction of FRM Spurs in I/Q Downconversion 2 TI-ADC using Measured Data

A multi-tone scenario is constructed to create a challenging scenario to demonstrate and evaluate the proposed FRM spurs correction architecture depicted in Fig. 4.7, Fig. 4.8 and Fig. 4.9. Multiple CW tones are fed in between -400MHz to +400MHz relative to the RF center-frequency of 2.7 GHz. All three compensation filters in Fig. 4.7, Fig. 4.8 and Fig. 4.9 are calculated as given in eq. (4.38), with the individual filter lengths being 8 taps. It is clearly seen in Fig. 5.21 that all the spurs $v_{2,IQ}(t), v_{2,TI}(t)$ and $v_{2,IT}(t)$ are successfully reduced down to the noise floor, verifying again the functionality of the proposed methods.

CHAPTER 6

Conclusions

The key results and novel contributions of this thesis are shortly highlighted and summarized in this chapter. The potential of TI-ADCs in overcoming the individual ADC's technological limitations has fueled and still is catalyzing a lot of research effort in removing the performance limiting frequency response mismatches between the interleaved ADCs. After reviewing the key contributions made in this thesis work, some possible future work items are also reviewed and highlighted.

6.1 Summary of Thesis Contributions & Results

The first part of the contributions of this thesis is the comprehensive modeling of the TI-ADCs using complex valued signals, which provides new insight to the nature of the TI-ADC FRM spurs, i.e., how the FRM spurs are created, what type of FRM spurs are present and where they are located in the output spectrum. This also provides the fundamental starting point and background needed to utilize complex signal processing in solving the TI-ADC FRM mismatch spur identification and correction problems.

Using the complex-valued FRM spur modeling of the TI-ADCs, various new methods were then developed for the FRM spurs identification and correction in different types of TI-ADCs. The major contribution of this thesis includes establishing the fact that the TI-ADC mismatch parameters can be identified by utilizing the mirror frequency interference based techniques, which are classically encountered in I/Q downconversion. This finding led then to new types of architectures for the FRM spur identification and correction in TI-ADCs. It enabled constructing a first of its kind solution to solving the major open challenge in the field of time interleaved ADCs, i.e., the blind and adaptive identification of FRM in time interleaved ADCs. The first known examples of blind

adaptive FRM correction algorithms for 2-channel TI-ADC were developed which are able to fully detect the FRM within the band of use [P2],[P5],[P8]. The first known examples of blind adaptive FRM correction algorithms for 4-channel TI-ADC were then also developed which are able to estimate and correct the FRM within the band of use [P1],[P7],[P6].

In addition to this, novel analysis and insight were offered to increase the TI-ADC's analog BW. The study of the effects of FRM in wideband I/Q downconversion circuitry which utilizes TI-ADCs in its analog I and Q branches was carried out. In the analysis, the interactions between the frequency response mismatches in the various analog stages, i.e., in the analog I/Q downconversion and TI-ADCs circuitries, were established and the nature of the resulting spur components was characterized [P4]. This behavior was previously not systematically studied in the existing literature. It was then followed by the correction of these FRM mismatches, where the identification and compensation of the FRM spurs in the analog I/Q downconversion and the 2-channel TI-ADCs circuitry were all carried out. These are the first known published results which explicitly offer solutions to the suppression of FRM spurs in the 2-channel I/Q TI-ADC [P3].

Another interesting finding established in the thesis work was that the 2-channel I/Q TI-ADC's spectrum, with its corresponding mismatches components, share a lowpass-bandpass relationship with a 4-channel TI-ADC and its corresponding FRM spurs [P1].

6.2 Possible Future Work Topics

In the framework of this thesis, various contributions have been made to be able to deal with the FRM spurs in TI-ADCs and towards extending the analog BW of the TI-ADCs. However, there is still much work to be done in the field of TI-ADC impairments mitigation to achieve higher ADC system performance. Listed below are some examples of possible future work topics:

1. *Extending the FRM spur identification and correction techniques to general M-channel TI-ADCs.* The number of interleaved ADCs can amount, e.g., to 24, 32 or even 64 ADCs [14, 36, 78]. Therefore, the identification and correction architecture to suppress the FRM spurs should also be developed to mitigate these spurs in a TI-ADC with a higher number of interleaved ADCs.

2. *Studying the nature of FRM spurs in M-channel I/Q TI-ADCs and developing corresponding identification and correction solutions.* The study of the nature of the I/Q downconversion process in combination with 2-channel TI-ADC has been done in this thesis. In the next step, the analysis is to be extended regarding the

FRM spur components created in the output spectrum when a higher number of interleaved ADCs are used in combination with the I/Q downconversion process.

3. *Developing more advanced S.O.S. algorithms for MFI and/or FRM spurs identification.* The development of new and improved S.O.S. algorithms for the purposes of mirror frequency correlation measurement would definitely be beneficial as future enhancement for the existing MFI measuring algorithms such as those reported in [4, 5, 40, 51, 52, 83].

4. *The study of non-linear non-idealities in TI-ADCs.* Apart from linear FRM spurs correction, the TI-ADCs may also suffer from non-linear distortion spurs which are typically less severe than FRM mismatch spurs [3, 41, 80]. The study of non-linear distortion in TI-ADCs and its mitigation is also an interesting topic of future studies [68, 98].

References

[1] A. Ali, H. Dinc, P. Bhoraskar, C. Dillon, S. Puckett, B. Gray, C. Speir, J. Lanford, J. Brunsilius, P. Derounian, B. Jeffries, U. Mehta, M. McShea, and R. Stop, "A 14 Bit 1 GS/s RF Sampling Pipelined ADC With Background Calibration," *IEEE J. Solid-State Circuits*, vol. 49, no. 12, pp. 2857–2867, Dec 2014.

[2] M. Allén, "Nonlinear distortion in wideband radio receivers and analog-to-digital converters: Modeling and digital suppression," *Tampereen teknillinen yliopisto. Julkaisu-Tampere University of Technology. Publication; 1329*, 2015.

[3] Analog Devices. (2014) 12-Bit, 2.6 GSPS/2.5 GSPS/2.0 GSPS, 1.3 V/2.5 V Analog-to-Digital Converter. [Online]. Available: http://www.analog.com

[4] L. Anttila and M. Valkama, "Blind Signal Estimation in Widely-Linear Signal Models With Fourth-Order Circularity: Algorithms and Application to Receiver I/Q Calibration," *IEEE Signal Process. Lett.*, vol. 20, no. 3, pp. 221–224, March 2013.

[5] L. Anttila, M. Valkama, and M. Renfors, "Blind compensation of frequency-selective I/Q imbalances in quadrature radio receivers: Circularity -based approach," in *IEEE International Conference on Acoustics, Speech and Signal Processing, 2007. ICASSP 2007*, vol. 3, 2007, pp. III–245–III–248.

[6] L. Anttila, M. Valkama, and M. Renfors, "Circularity-based I/Q imbalance compensation in wideband direct-conversion receivers," *IEEE Trans. Veh. Technol.*, vol. 57, no. 4, pp. 2099–2113, 2008.

[7] L. Anttila, "Digital front-end signal processing with widely-linear signal models in radio devices," *Tampereen teknillinen yliopisto. Julkaisu-Tampere University of Technology. Publication; 985*, 2011.

[8] W. C. Black Jr. and D. Hodges, "Time interleaved converter arrays," *IEEE J. Solid-State Circuits*, vol. 15, no. 6, pp. 1022–1029, 1980.

[9] A. Bonnetat, J.-M. Hode, G. Ferre, and D. Dallet, "An Adaptive All-Digital Blind Compensation of Dual-TIADC Frequency-Response Mismatch Based on Complex Signal Correlations," *IEEE Trans. Circuits Syst. II, Exp. Briefs*, vol. 62, no. 9, pp. 821–825, Sept 2015.

[10] A. Bonnetat, J.-M. Hode, G. Ferre, and D. Dallet, "Correlation-Based Frequency-Response Mismatch Compensation of Quad-TIADC Using Real Samples," *IEEE Trans. Circuits Syst. II, Exp. Briefs*, vol. 62, no. 8, pp. 746–750, Aug 2015.

[11] M. Brandolini, Y. Shin, K. Raviprakash, T. Wang, R. Wu, H. Geddada, Y.-J. Ko, Y. Ding, C.-S. Huang, W.-T. Shih, M.-H. Hsieh, W.-T. Chou, T. Li, A. Shrivastava, Y.-C. Chen, B.-J. Hung, G. Cusmai, J. Wu, M. Zhang, Y. Yao, G. Unruh, A. Venes, H. Huang, and C.-Y. Chen, "A 5 GS/s 150 mW 10 b SHA-Less Pipelined/SAR Hybrid ADC for Direct-Sampling Systems in 28 nm CMOS," *IEEE J. Solid-State Circuits*, vol. PP, no. 99, pp. 1–13, 2015.

[12] K. Doris, E. Janssen, C. Nani, A. Zanikopoulos, and G. Van Der Weide, "A 480mW 2.6GS/s 10b 65nm CMOS time-interleaved ADC with 48.5dB SNDR up to nyquist," in *IEEE ISSCC*, Feb. 2011, pp. 180–182.

[13] K. Doris, A. Molnar, X. Jiang, and S. T. Ryu, "F2: data-converter calibration and dynamic-matching techniques," in *IEEE ISSCC*, Jan 2016, pp. 495–497.

[14] Y. Duan and E. Alon, "A 12.8 GS/s Time-Interleaved ADC With 25 GHz Effective Resolution Bandwidth and 4.6 ENOB," *IEEE J. Solid-State Circuits*, vol. 49, no. 8, pp. 1725–1738, Aug 2014.

[15] M. El-Chammas and B. Murmann, "General analysis on the impact of phase-skew in time-interleaved ADCs," *IEEE Trans. Circuits Syst. I, Reg. Papers*, vol. 56, no. 5, pp. 902–910, 2009.

[16] M. El-Chammas and B. Murmann, "A 12-GS/s 81-mW 5-bit time-interleaved flash ADC with background timing skew calibration," *IEEE Journal of Solid-State Circuits*, vol. 46, no. 4, pp. 838–847, 2011.

[17] J. Elbornsson, F. Gustafsson, and J.-E. Eklund, "Blind adaptive equalization of mismatch errors in a time-interleaved A/D converter system," *IEEE Trans. Circuits Syst. I, Reg. Papers*, vol. 51, no. 1, pp. 151–158, Jan 2004.

[18] J. Elbornsson, F. Gustafsson, and J.-E. Eklund, "Analysis of mismatch effects in a randomly interleaved A/D converter system," *IEEE Trans. Circuits Syst. I, Reg. Papers*, vol. 52, no. 3, pp. 465–476, March 2005.

[19] J. Elbornsson, F. Gustafsson, and J.-E. Eklund, "Blind equalization of time errors in a time-interleaved ADC system," *IEEE Trans. Signal Process.*, vol. 53, no. 4, pp. 1413–1424, April 2005.

[20] F. Harris, X. Chen, and E. Venosa, "A novel PR channelizer-based architecture for estimation and correction of timing and gain mismatches in two channel TI-ADCs," in *IEEE 55th MWSCAS*, 2012, pp. 1140–1143.

[21] F. Harris, X. Chen, E. Venosa, and F. Palmieri, "Two channel TI-ADC for communication signals," in *IEEE 12th International Workshop SPAWC*, 2011, pp. 576–580.

[22] V. Hiremath, "Design of Ultra High Speed Flash ADC, Low Power Folding and Interpolating ADC in CMOS 90nm Technology," Ph.D. dissertation, Wright State University, 2010.

[23] S. Huang and B. Levy, "Blind calibration of timing offsets for four-channel time-interleaved ADCs," *IEEE Transactions on Circuits and Systems I: Regular Papers*, vol. 54, no. 4, pp. 863–876, 2007.

[24] V. Ingle and J. Proakis, *Digital signal processing using MATLAB*. Cengage Learning, 2011.

[25] S. Jamal, D. Fu, N. Chang, P. Hurst, and S. Lewis, "A 10-b 120-msample/s time-interleaved analog-to-digital converter with digital background calibration," *IEEE Journal of Solid-State Circuits*, vol. 37, no. 12, pp. 1618–1627, 2002.

[26] S. Jamal, D. Fu, M. Singh, P. Hurst, and S. Lewis, "Calibration of sample-time error in a two-channel time-interleaved analog-to-digital converter," *IEEE Transactions on Circuits and Systems I: Regular Papers*, vol. 51, no. 1, pp. 130–139, 2004.

[27] E. Janssen, K. Doris, A. Zanikopoulos, A. Murroni, G. van der Weide, Y. Lin, L. Alvado, F. Darthenay, and Y. Fregeais, "An 11b 3.6GS/s time-interleaved SAR ADC in 65nm CMOS," in *IEEE ISSCC*, Feb. 2013, pp. 464–465.

[28] X. Jiang, *Digitally-Assisted Analog and Analog-Assisted Digital IC Design*. Cambridge University Press, 2015.

[29] H. Johansson, "A polynomial-based time-varying filter structure for the compensation of frequency-response mismatch errors in time-interleaved ADCs," *IEEE J. Sel. Topics. Signal Process*, vol. 3, no. 3, pp. 384–396, 2009.

[30] H. Johansson, "Relations between zero-if receiver I/Q and TI-ADC channel mismatches," *IEEE Trans. Signal Process.*, vol. 62, no. 13, pp. 3403–3414, July 2014.

[31] H. Johansson and P. Lowenborg, "A least-squares filter design technique for the compensation of frequency response mismatch errors in time-interleaved A/D converters," *IEEE Trans. Circuits Syst. II, Exp. Briefs*, vol. 55, no. 11, pp. 1154–1158, 2008.

[32] H. Johansson, P. Lowenborg, and K. Vengattaramane, "Least-squares and minimax design of polynomial impulse response FIR filters for reconstruction of two-periodic nonuniformly sampled signals," *IEEE Trans. Circuits Syst. I, Reg. Papers*, vol. 54, no. 4, pp. 877–888, 2007.

[33] R. Kapusta, "Sar adcs in parallel [time-interleaved] converter arrays," in *Custom Integrated Circuits Conference (CICC), 2015 IEEE*. IEEE, 2015, pp. 1–86.

[34] W. Kester, "ADC Architectures VI: Folding ADCs," *Analog Devices Inc., Rev. A*, vol. 10, no. 08.

[35] R. Khalil, M.-M. Louerat, R. Petigny, and H. Gicquel, "Background time skew calibration for time-interleaved adc using phase detection method," in *IEEE NEWCAS*, June 2012, pp. 257–260.

[36] L. Kull, T. Toifl, M. Schmatz, P. Francese, C. Menolfi, M. Braendli, M. Kossel, T. Morf, T. Andersen, and Y. Leblebici, "22.1 a 90gs/s 8b 667mw 64 x interleaved SAR ADC in 32nm digital SOI CMOS," in *IEEE ISSCC*, Feb 2014, pp. 378–379.

[37] N. Kurosawa, H. Kobayashi, K. Maruyama, H. Sugawara, and K. Kobayashi, "Explicit analysis of channel mismatch effects in time-interleaved ADC systems," *IEEE Trans. Circuits Syst. I, Fundam. Theory Appl.*, vol. 48, no. 3, pp. 261–271, 2001.

[38] C. H. Law, P. Hurst, and S. Lewis, "A four-channel time-interleaved ADC with digital calibration of interchannel timing and memory errors," *IEEE Journal of Solid-State Circuits*, vol. 45, no. 10, pp. 2091–2103, 2010.

[39] Y. C. Lim, Y.-X. Zou, J. W. Lee, and S.-C. Chan, "Time-interleaved analog-to-digital-converter compensation using multichannel filters," *IEEE Trans. Circuits Syst. I, Reg. Papers*, vol. 56, no. 10, pp. 2234–2247, 2009.

[40] H. Lin and K. Yamashita, "Time domain blind I/Q imbalance compensation based on real-valued filter," *IEEE Trans. Wireless Commun.*, vol. 11, no. 12, pp. 4342–4350, 2012.

[41] Linear Technology. (2014) Linear Technology 16-Bit, 130 Msps ADC. [Online]. Available: http://www.linear.com/product/LTC2208

[42] S. J. Liu, P. P. Qi, J. S. Wang, M. H. Zhang, and W. S. Jiang, "Adaptive calibration of channel mismatches in time-interleaved ADCs based on equivalent signal recombination," *IEEE Instrum. Meas. Mag.*, vol. 63, no. 2, pp. 277–286, Feb. 2014.

[43] M. El-Chammas et al., "A 12 bit 1.6 GS/s BiCMOS 2x2 hierarchical time-interleaved pipeline ADC," *IEEE J. Solid-State Circuits*, vol. Early Access Online, 2014.

[44] D. Marelli, K. Mahata, and M. Fu, "Linear LMS compensation for timing mismatch in time-interleaved ADCs," *IEEE Trans. Circuits Syst. I, Reg. Papers*, vol. 56, no. 11, pp. 2476–2486, 2009.

[45] J. Marttila, "Quadrature sigma-delta modulators for reconfigurable a/d interface and dynamic spectrum access: Analysis, design principles and digital post-processing," *Tampereen teknillinen yliopisto. Julkaisu-Tampere University of Technology. Publication; 1265*, 2014.

[46] J. Matsuno, T. Yamaji, M. Furuta, and T. Itakura, "All-digital background calibration technique for time-interleaved ADC using pseudo aliasing signal," *IEEE Transactions on Circuits and Systems I: Regular Papers*, vol. 60, no. 5, pp. 1113–1121, 2013.

[47] J. Matsuno, T. Yamaji, M. Furuta, and T. Itakura, "All-digital background calibration for time-interleaved ADC using pseudo aliasing signal," in *2012 IEEE International Symposium on Circuits and Systems (ISCAS)*, 2012, pp. 1050–1053.

[48] B. Murmann, "Digitally assisted data converter design," in *ESSCIRC, Proceedings of the*, Sep. 2013, pp. 24–31.

[49] B. Murmann. (2015) ADC Performance Survey 1997-2015. [Online]. Available: http://www.stanford.edu/~murmann/adcsurvey.html

[50] D. Nairn, "Time-interleaved analog-to-digital converters," in *IEEE Custom Integrated Circuits Conference, 2008. CICC 2008*, 2008, pp. 289–296.

[51] W. Nam, H. Roh, J. Lee, and I. Kang, "Blind adaptive I/Q imbalance compensation algorithms for direct-conversion receivers," *IEEE Signal Process. Lett.*, vol. 19, no. 8, pp. 475–478, 2012.

[52] B. Narasmihan, C. Chien, S.-H. Yan, P. Liang, and H. Hwang, "Robust low-complexity blind frequency-dependent I/Q estimation and compensation," in *IEEE GLOBECOM 2013*. IEEE, pp. 4331–4336.

[53] T. Nieminen *et al.*, "High-performance analog-to-digital converters and line drivers," 2016.

[54] A. V. Oppenheim, R. W. Schafer, J. R. Buck *et al.*, *Discrete-time signal processing*. Prentice-hall Englewood Cliffs, 1989, vol. 2.

[55] A. Petraglia and S. Mitra, "High speed A/D conversion using QMF banks," in *IEEE International Symposium on Circuits and Systems ISCAS*, 1990, pp. 2797–2800.

[56] A. K. M. Pillai and H. Johansson, "Prefilter-based reconfigurable reconstructor for time-interleaved adcs with missing samples," *IEEE Trans. Circuits Syst. II, Exp. Briefs*, vol. 62, no. 4, pp. 392–396, April 2015.

[57] G. Proakis John and G. Manolakis Dimitris, "Digital signal processing, principles, algorithms, and applications," *Pentice Hall*, 1996.

[58] P. Pupalaikis, "An 18 ghz bandwidth, 60 GS/s sample rate real-time waveform digitizing system," in *Microwave Symposium, 2007 IEEE/MTT-S International*, 2007, pp. 195–198.

[59] L. Qiu, K. Tang, Y. Zheng, and L. Siek, "A digital time skew calibration technique for time-interleaved adcs," in *IEEE ISCAS*, May 2015, pp. 2297–2300.

[60] B. Razavi, "Problem of timing mismatch in interleaved ADCs," in *2012 IEEE Custom Integrated Circuits Conference (CICC)*, 2012, pp. 1–8.

[61] B. Razavi, "Design considerations for interleaved ADCs," *IEEE Journal of Solid-State Circuits*, vol. 48, no. 8, pp. 1806–1817, 2013.

[62] S. Saleem, "Adaptive blind calibration of gain and timing mismatches in a time-interleaved adc - a performance analysis," in *IEEE I2MTC*, May 2012, pp. 2672–2677.

[63] S. Saleem and C. Vogel, "Adaptive compensation of frequency response mismatches in high-resolution time-interleaved ADCs using a low-resolution ADC and a time-varying filter," in *Proceedings of 2010 IEEE International Symposium on Circuits and Systems (ISCAS)*, 2010, pp. 561–564.

[64] S. Saleem and C. Vogel, "Adaptive blind background calibration of polynomial-represented frequency response mismatches in a two-channel time-interleaved ADC," *IEEE Transactions on Circuits and Systems I: Regular Papers*, vol. 58, no. 6, pp. 1300–1310, 2011.

[65] S. Saleem, "Adaptive calibration of frequency response mismatches in time-interleaved analog-to-digital converters," Ph.D. dissertation, Graz University of Technology, Austria, 2010.

[66] P. Satarzadeh, B. Levy, and P. Hurst, "Bandwidth mismatch correction for a two-channel time-interleaved A/D converter," in *IEEEISCAS*, 2007, pp. 1705–1708.

[67] P. Satarzadeh, B. Levy, and P. Hurst, "Adaptive semiblind calibration of bandwidth mismatch for two-channel time-interleaved ADCs," *IEEE Trans. Circuits Syst. I, Reg. Papers*, vol. 56, no. 9, pp. 2075–2088, 2009.

[68] P. Satarzadeh, B. Levy, and P. Hurst, "Digital calibration of a nonlinear S/H," *IEEE Journal of Selected Topics in Signal Processing*, vol. 3, no. 3, pp. 454–471, 2009.

[69] P. Satarzadeh, B. Levy, and P. Hurst, "A parametric polyphase domain approach to blind calibration of timing mismatches for m-channel time-interleaved ADCs," in *Proceedings of 2010 IEEE International Symposium on Circuits and Systems (ISCAS)*, 2010, pp. 4053–4056.

[70] M. Seo and M. Rodwell, "Generalized blind mismatch correction for a two-channel time-interleaved ADC: analytic approach," in *IEEE ISCAS 2007*, pp. 109–112.

[71] M. Seo, M. Rodwell, and U. Madhow, "Generalized blind mismatch correction for two-channel time-interleaved a-to-d converters," in *IEEE International Conference on Acoustics, Speech and Signal Processing, 2007. ICASSP 2007*, vol. 3, 2007, pp. III–1505–III–1508.

[72] M. Seo, M. J. W. Rodwell, and U. Madhow, "Comprehensive digital correction of mismatch errors for a 400-msamples/s 80-dB SFDR time-interleaved analog-to-digital converter," *IEEE Trans. Microw. Theory Tech.*, vol. 53, no. 3, pp. 1072–1082, 2005.

[73] M. Seo, M. J. W. Rodwell, and U. Madhow, "Blind correction of gain and timing mismatches for a two-channel time-interleaved analog-to-digital converter: experimental verification," in *2006 IEEE International Symposium on Circuits and Systems, 2006. ISCAS 2006. Proceedings*, 2006, pp. 4 pp.–3397.

[74] M. Seo, M. J. W. Rodwell, and U. Madhow, "A low computation adaptive blind mismatch correction for time-interleaved ADCs," in *49th IEEE International Midwest Symposium on Circuits and Systems, 2006. MWSCAS '06*, vol. 1, 2006, pp. 292–296.

[75] B. Setterberg, K. Poulton, S. Ray, D. Huber, V. Abramzon, G. Steinbach, J. Keane, B. Wuppermann, M. Clayson, M. Martin, R. Pasha, E. Peeters, A. Jacobs, F. Demarsin, A. Al-Adnani, and P. Brandt, "A 14b 2.5GS/s 8-way-interleaved pipelined ADC with background calibration and digital dynamic linearity correction," in *IEEE ISSCC*, Feb. 2013, pp. 466–467.

[76] S. Singh, M. Epp, M. Valkama, G. Vallant, and W. Schlecker, "A novel blind adaptive correction algorithm for 2-channel time-interleaved ADCs," in *19th IMEKO TC 4 Symposium and 17th IWADC Workshop.*, 2013, pp. 188–193.

[77] SP Devices. (2016) ADX - ADC Interleaving IP. [Online]. Available: http://spdevices.com/index.php/products2

[78] D. Stepanovic and B. Nikolic, "A 2.8 GS/s 44.6 mW time-interleaved ADC achieving 50.9 dB SNDR and 3 dB effective resolution bandwidth of 1.5 GHz in 65 nm CMOS," *IEEE Journal of Solid-State Circuits*, vol. 48, no. 4, pp. 971–982, 2013.

[79] D. V. Stepanovic, "Calibration techniques for time-interleaved SAR A/D converters," Ph.D. dissertation, University of California, Berkeley, 2012.

[80] Texas Instrument. (2013) ADC12D1800RF 12-Bit, Single 3.6 GSPS RF Sampling ADC (Rev. H). [Online]. Available: http://www.ti.com

[81] Texas Instrument. (2013) TC1-DESIQ-SBB User Guide. [Online]. Available: http://www.ti.com

[82] Texas Instrument. (2014) ADC12J4000 12-Bit 4 GSPS ADC With Integrated DDC (Rev. C). [Online]. Available: http://www.ti.com

[83] Y. Tsai, C.-P. Yen, and X. Wang, "Blind frequency-dependent I/Q imbalance compensation for direct-conversion receivers," *IEEE Trans. Wireless Commun.*, vol. 9, no. 6, pp. 1976–1986, 2010.

[84] K. Tsui and S. Chan, "A Novel Iterative Structure for Online Calibration of M-channel Time-Interleaved ADCs," *IEEE Transactions on Instrumentation and Measurement*, vol. 63, no. 2, pp. 312–325, Feb. 2014.

[85] S. L. Tuai, B. Nikolic, T. Iizuka, and I. Fujimori, "F1: High-speed interleaved ADCs," in *IEEE ISSCC*, Feb 2015, pp. 1–2.

[86] G. Vallant, M. Allen, S. Singh, M. Epp, S. Chartier, and M. Valkama, "Direct downconversion architecture performance in compact pulse-doppler phased array radar receivers," in *2013 IEEE 13th Topical Meeting on Silicon Monolithic Integrated Circuits in RF Systems (SiRF)*, 2013, pp. 102–104.

[87] G. Vallant, M. Epp, W. Schlecker, U. Schneider, L. Anttila, and M. Valkama, "Analog IQ impairments in zero-IF radar receivers: Analysis, measurements and digital compensation," in *Instrumentation and Measurement Technology Conference (I2MTC), 2012 IEEE International*, 2012, pp. 1703–1707.

[88] G. Vallant, M. Epp, M. Allén, M. Valkama, and F. K. Jondral, "System-Level Mitigation of Undersampling ADC Nonlinearity for High-IF Radio Receivers," *Frequenz*, vol. 66, no. 9-10, pp. 311–319, 2012.

[89] G. J. Vallant, "Modellbasierte entzerrung von analog/digital-wandler-systemen," Ph.D. dissertation, Inst. für Nachrichtentechnik, 2013.

[90] J.-A. Vernhes, M. Chabert, B. Lacaze, G. Lesthievent, R. Baudin, and M.-L. Boucheret, "Adaptive estimation and compensation of the time delay in a periodic non-uniform sampling scheme," in *International Conference on SampTA*, May 2015, pp. 473–477.

[91] F. Vessal and C. A. T. Salama, "An 8-bit 2-gsample/s folding-interpolating analog-to-digital converter in SiGe technology," *Solid-State Circuits, IEEE Journal of*, vol. 39, no. 1, pp. 238–241, 2004.

[92] C. Vogel, "The impact of combined channel mismatch effects in time-interleaved ADCs," *IEEE Instrum. Meas. Mag.*, vol. 54, no. 1, pp. 415–427, 2005.

[93] C. Vogel, M. Hotz, S. Saleem, K. Hausmair, and M. Soudan, "A review on low-complexity structures and algorithms for the correction of mismatch errors in time-interleaved ADCs," in *New Circuits and Systems Conference (NEWCAS), 2012 IEEE 10th International*, 2012, pp. 349–352.

[94] C. Vogel and H. Johansson, "Time-interleaved analog-to-digital converters: status and future directions," in *IEEE ISCAS*, 2006, pp. 3386 –3389.

[95] C. Vogel and S. Mendel, "A flexible and scalable structure to compensate frequency response mismatches in time-interleaved ADCs," *IEEE Trans. Circuits Syst. I, Reg. Papers*, vol. 56, no. 11, pp. 2463–2475, 2009.

[96] C. Vogel, S. Saleem, and S. Mendel, "Adaptive blind compensation of gain and timing mismatches in M-channel time-interleaved ADCs," in *15th IEEE ICECS*, 2008, pp. 49–52.

[97] C. Vogel, "Modeling, identification, and compensation of channel mismatch errors in time-interleaved analog-to-digital converters," Ph.D. dissertation, Citeseer, 2005.

[98] Y. Wang, H. Johansson, H. Xu, and Z. Sun, "Joint Blind Calibration for Mixed Mismatches in Two-Channel Time-Interleaved ADCs," *IEEE Trans. Circuits Syst. I, Reg. Papers*, vol. 62, no. 6, pp. 1508–1517, June 2015.

[99] M. White and Y. Chen, "Scaled cmos technology reliability users guide," 2008.

[100] R. Yi, M. Wu, K. Asami, H. Kobayashi, R. Khatami, A. Katayama, I. Shimizu, and K. Katoh, "Digital Compensation for Timing Mismatches in Interleaved ADCs," in *22nd ATS*, Nov 2013, pp. 134–139.

[101] Y. X. Zou and X. J. Xu, "Blind Timing Skew Estimation Using Source Spectrum Sparsity in Time-Interleaved ADCs," *IEEE Trans. Instrum. Meas.*, vol. 61, no. 9, pp. 2401–2412, Sept 2012.

[102] Y. Zou, B. Li, and X. Chen, "An efficient blind timing skews estimation for time-interleaved analog-to-digital converters," in *2011 17th International Conference on Digital Signal Processing (DSP)*, 2011, pp. 1–4.

Tampereen teknillinen yliopisto
PL 527
33101 Tampere

Tampere University of Technology
P.O.B. 527
FI-33101 Tampere, Finland

ISBN 978-952-15-3773-8
ISSN 1459-2045